ISSN: 3102-0372 (Online)

Dec. 2024

Vol. 1, No. 1 and 2

Official Journal of

Nepal Society of Engineering Geology (NSEG)

Asian Journal of Engineering Geology

Vol. 1 No. 1 and 2, December 2024

Official Journal of Nepal Society of Engineering Geology

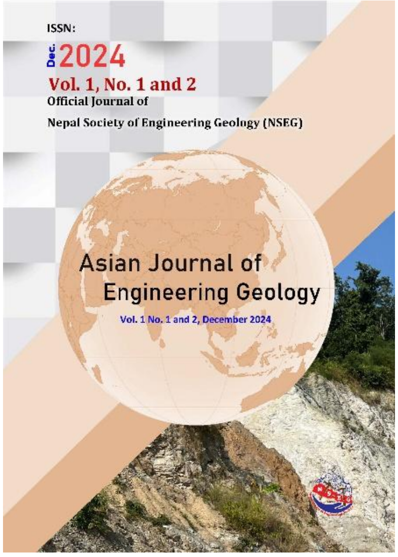

Asian Journal of Engineering Geology (AJEG)

Concept

The Asian Journal of Engineering Geology (**AJEG**), published by the Nepal Society of Engineering Geology (**NSEG**), is envisioned as a dedicated platform for advancing the understanding and application of engineering geology within the unique geological context of Asia, with a particular focus on the Himalayan region, while also welcoming contributions relevant to other parts of the world.

In recent years, research in engineering geology and related fields has seen significant progress. However, specialized publication platforms remain limited, especially in Asia, hindering the effective dissemination of research findings and knowledge sharing among engineering geologists. To address this gap, NSEG has launched the Asian Journal of Engineering Geology (AJEG), offering a professional and accessible forum for geoscientists, engineers, and environmentalists engaged in landslide studies, environmental geoscience, and engineering geological research.

AJEG aims to be a key resource for stakeholders seeking updated information on the geological challenges and engineering solutions relevant to seismically active and geologically complex regions like the Himalayas and beyond. The journal is committed to publishing original research, case studies, and technical notes that contribute to a deeper understanding of engineering geology in diverse terrains. Under the auspices of **NSEG**, **AJEG** places particular emphasis on:

- Slope stability and landslide hazard assessment
- Earthquake geology and seismic risk analysis
- Engineering geological aspects of infrastructure development
- Environmental and geotechnical investigations
- Integration of geological, geotechnical, and environmental knowledge for sustainable development

The journal actively promotes collaboration among researchers, engineers, and geologists from Asia and around the globe. By engaging regional experts and fostering interdisciplinary dialogue, **AJEG** seeks to address current and emerging challenges in engineering geology through shared knowledge and innovation.

In addition to peer-reviewed articles, **AJEG** will feature updates on conferences, research initiatives, and activities organized by the Nepal Society of Engineering Geology. This will position the journal not only as a scholarly publication but also as a hub for professional exchange and community building within the field of engineering geology in Nepal and across the region.

Aims and Scope

The Asian Journal of Engineering Geology (**AJEG**) serves as a common platform for the publication of integrated research covering all aspects of engineering geology. The journal welcomes original research articles, rapid reports on emerging engineering geology issues, case studies, and technical notes highlighting practical applications. Researchers and practitioners are encouraged to submit original, unpublished contributions. Subject areas include, but are not limited to, the following fields:

- Applied geomorphology
- Structural geology
- Applied geophysics and g
- Geochemistry
- Environmental geology
- Hydrogeology
- Land use planning
- Natural hazards
- Remote sensing techniques
- Soil and rock mechanics
- Applied geotechnical engineering
- Urban Engineering Geology
- Engineering Geology of marine and reservoir.
- Engineering geology in flash floods and tsunami
- Landslide hazard assessment and mapping
- GIS applications in engineering geology
- Landslide monitoring and landslide mitigation
- Engineering geology of the Himalayan slopes
- Rainfall-induced landslides
- Earthquake-induced landslides
- Anthropogenic controls on hazards
- Stability of dams and embankments
- Engineering geology of heritage areas, monitoring and mitigation
- Groundwater monitoring
- Seismic Hazard and Risk
- Disaster Risk Reduction and Management
- Engineering geology of Tunnels and bridges
- Foundations on slopes and plains

- Early warning of multi-hazard risk
- Landslide hazard management at community level
- Physical and numerical modeling in engineering geology
- High altitude engineering geological issues.
- Economics of natural hazards and related climate change
- Agricultural geology
- Snow avalanche
- Engineering geology and infrastructure development
- Snow cover in the Himalaya
- Environment friendly low cost infrastructure development
- Rural infrastructures and engineering geology
- Geotechnical engineering, modeling and ground improvement
- Nature-based solutions for disaster risk reduction

These topics suggest a multidisciplinary approach, encompassing various aspects of geology and engineering that have practical applications in fields such as environmental management, land planning, and geotechnical engineering.

Publication program

The Asian Journal of Engineering Geology (**AJEG**) publishes two issues each year. It is a peer-reviewed journal committed to disseminating the latest developments across various fields of engineering geology. **AJEG** is an open-access online journal, freely available to readers worldwide.

The Nepal Society of Engineering Geology promotes open access publishing to broaden the journal's global reach, enhance the visibility and impact of published research, and improve indexing across major search engines. Researchers and professionals from all relevant disciplines are invited to submit high-quality manuscripts presenting cutting-edge research or innovations in engineering geology and related areas. **AJEG** welcomes both individual and institutional submissions aligned with the journal's aims and scope.

Editorial Team

Editor-in-Chief

Associate Editor-in-Chief

Associate Editor-in-Chief

Editorial Board Members

We invite researchers specializing in engineering geology to become part of the editorial board and contribute to our publication. If you are interested in joining, kindly send an email to nsegnepal@gmail.com.

Instructions to Contributors

All types of manuscripts, including original articles, rapid reports on recent engineering geology issues, case studies, and technical notes, submitted for publication will undergo peer review by at least two experts in the relevant field. The review process is double-blind, meaning the authors will not know the identity of the reviewers. In some cases, editors may also serve as reviewers.

Authors' Responsibilities

Only individuals who have made significant intellectual contributions to the content of the manuscript should be listed as authors. Authorship should be based on contributions to the conception and design of the study, active involvement in drafting or critically revising the manuscript, and participation in the final revision process.

The corresponding author is responsible for submitting the final version of the manuscript following the peer review process. Any external support, such as funding, equipment, or institutional assistance, must be clearly acknowledged in the Acknowledgment section.

In the Comments to the Editor section during submission, authors must disclose any prior or duplicate publication of the manuscript's content. All submissions to AJEG are subject to plagiarism screening, and the acceptable similarity index is limited to a maximum of 20%. Author should use given Template in the web site for preparation of manuscript.

Manuscript Preparation Overview

All submissions to the Asian Journal of Engineering Geology (AJEG) must be written in International English. Authors whose first language is not English are strongly encouraged to have their manuscripts reviewed by a native English speaker or to use a professional English editing service prior to submission. All references, including online sources, must be formatted according to the journal's referencing guidelines outlined in this document. Each submitted article must include an abstract that briefly summarizes the key content and findings of the study. The name, institutional address, and email address of the corresponding author must be clearly indicated on the title page.

Figures and tables should be embedded within the manuscript after the list of references. Original figures should be at least half the size of A4 paper in their longest dimension. Acceptable formats for figures and images are TIFF (TIF) with a resolution of 300–600 pixels per inch (ppi). Monochrome images should be saved in grayscale mode, while color images must be in RGB mode. Only single-layer images are accepted. Authors should make every effort to avoid jargon, clearly define all nonstandard abbreviations upon first use, and present the content in a clear, concise, and accessible manner.

Manuscript Preparation Guidelines for AJEG

Authors must use the official manuscript template available on the AJEG website for preparing their submissions.

Title Page

The **title page** should include the following details:

- **Title** of the article
- **Full name(s)** of all authors (first name, middle initial(s), and surname)
- **Affiliations** of the authors, including department or division, institution or organization, city, and country. Do not use abbreviations for affiliations.
- If multiple authors share the same affiliation, list all authors first, followed by the shared affiliation.
- **Email addresses** of all authors must be included.
- The **corresponding author** should be clearly identified with an asterisk (*).

Abstract and Keywords

The manuscript should begin with an **Abstract** of approximately **300 words**, clearly summarizing:

- The research problem
- The methods used
- Major findings
- Conclusions

Immediately following the abstract, list **up to five keywords or phrases** for indexing purposes as per the template provided.

Figures, Tables, and Symbols

- Special characters, mathematical symbols, and Greek letters not available on a standard keyboard must be created using the **Symbol** font.
- **Figures and tables** should be **embedded** at appropriate locations within the text **after the list of references**.
- After the manuscript is accepted, authors must also submit **figures as separate high-resolution files**.
- Figures should follow the formatting requirements outlined in the submission guidelines (e.g., TIFF format, 300–600 dpi, RGB/grayscale mode, single-layer).

Pagination, Line Numbering, and Equations

- Authors must insert both page numbers and continuous line numbers throughout the manuscript to facilitate the review process. Page numbers should appear in the footer of each page.
- Equations should be left-aligned, with reference numbers aligned to the right margin.
- For long equations, break the right side into approximately equal parts and align to the right. Place the equation number on the last line only.
- All equations must be numbered sequentially as they appear in the text.

Units

Use **SI units** throughout the manuscript. If alternative units are provided, they should appear in parentheses following the SI units.

Acknowledgments

Acknowledgments should be included before the list of References, and the title should read "Acknowledgments." Author/s should obtain a permission to acknowledge from all those mentioned in the Acknowledgements.

References

In the list of references, provide complete information of each reference material. Cite a symposium paper only from published proceedings. Do not cite an article or book only accepted for publication but not published. Do not use ibid. Please avoid excessive referencing.

Unpublished data, unpublished abstracts and personal communications should not be included in the reference list. Footnotes are not acceptable.

AJEG prefers maximum 60 references per article. The journal follows the Harvard system for citation, with author name/s and year of publication in parentheses, such as one author: (Hungr 2003) or Hungr (2003), two authors: (Doe and Morris 2009) or Doe and Morris (2009), and three authors or more: (Rahardjo et al. 2002) or Rahardjo et al. (2002).

Journal article

van Westen C.J., Rengers N. and Soeters R. (2003). Use of geomorphological information in indirect landslide susceptibility assessment. Natural Hazards, 30, 399–419.

Same author/s more than one journal articles of same year

Dahal R.K., Hasegawa S., Nonomura A., Yamanaka M. and Dhakal S. (2008a). DEM-based deterministic landslide hazard analysis in the Lesser Himalaya of Nepal. Georisk: Assessment and Management of Risk for Engineered Systems and Geohazards, 2(3), 161-178.

Dahal R.K., Hasegawa S., Nonomura A., Yamanaka M., Dhakal S. and Paudyal P. (2008b). Predictive modelling of rainfall-induced landslide hazard in the Lesser Himalaya of Nepal based on weights-of-evidence. Geomorphology 102 (3-4), 496-510.

Journal article with DOI

Hasegawa S., Dahal R.K., Yamanaka M., Bhandary N.P., Yatabe R. and Inagaki H. (2009). Causes of large-scale landslides in the Lesser Himalaya of central Nepal. Environ Geol 57, 1423–1434. doi:10.1007/s00254-008- 1420-z+

Journal article in press

Dahal R.K. and Hasegawa S. (2008). Representative rainfall thresholds for landslides in the Nepal Himalaya. Geomorphology, doi:10.1016/j.geomorph.2008.01.014, p 15 (in press)

Maps and pamphlets

Amatya K.M. and Jnawali B.M. (1994). Geological map of Nepal. Scale:1:1,000,000. Department of Mines and Geology, Kathmandu, Nepal

Book, authored

Dahal R.K. (2006). Geology for technical students. Bhrikuti Academic Publication, Kathmandu, 756 p.

Same author more than one book

Krahn J. (2004a). Seepage modeling with SEEP/W, an engineering methodology, 1st edn. Geo-Slope International Ltd, Alberta

Krahn J. (2004b). Stability modeling with SLOPE/W, an engineering methodology, 1st edn. Geo-Slope International Ltd., Calgary

Book, edited

Wohletz F. and Aaron G. (Ed.) (1992). Sedimentology. California Press, CA.

Book chapter

Ward T.J., Li R-M. and Simons D.B. (1981). Use of a mathematical model for estimating potential landslide sites in steep forested basin. In T.R.H. Davis, A.J. Pearce (Ed.) Erosion and sediment transport in pacific rim steep lands, International hydrological Science Publ No 132, (pp. 21-41). Institute of Hydrology, Wallingford, Oxon, UK.

Proceedings as a book

Sassa K. (1998). Recent urban landslide disasters in Japan and their mechanisms. In Proceedings of 2nd International Conference on Environmental Management, "Environmental Management'' (vol 1, pp. 47–58), Australia, 10–13 February, Elsevier, Amsterdam.

Proceedings with an editor but without a publisher

Rahardjo H., Leong E.C. and Rezaur R.B. (2002). Studies of rainfall-induced slope failures. In P. Paulus, H. Rahardjo (Ed.) Proceedings of the National Seminar, Slope 2002 (pp. 15–29). 27 April 2002, Bandung,

Proceedings without an editor but with a publisher

Doe S.-T. and Morris R.L. (1998). Rainfall-induced slope failures and damming of ravines. In Abstracts of international symposium on water- induced disasters, Tribhuvan University, Kathmandu, 4–9 June 1998.

Proceedings in media (CD, DVD, Pen drive) format

Yatabe R., Yagi N., Yokota K. and Bhandary N.P. (2000). Influence of expansive chlorite on the strength of weathered Green Rock at Mikabu Belt of Japan. Proceedings of International Conference on Geotechnical and Geological Engineering. Melbourne, Australia, 19–24 November 2000 (CD format)

Publicly available unpublished report

Wagner A. (1983). The principal geological factors leading to landslides in the foothills of Nepal: a statistical study of 100 landslides-steps for mapping the risk of landslides. HELVETAS-Swiss Technical Cooperation and ITECO-Company for International Cooperation and Development, unpublished.

Online document

Hungr O. (2003). Flow slides and flows in granular soils. In Proceedings of international workshop on occurrence and mechanisms of flows in Natural Slopes and Earth fills (15p.), Retrieved from http://www.unina2.it/flows2003/flows2003/articoli/Hungr-Flows.pdf. Accessed 15 Jan 2024.

Dissertation

Khanal R.K. (1991). Historic landslides of Nepal during 1902-1990 A.D., extent and economic significance, (M.Sc. Dissertation), Central Department of Geology, Tribhuvan University, Nepal, unpublished, 94p.

Standard or Patent name

ASTM D3385-03. (2003). Standard test method for infiltration rate of soils in field using double-ring infiltrometer. ASTM International, 100 Bar, Harbor Drive, west Conshohocken, 19428

Review and Production Process

All manuscripts submitted to AJEG undergo peer review. Accepted materials are subject to copyediting to ensure clarity, consistency, and adherence to journal standards. Authors will receive galley proofs of their article prior to publication and are expected to respond promptly to any editorial queries. Proof corrections must be limited to typographical or printer’s errors; substantial revisions or rewriting at the proof stage will not be permitted.

Page Charges

There is no page charge/s for papers submitted to the AJEG. The upper limit on length of a paper is approximately 35 manuscript pages, including tables and references. This limit may be exceeded at the discretion of the Editor-in-chief.

Online Submission

Please note that the online manuscript submission system is available through the journal’s official website. This system is essential for preparing and submitting your manuscript electronically to the Asian Journal of Engineering Geology via its web-based peer-review platform.

Manuscripts should be submitted at https://ajeg.nseg.org.np . The submission portal also allows authors to track the progress of their manuscript throughout the peer-review and editorial process.

Author should use given Template in the web site for preparation of manuscript.

Asian Journal of Engineering Geology, 2024, Vol. 1 No. 1 and 2, 1-6

Research Article **DOI: https://doi.org/10.64862/ajeg.112.01** **Open Access**

Determination of Terrain-Specific Restitution Coefficients and Rockfall Hazard Assessment in the Chaku Bazar of Nepal

Dhurba Tiwari[1]*, Brabin Sapkota[2], Praveen Upadhyaya Kandel[2] and Sunam Kumar Sharma[2]

[1]Seventy Seven D. International Pvt. Ltd, Sanepa, Lalitpur, Nepal
[2]Geotech Solutions International, Dhobighat, Lalitpur, Nepal

(*Corresponding E-mail: tiwaridhurba98@gmail.com)

Received: July 15, 2024, Accepted on November 05, 2024

Abstract: Many of Nepal's rapidly growing cities are located at the base of steep slopes, where rockfall hazards pose a significant threat. Rockfall issues have also been observed in Chaku Bazar, Sindhupalchowk, Bagmati Nepal, situated at km 102+000 along the Araniko Highway. The primary aims of this study were to determine the restitution coefficient of the material, stability analysis and to simulate rockfall at the steep slope in Chaku Bazar. The accuracy of rockfall simulations relies on the restitution coefficient. Initially, the normal and tangential restitution coefficients were calculated for 10 different rock boulders, varying in shape and composition using the Tracker Video analysis and modeling tool. The computed values for normal and tangential restitution coefficients were then used to simulate rockfall behavior using GeoRock 2D across four different sections, predicting rockfall trajectories and run-out distances. Geologically, the area is part of the Lakharpata Group of the Lesser Himalaya, characterized by calcareous rocks, primarily dolomite and schist. The normal restitution coefficient for vegetated rocky terrain was 0.25, while for solid rock it was 0.73. Likewise, the tangential restitution coefficient was 0.37 for grass-covered areas and 0.82 for rocky surfaces. The factor of safety of block for planar failure is 0.83, for wedge failure is 0.95 and for toppling failure is 1.35. After determining the restitution coefficients, the calculations revealed a maximum collision energy of 2576 kJ and a maximum bounce height of 4.6 meters.

Keywords: ***Block Analysis, GeoRock 2D, Hazard, Rockfall, Restitution Coefficient.***

Introduction

Rockfall is the natural downward movement of one or more detached blocks with small volumes, characterized by free fall, bouncing, rolling, and sliding (Varnes 1978) which pose threat to the environment and resulting in loss of life and property (Cruden and Varnes 1996 and Bunce et al. 1997). These rock blocks can be dislodged through various processes, including natural mechanisms such as freeze-thaw cycles (McCarroll and Pawellek 1998, Matsuoka and Sakai 1999 and Khatiwada and Dahal 2020), seismic events (Abebe et al. 2010), or by human activities such as slope excavation or earth-moving operations (Dorren 2003 and Vijayakumar et al., 2011). The steep topography, geological variations and tectonic activity within the small belt have accelerated the soil erosion and rockfall (Tiwari et al. 2022). The Rock fall incidents, recognized as a global hazard, pose challenges due to their unpredictable nature and the lack of precise analysis.

To the mark, Nepal has experienced numerous fatal rock fall incidents, notably along the Jogimara section of Prithvi Highway and the Narayanghat-Muglin Road during the 2016 monsoon. The Araniko Highway, crucial for trade with China, has witnessed an increase in rock fall incidents since the 2015 Gorkha earthquake (Dahal 2016), which caused extensive damage, including to the Upper Bhotekoshi Hydroelectric Project's penstocks. Thus, there is a pressing need for identifying rock fall hazard zones and conducting detailed studies to mitigate risks, safeguard lives, properties, and prevent significant economic losses.

The impact of the rockfall depends upon the estimation of trajectories, bouncing heights and the kinetic energies of the unstable blocks. These elements are frequently derived through the application of kinematic modeling techniques created using numerical codes like Colorado Rockfall Simulation Program (CRSP) or RocFall (Pfeiffer and Bowen 1989). The key input parameters influencing the estimated rockfall hazard in computer simulations are the coefficients of restitution. These parameters measure the energy loss that occurs when a block impacts the slope (Sabatakakis et al. 2015). The coefficients of restitution are divided into tangential (Rt) and normal (Rn) components relative to the slope. Two primary methods are used to determine these parameters: direct measurement through experimental tests, both in situ and in the laboratory (Azzoni and de Freitas 1995, Giani et al. 2004 and Chau et al. 2002), and back-analysis of natural or artificially triggered rockfalls (Evans and Hungr 1993). It has been observed that (Rn) values exceeding one have been recorded in both field tests (Bourrier et al. 2012, Spadari et al. 2012) and laboratory experiments (Asteriou et al. 2012 and Buzzi et al. 2012), as well as calculated through simulations (Bourrier et al. 2009) and by back-analysis methods (Paronuzzi 2009).

The research focus of the determination of restitution coefficient of the slope material and Rockfall Simulation at Chaku Bazar, Sindhupalchock, Bagmati Nepal.

Study Area

The study area is located in Chaku Bazar, within Bhotekoshi Rural Municipality of Sindhupalchowk district (27°53'2.3" N, 85°54'48.5"E) which site on cliff with an elevation of 1216 m from mean sea level. It is easily accessible from Kathmandu via the Araniko Highway, positioned at 102+000 km along of the highway (Figure 1). The rockfall hazards in this region pose a risk to the residents of Chaku Bazar and the Araniko Highway. Geologically, the area is part of the Lakharpata Subgroup within the Lakharpata Formation, characterized by fine-grained gray limestones, dolomitic limestones, and dolomite. The boulders of these rock type were the source for rockfall.

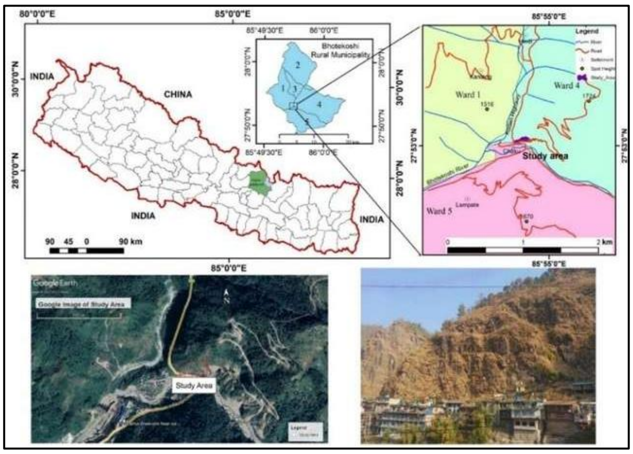

Figure 1, Location map of the study slope area.

Materials and Methods

This study experimentally evaluates the coefficient of restitution for boulders colliding with rock slopes under different impact conditions, followed by the calculation of their kinetic energy and re-bounce height at four distinct sections of the terrain. The method of data collection and interpretation is given in Figure 2 and describe as,

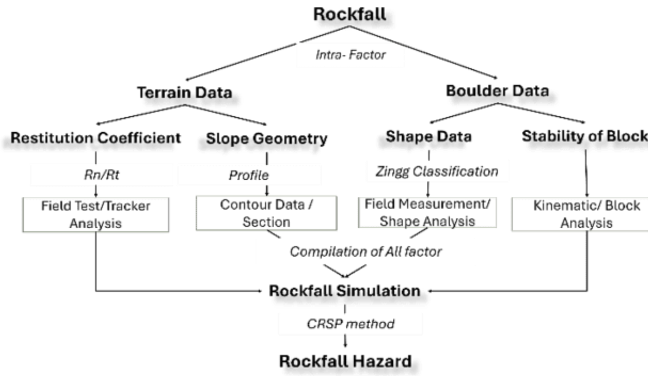

Figure 2, Methodological flow chart for the study.

Determination of restitution coefficient

Newton (1686) originally defined the coefficient of restitution (R_C) as the ratio of the rebound velocity to the incident velocity of two colliding particles (or small spheres) along the normal direction. The kinematic definition of the coefficient of restitution, has been generalized and extended to three dimensional collisions by Brach (1991) and Brach (1997).

$$R_C = \frac{V_{1n} - V_{2n}}{U_{1n} - U_{2n}} \qquad (1)$$

Where, V_{1n} & V_{2n} = normal components of rebound velocities, and U_{1n} &U_{2n} = normal component of initial velocities of two colliding bodies. The both normal and tangential component of the restitution coefficient has significant role on the velocities and trajectories of the falling block. Both normal and tangential components have determined by,

$$R_n = -\frac{V_{rn}}{V_{in}}, \qquad (2)$$

$$R_t = \frac{V_{rt}}{V_{it}} \qquad (3)$$

Where, V_{rn} and V_{in} are the magnitudes of the normal component of the rebounding and incoming velocities and V_{rt} and V_{it} are the magnitudes of the tangential component of the rebounding and incoming velocities. Each parameter has determined by using the following relations (Chau et al. 2002),

$$V_{rn} = \left(\frac{h}{T2} + \frac{1}{2} gT2\right) \cos \propto - \frac{L}{T2} \sin \propto \qquad (4)$$

$$V_{in} = \left(\frac{H}{T1} + \frac{1}{2} gT1\right) \cos \propto - \frac{S}{T1} \sin \propto \qquad (5)$$

$$V_{rt} = \left(\frac{h}{T2} - \frac{1}{2} gT2\right) \sin \propto + \frac{L}{T2} Cos \propto \qquad 6)$$

$$V_{it} = \left(\frac{H}{T1} + \frac{1}{2} gT1\right) \sin \propto + \frac{S}{T1} \cos \propto \qquad (7)$$

Where, g is the gravitational constant (i.e. 9.81 m/s^2) and H= y_1 - y_2; h= y_2 -y_3; s =x_1- x_2; L = x_2 -x_3; T_1 = t_2- t_1; T_2= t_3 -t_2.

To determine these parameters, ten blocks of varying shapes and sizes were selected and released from the top of the slope. The falling blocks were recorded on video, which was later analyzed using Tracker software to measure their velocity (Figure 3). After all the blocks had been dropped and the test area was deemed safe, the final positions of the blocks were recorded with coordinates, the impact depths were measured, and the sizes of the blocks were noted. Ranging rods and measuring tapes were used to measure and mark the distances traveled by the blocks. Data from Tracker, along with manual observations, were used to calculate the tangential and normal coefficients of restitution, with trigonometric formulas aiding in determining the blocks movement and restitution coefficients.

Kinematic Analysis

The discontinuities data were collected from the site and determined the major joint set by stereonet plot. The major joint set were used for the determination of the prominent failure type of the rock slope. After determining the prominent failure type, the block analysis for each failure type (Plane, wedge and toppling has determined. The plane failure analysis was conducted based on equations developed by Hoek and Bray (1981). Condition for calculation was external force zero ($a = T = 0$) and dry slope ($U = V = 0$).

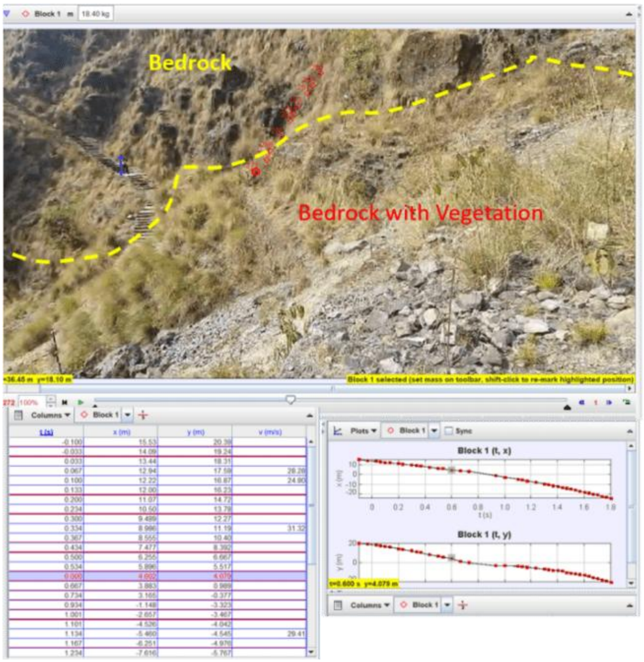

t (s)	x (m)	y (m)	v (m/s)
-0.100	15.53	20.39	
-0.033	14.09	19.24	
0.033	13.44	18.31	
0.067	12.94	17.59	28.26
0.100	12.22	16.87	24.90
0.133	12.00	16.23	
0.200	11.07	14.72	
0.234	10.50	13.79	
0.300	9.489	12.27	
0.334	8.986	11.19	31.32
0.367	8.555	10.40	
0.434	7.477	8.392	
0.500	6.255	6.667	
0.534	5.896	5.517	
0.600	4.602	4.079	
0.667	3.883	0.989	
0.734	3.165	-0.377	
0.934	-1.148	-3.323	
1.001	-2.657	-3.467	
1.101	-4.526	-4.042	
1.134	-5.460	-4.545	29.41
1.167	-6.251	-4.976	
1.234	-7.616	-5.767	

Figure 3, Tracker video analysis for determination of Restitution Coefficient (Rn and Rt).

$$\mathrm{FS} = \frac{\{\mathrm{cA}+[\mathrm{W}*(\cos\Psi_\mathrm{p})-\mathrm{U}-\mathrm{V}\sin\Psi_\mathrm{p}+\mathrm{T}\cos\theta\,]\tan\phi\}}{[\mathrm{W}(\sin\Psi_\mathrm{p}+\mathrm{a}\cos\Psi_\mathrm{p})+\mathrm{V}\cos\Psi_\mathrm{p}-\mathrm{T}\sin\theta\,]} \quad (8)$$

Where, c = cohesive strength of failure surface; A=area of failure surface; W=weight of sliding block; Ψ_p = inclination of failure plane; a = horizontal acceleration, blast or earthquake loading; U=uplift water force; V= driving water force; T = Tension in bolts or cables; θ = inclination of bolt or cable to normal to failure plane; ϕ = friction angle of failure surfaces; Z = depth of tension crack, H = height of slope face; Ψ_f = inclination of slope face; b = distance of tension crack from slope crest; γ_r = density of rock; γ_w = density of water; $\mathrm{Z_w}$ = height of water in tension crack.

Similarly for wedge failure, the empirical relation developed by Hoek and Bray (1981), has applied,

$$\mathrm{FS} = \frac{3}{\gamma_\mathrm{r}\mathrm{H}}(\mathrm{c_a X} + \mathrm{c_b Y}) + \mathrm{A}\tan\phi_\mathrm{a} + \mathrm{B}\tan\phi_\mathrm{b} \quad (9)$$

Where, $\mathrm{c_a}$ and $\mathrm{c_b}$ are the cohesive strengths of planes a and b, ϕ_a and ϕ_b are the angles of friction on planes a and b; γ_r is the unit weight of the rock; H is the total height of the wedge; X, Y, A and B are dimensionless factors which depend upon the geometry of the wedge.

The toppling failure analysis was conducted by using empirical relations formulated by Hoek and Bray (1981).

$$FOS = \frac{w\cos\theta.\left(\frac{t}{2}\right)}{w\sin\theta,\left(\frac{h}{2}\right)} = \frac{\frac{t}{h}}{\tan\theta} \quad (10)$$

Where, weight of the block, θ = inclination of slope, h= height of block and t is the thickness of block.

Rockfall simulation

The rockfall simulation has followed by CRSP method in GeoRock 2D Software which is easily available and widely used in the simulation of rock fall problems. The parameter required for the rockfall simulation were restitution coefficient of slope material, slope geometry and the boulder data. For the rockfall simulation, the restitution coefficient was used from previously determined values after field tests and tracker analysis.

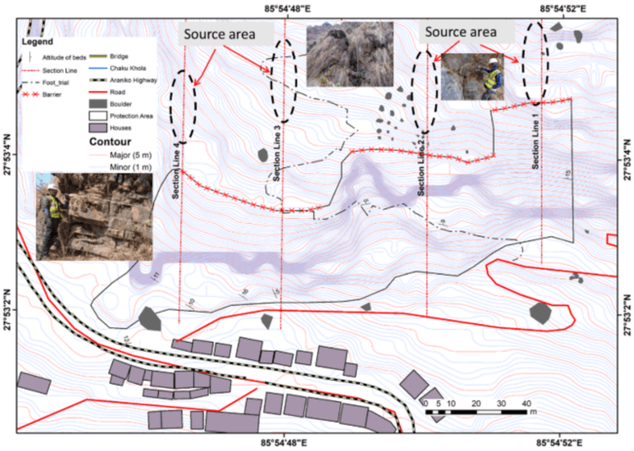

Figure 4, Slope geometry section line with source of loose rock boulders.

The cross-sectional profile of the slope, as shown in Figure 4 was developed based on contour data generated from a total station survey. The source area was determined based on field investigations and kinematic analysis to identify the mode of failure at the source. Boulder data, including the shape of the boulders, was determined through block analysis using major discontinuities and field measurements.

The rigid body approach of CRSP analyzes the impulse reaction of the rock during its brief contact with the slope to identify critical events such as slipping, sticking, and reversal behavior during both the compression and restitution phases. The normal coefficient of restitution is applied during these two contact phases to calculate the terminal impulse. Using this terminal impulse, the outgoing velocities at the contact point can also be determined.

Result and Discussion

Restitution coefficient

The normal and tangential coefficients of restitution were determined for ten different rock boulders, each varying in shape and lithology, to account for the diversity in rockfall behavior associated with different physical and material characteristics. The tangential coefficient of restitution for the bedrock varies from 0.77 to 0.87, which is in the range of standard values in dolomitic terrain. Similarly, the average normal coefficient for bedrock is 0.73. The average normal and tangential coefficient of restitution for bedrock with vegetation is 0.25 and 0.37 respectively (Figure 5).

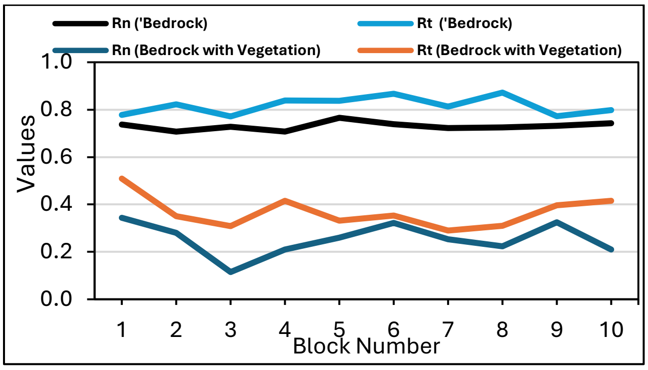

Figure 5, Result showing restitution coefficient of the bed rock terrain and grass with bedrock terrain.

Kinematic Analysis

The kinematic analysis of discontinuities data shows that the predominant type of slope failure of slope are wedge failure and plane failure. Block analysis, using the modified Hoek and Bray (1981) method, was conducted on a representative slope section to determine the factor of safety for a typical vulnerable block. The factor of safety of block for plane failure is 0.83, for wedge failure is 0.95, and for toppling failure is 1.35, which is given in Table 1 and Figure 7 which implies that the slope instability has created by the blocks.

Table 1, The determination of factor of safety of block with respect to prominent failure.

Plane Failure		Wedge Failure				Toppling Failure	
b	0.94	θna*2	89.11	φb	71	d	0.08
c	1.49	θnb*1	85.89	Phi	17.72	γ	26
γ	26	θna*nb	58.87	H	54.98	W	2.04
H	41	φi	46	γ	26	θ	85
z	8.67	θ24	72.85	C	0.517	t	0.5
φp	74	θ45	67.83	X	1.41	H	2.11
φf	85	θ35	50.11	Y	-1	**FOS**	**1.35**
ϕ	30	θ13	50.34	A	0.28		
A	1109.8	φa	70	B	0.28		
W	2442.3			**FOS**	**0.95**		
ROS	**0.83**						

Rockfall Hazard

The field measurement and discontinuities plot show that the size of the boulder is 2.4 m on average. The Zingg classification of the boulder data shows that the shape of the boulder is "disc" (Figure 8) which is used for the rockfall hazard simulation. The result shows that there is possibility of the rock slope failure. On varying the shape and size of the block, the factor of safety has increased. The rockfall simulation result shows that the rockfall hazard can be of maximum energy 15000 kJ to the settlement area of Chaku Bazar and Araniko Highway (Table 2).

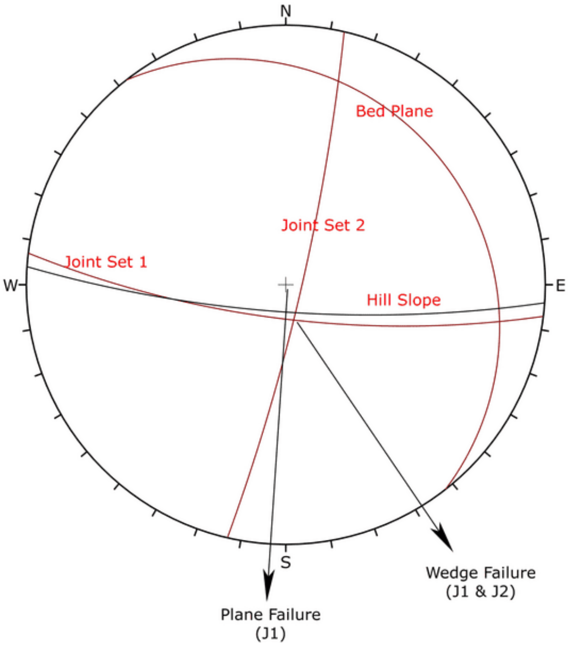

Bed Plane	J1	J2
(15°/052°)	(75°/187°)	(83°/103°)

Figure 6, Stereonet plot of discontinuities data for kinematic analysis in the Dips software.

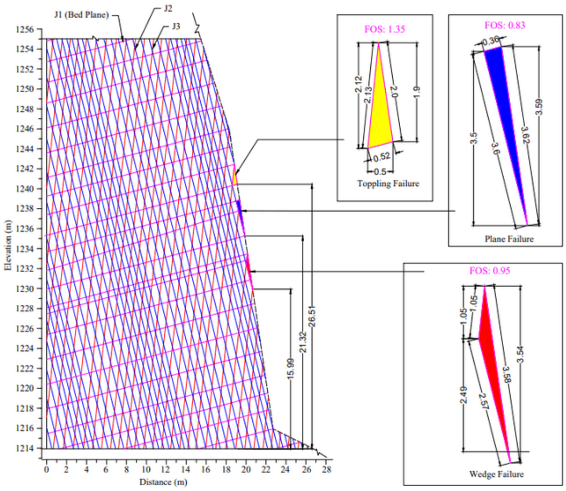

Figure 7, Rockfall analysis by stability of block at section of study slope.

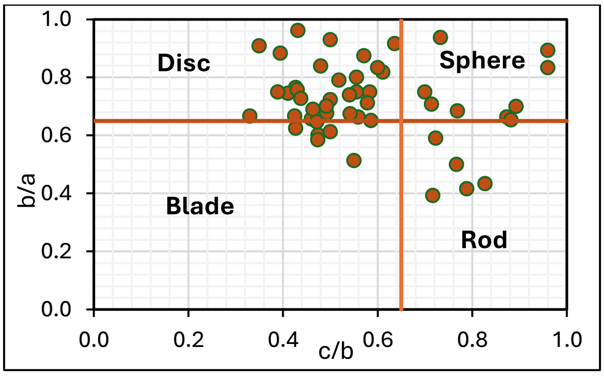

Figure 8, Zingg classification of the boulder data.

Similarly, the maximum run-out distance is estimated to be 160 meters, with a rebound height of up to 30 meters, due to the extremely steep terrain with slopes exceeding 80° (Table 2). The slope area is divided into three zones according to kinetic energy (Figure 9). The red zone implies high-energy zone while green zone indicates the low energy zone.

Table 2, Section wise rockfall simulation result.

Section	Energy	Max. Height	Run out
1	14000 kJ	24 m	140 m
2	15000 kJ	25 m	160 m
3	7000 kJ	30 m	160 m
4	6900	30 m	160 m

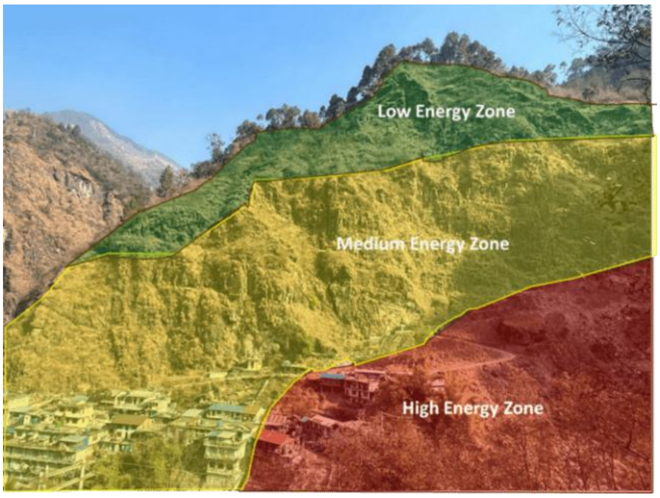

Figure 9, Hazard map of the studied slope according to rockfall and kinetic energy.

Conclusion

In this research, rockfall hazard assessment was carried out using field tests and simulations, leading to recommendations for significant stabilization measures. Kinematic analysis indicated a high likelihood of planar failure occurring at rock slope of Chaku Bazar in which factor of safety is less than 1, with notable chances of wedge and toppling failure. The analysis implies that the rock fall is significantly dependent on restitution coefficient and this value should be site specific. The findings highlight the elevated risk, particularly at the toe of the slope, where the highway road is the primary element exposed to danger.

Acknowledgment

Special thanks to Geotech Solutions International for Software and funding the project. We are thankful to two anonymous reviewers for their comments and suggestions, which helped to rectify the manuscript.

References

Abebe B., Dramis F., Fubelli G., Umer M. and Asrat A. (2010). Landslides in the Ethiopian highlands and the Rift margins. Journal of African Earth Sciences, 56 (4-5), 131-138. https://doi.org/10.1016/j.jafrearsci.2009.06.006

Asteriou P., Saroglou H., Tsiambaos G. (2012). Geotechnical and kinematic parameters affecting the oefficients of restitution for rock fall analysis. Int J Rock Mech Min Sci 54:103–113. https://doi.org/10.1016/j.ijrmms.2012.05.029

Azzoni A. and De Freitas M.H. (1995). Experimentally gained parameters, decisive for rock fall analysis. Rock mechanics and rock engineering, 28 (2), 111-124. https://doi.org/10.1007/BF01020064

Brach R.M. (1991). Vehicle dynamics model for simulation on a microcomputer. International Journal of Vehicle Design, 12 (4), 404-419. https://doi.org/10.1504/IJVD.1991.061757

Brach R.M. (1997). An analytical assessment of the critical speed formula (No. 970957). SAE Technical Paper. https://doi.org/10.4271/970957

Bunce C.M., Cruden D.M. and Morgenstern N.R. (1997). Assessment of the hazard from rock fall on a highway. Canadian Geotechnical Journal, 34 (3), 344-356. http://dx.doi.org/10.1139/cgj-34-3-344

Bourrier F., Dorren L., Nicot F., Berger F. and Darve F. (2009). Toward objective rockfall trajectory simulation using a stochastic impact model. Geomorphology 110: 68–79. http://dx.doi.org/10.1016/j.geomorph.2009.03.017

Bourrier F., Berger F., Tardif P., Dorren L., Hungr O. (2012). Rockfall rebound: comparison of detailed field experiments and alternative modelling approaches. Earth Surface Processes and Landforms 37 (6): 656–665. http://dx.doi.org/10.1002/esp.3202

Buzzi O., Giacomini A. and Spadari M. (2012). Laboratory investigation on high values of restitution coefficients. Rock mechanics and rock engineering, 45, 35-43. http://dx.doi.org/10.1007/s00603-011-0183-0

Chau K.T., Wong R.H.C. and Wu J.J. (2002). Coefficient of restitution and rotational motions of rockfall impacts. International Journal of Rock Mechanics and Mining Sciences, 39 (1), 69-77. https://doi.org/10.1016/S13651609(02)00016-3

Cruden D.M. and Varnes D.J. (1996). Landslide types and processes, transportation research board, us national academy of sciences, special report, 247: 36-75.

Dahal R.K. (2016). Initiatives for rockfall hazard mitigation in Nepal. Bulletin of Nepal Geological Society, 33, 51-56.

Dorren L.K. (2003). A review of rockfall mechanics and modelling approaches. Progress in Physical Geography, 27 (1), 69-87. http://dx.doi.org/10.1191/0309133303pp359ra

Evans S.G. and Hungr O. (1993). The assessment of rockfall hazard at the base of talus slopes. Canadian geotechnical journal, 30 (4), 620-636. https://doi.org/10.1139/t93-054

Giani G.P., Giacomini A., Migliazza M. and Segalini A., (2004). Experimental and theoretical studies to improve rock fall analysis and protection work design. Rock Mechanics and Rock Engineering, 37, 369-389. https://doi.org/10.1007/s00603-004-0027-2

Hoek E. and Bray J. D. (1981). Rock slope engineering. The Institution of Mining and Metallurgy, 402.

Khatiwada D. and Dahal R.K. (2020). Rockfall hazard in the Imja glacial Lake, eastern Nepal. Geoenvironmental Disasters, 7 (1), 29p. https://doi.org/10.1186/s40677-020-00165-9

Matsuoka N. and Sakai H. (1999). Rockfall activity from an alpine cliff during thawing periods. Geomorphology, 28 (3-4), 309-328. https://doi.org/10.1016/S0169-555X(98)00116-0

McCarroll D. and Pawellek F. (1998). Stable carbon isotope ratios of latewood cellulose in Pinus sylvestris from northern Finland: variability and signal-strength. The Holocene, 8 (6), 675-684. https://doi.org/10.1191/095968398675987498

Paronuzzi P. (2009). Rockfall-induced block propagation on a soil slope, northern Italy. Environmental geology, 58, 1451-1466. http://dx.doi.org/10.1007/s00254-008-1648-7

Pfeiffer T.J. and Bowen T.D. (1989). Computer simulation of rockfalls. *Bulletin of the association of Engineering Geologists*, *26* (1), 135-146. https://doi.org/10.2113/GSEEGEOSCI.XXVI.1.135

Sabatakakis N., Depountis N. and Vagenas N. (2015). Evaluation of rockfall restitution coefficients. In Engineering Geology for Society and Territory, Landslide Processes, Springer International Publishing, 2, 2023-2026. https://doi.org/10.1007/978-3-319-09057-3_359

Spadari M., Giacomini A., Buzzi O., Fityus S. and Giani G.P. (2012). In situ rockfall testing in new south Wales, Australia. International Journal of Rock Mechanics and Mining Sciences, 49, 84-93. https://doi.org/10.1016/j.ijrmms.2011.11.013

Tiwari D., Kandel S. and Thapa P. B. (2022), Assessment of Soil Erosion in Bhanu Municipality of Tanahun District, Western Nepal, Bulletin of Nepal Geological Society, 39, 125-129.

Varnes D.J. (1978). Landslides-Analysis and Control. National Academy of Sciences, Transportation Board Special Report, 176, 11-33.

Vijayakumar S., Yacoub T. and Curran J. (2011). A study of rock shape and slope irregularity on rock fall impact distance. 45th US Rock Mechanics/Geomechanics Symposium, 2011. American Rock Mechanics Association.

Asian Journal of Engineering Geology, 2024, Vol. 1 No. 1 and 2, 7-16

Research Article DOI: https://doi.org/10.64862/ajeg.112.02 Open Access

Engineering Geological Challenges Following the 2024 Noto Earthquake, Japan

Ashis Acharya[1]*, Anjila Babu Malla[1, 2], Sweta Guragain[1], Ranjan Kumar Dahal[3], Shuichi Hasegawa[4]

[1]Graduate School of Natural Science and Technology, Shimane University, Matsue, Japan
[2]Geotech Solutions International, Dhobighat, Lalitpur, Nepal
[3]Central Department of Geology, Tribhuvan University, Kirtipur, Kathmandu, Nepal
[4]Center of Crisis Management Advanced Education and Research, Kagawa University, Takamatsu, Japan

*(*Corresponding E-mail: ashisacharya648@gmail.com)*

Received: September 06, 2024, Accepted on December 11, 2024

Abstract: The 2024 Noto Peninsula (Noto-Hanto) earthquake significantly impacted infrastructure and communities in Central Japan, unveiling critical engineering geological challenges. To our knowledge, this paper presents the first systematic field survey conducted eight months after the mainshock, focusing on the post-disaster phenomenon and their recovery states. Through ground visits, satellite imagery analyses, and high-resolution DEM differencing, we identified persistent deep-seated gravitational slope deformation (DGSD) undermining tunnel stability, land uplift, structural collapses from soil liquefaction, and several landslides, with rural areas experiencing severe impacts. Our observations reported that the crustal uplift has permanently altered hydrological regimes and DGSD remains active beneath major tunnels, inducing tunnels spalling. Slope failures have progressed under cumulative rainfall loading, and tunnel linings show evolving structural distress linked to both DGSD and residual seismic damage. Lateral spreading, ground upheaval, ground settlement, sinking of utility poles, and the presence of sand ejecta are found as the major indicators of liquefaction. The study also evaluates the efficacy of current mitigation and restoration efforts. The Ishikawa`s structured, community-focused model demonstrates a clear path toward more efficient, resilient recovery, despite lingering delays in damage repair work. This study further emphasizes the significance of proactive, long-term disaster risk reduction to minimize future earthquake-related impacts.

Keywords*: **The 2024 Noto Earthquake, Post-disaster Assessment, Seismic hazards, Liquefaction, Landslides.***

Introduction

On January 1, 2024, as the people of the Noto Peninsula were celebrating the New Year, a sudden and powerful Mw7.5 earthquake with an epicenter at a depth of 16 kilometers struck, turning a joyful day into a tragic one (USGS 2024). Such a strong tremor was caused by a large thrust faulting, up to nearly 10 meters of slip, that expanded more than 150 kilometers along the fault zone (Fukushima et al. 2024). Figure 1 shows the tectonic setting around Japan and the location of the 2024 Noto earthquake's epicenter. The intense seismic activity caused significant crustal deformation and triggered regional cascading hazards (Fukushima et al. 2024, Gomez 2024 and Kataoka et al. 2024).

Two factors made this earthquake unusual: (a) an active seismic swarm resulting from the upward migration of crustal fluids and (b) much larger shaking than expected for an earthquake of its size and depth (Toda and Stein 2024). This unusual event has been linked to the accumulation of underground fluids due to a reverse fault stress field, as suggested by the focal mechanism analysis (Ishikawa and Bai 2024). The cracks in the earth's crust were oriented horizontally as the fluids flowing underground in deep areas could not rise and spread over a wide area in the horizontal plane. A recent geochemical study provided insight into the upwelling of deep fluids from the uppermost mantle that triggers the seismic swarm activity. The noble gases and their isotopes have been used as geochemical indicators to determine the origin of the fluids associated with the swarms and their upwelling. Gas samples collected from boreholes around the seismic source region are characterized by anomalously high 3He/4He ratios (~3.9 RAcor), indicating infiltration of mantle fluids from the subcrustal lithosphere (Umeda et al. 2024).

The major earthquake and subsequent tremors caused several geological engineering issues, including land uplift, structural collapse due to soil liquefaction, tunnel collapses, and landslides (Kataoka et al. 2024). The earthquake caused the collapse of old wooden houses with heavy roofs. The highways, railways and Noto airport runway were damaged. The earthquake induced many slope failures along the steep shores and mountainous terrain. These impacts are discussed in detail in the report available (Suppasri et al. 2024).

Although several rapid response studies documented the immediate impacts of the 2024 Noto earthquake (e.g., Suppasri et al. 2024; Ishikawa et al. 2024), no published report has evaluated the post-disaster state of the affected region. To address this gap, we conducted a focused field excursion on August 3-4, 2024, approximately eight months after the main shocks, during which we visited key sites across Ishikawa Prefecture to document engineering geological challenges and ongoing recovery efforts. The material presented here synthesizes publicly available data released by national and international earthquake institutes, mass media reports, and the author's field observations and measurements. To our knowledge, this is the first systematic survey of post-disaster phenomena in the Noto Peninsula at an eight-month interval. Because our focus was on analyzing post-disaster state and secondary hazard evolution of the affected area rather than exhaustive damage mapping, this paper highlights key sites where liquefaction-induced damages, sustained crustal uplift, and deep-seated gravitational slope deformation (DGSD) are the major issues that continue to threaten infrastructure, livelihoods, and the environment.

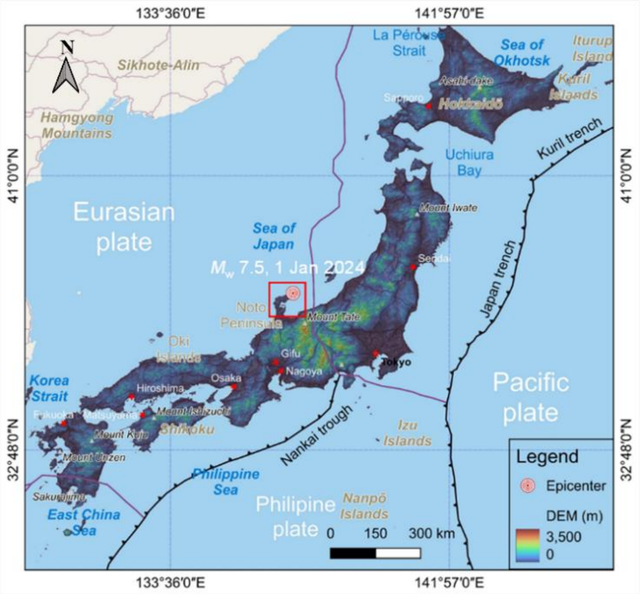

Figure 1, Tectonic setting in and around Japan.

Engineering Geological and Seismological Context

Japan has a very complex tectonic setting resulting from the convergence of several tectonic plates. Philippine Plate subducting beneath the Eurasian Plate at Nankai Trough and the Pacific Plate subducting beneath the North American Plate at Japan Trench has caused several major earthquakes and tsunamis (Seno et al. 1993). The Noto Peninsula is the largest Peninsula along Japan's Sea, situated at the convergence of the Eurasian and Pacific Plates. It extends towards the northeastern part, characterized by low-relief erosion surfaces and marine terraces. The geological framework of the Peninsula is dominated by pre-tertiary basement rock, primarily composed of Hida metamorphic rocks, and the Tertiary Formation is composed of Funatsu granitic rocks. Exposed basement rocks characterize the southern region, whereas Neogene formations dominate the central and northern parts of the Peninsula, demonstrating the geological transition from older to younger succession (Honda et al. 2008).

The Noto Peninsula has a history of seismic activity and has been subjected to complex tectonic processes. Four significant events have been recorded in this region, including coseismic uplift in 1025-1235, probable aseismic motion in 1430-1655, coseismic uplift associated with a pair of ca. Mw6.4 earthquakes in 1892 and Noto earthquake Mw6.7 in 2007 before the 2024 Noto earthquake (Shishikura et al. 2009). Several research studies have revealed the presence of active fault systems that traverse the Noto Peninsula. During this field observation, an active fault of the surface earthquake was observed along the Wakayama River in the northern part of Suzu city (Figure 2).

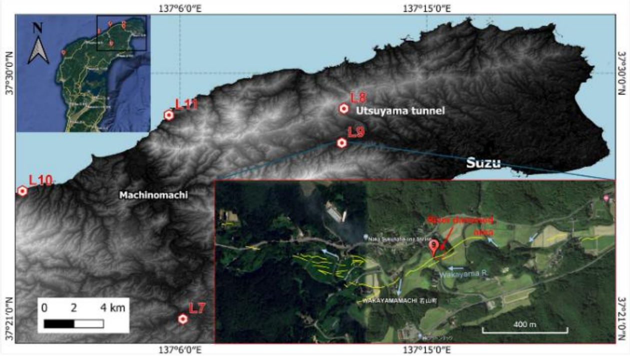

Figure 2, Surface earthquake active faults along the Wakayama River in the northern part of Suzu city (yellow line indicates active faults from Geospatial Information Authority of Japan 2024).

A series of minor to medium-sized earthquakes followed by aftershocks in the same area over a short period without a main event are recognized as earthquake swarms. Umeda et al. (2024) mentioned that the 2024 Noto Earthquake followed a prolonged period of intense earthquake swarms that had been ongoing beneath the northeastern part of the Peninsula for more than five years. Multi-year cluster-like pattern with shorter inter-event times has been observed during the swarm, which originates in the southern part of the Peninsula and it migrates towards the northeastern region along the Noto Peninsula (Wang et al. 2024). Additionally, they also discussed the occurrence of low-frequency seismic tremors within the region resulting from volcanic or hydrothermal activity beneath the surface.

Field Survey and Methodology

Eight months after the main shock, we conducted a comprehensive two-day field survey across the earthquake-affected regions of Ishikawa Prefecture. Our approach combined direct site visits and aerial imagery analysis to evaluate the seismic impacts on infrastructure and natural landscapes. This integrated methodology enabled us to investigate the scientific and engineering geological dimensions of the damage caused by the earthquake. Table 1 presents the data source used to prepare various thematic layers.

During our survey, we assessed the extent of damage and evaluated the progress of restoration efforts. Several maps were created within the QGIS environment, allowing us to visualize and interpret the observed damage more effectively. A 10 m DEM from the Geospatial Information Authority of Japan was used to overlay point data on the collapsed areas. We recorded the coordinates of damaged homes, road blockages, and fissures, measured visible displacement when possible, and photographed each site for later georeferencing. When debris blocked access, we relied on aerial imagery to identify additional slides and estimate their extent. In addition to our field observations, we critically reviewed previously published scientific articles and news reports from various media outlets to comprehensively understand the situation.

Table 1, Summary of tools, data sources, resolutions, and observation types used during the field survey

Tools and techniques	Source	Resolution/accuracy	Purpose
Digital elevation model (DEM)	Geospatial Information Authority of Japan (GSI)	10 m × 10 m grid	Map collapse zones, uplift, and subsidence
QGIS	QGIS 3.34	10 m×10 m grid	Create thematic maps and layer integration
Landslide topography distribution map	National research institute for earth science and disaster resilience	1:50,000 (landslides of ≥150 m width are only presented)	Analyze landslide distribution
Prefecture boundary	Geospatial Information Authority of Japan	n/a	Provide administrative boundary
Literature and media review	Peer-reviewed papers, local news outlets	n/a	Contextualized field data against initial rapid-response findings, verified timelines of recovery efforts and identified gaps in existing reports

Key Engineering Geological Issues

Soil liquefaction and associated damage

Liquefaction emerged as a major geotechnical concern in most of the earthquake-affected areas. It generally occurs when seismic vibrations destabilize loosely packed, water-saturated fine sand to silt sediments near the surface, significantly reducing ground strength. The major indicators of liquefaction are shown in Table 2. Inland regions of the Noto Peninsula, containing sand deposits from nearby dunes, were severely impacted by liquefaction due to the strong tremor. Along the coast, fine sand susceptible to liquefaction seems to have been carried by seasonal winds from the Sea of Japan. In contrast, on the landward side, where winds are blocked, fine sand was likely deposited in hilly regions, making the ground on the landward side more vulnerable to liquefaction compared to the seaside (Suppasri et al. 2024).

In Uchinada Town, the Saida Bridge has collapsed due to ground subsidence, disrupting the connection between the structure and the ground (Figure 3). The area, a floodplain located at the neck of Kahokugata Lagoon, has experienced significant subsidence due to sand liquefaction. Traffic on this bridge has been completely halted since the event. Lateral stress caused the bridge's northern side to pop up, displacing the abutment with a 36 cm lateral crack toward the south and a vertical movement of 12 cm, leading to the buckling of the bridge's middle section, which remains visible today. Figure 4 further illustrates liquefaction-induced engineering geological issues. Mizuno et al. (2024) reported the damage to the twin bridges (Naka-Noto Agriculture Bridge and Noto Island Ohashi Bridge) that connect Noto Island and the Peninsula. Additionally, a two-day emergency survey conducted using a microtremor array revealed ground shaking lasting approximately 4–5 minutes, which resulted in several liquefaction-induced damages in Uchinada Town. These included lateral spreading over approximately 2.7 hectares, ground upheaval, ground settlement, lateral displacement in the northwest to southwest direction, sinking of utility poles, and the presence of sand ejecta.

During the 2011 Great East Japan Earthquake, liquefaction was observed in reclaimed lands and old river channels. However, in the case of the 2024 Noto earthquake, liquefaction occurred in areas where sand deposits and sand dunes had accumulated, particularly on the landward side, making the land more susceptible to subsidence and dry slope failure where most of the structural damage resulted from the liquefaction of deeper sandy strata. This phenomenon was especially damaging in Uchinada town.

Figure 3, Damages in the Saida Bridge, Uchinada (Bridge offset vertically over tens of centimeters) (date of photographs taken: August 3, 2024).

According to Kataoka et al. (2024), liquefaction induced by this earthquake can be compared to that of the Niigata Earthquake in 1964, as both events exhibited liquefaction caused by seismic waves interacting with a combination of various geomorphic and geological factors.

Ground uplift and coastal changes

In December 2020, a seismic swarm began in the Noto Peninsula, initially confined to a small area associated with upwelling fluids through a shallow fault zone at a depth of around 16 km (Nishimura et al. 2023). This activity escalated significantly with a Mw6.5 earthquake in 2023, linked to the same mechanism (Kato 2024).

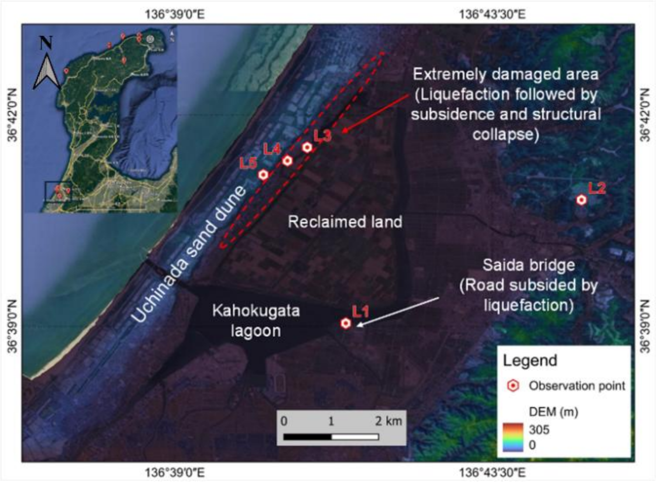

Figure 4, Liquefaction-related engineering issues observed along the coast of Saidamachi, Iwasaki, and Midorigaoka (L1 to L5 represents the observation site location).

The fifty seconds of violent shaking on the Noto Peninsula has uplifted and shifted the land northwest. The field observations indicated that the seafloor in the western part of Wajima City has been uplifted by approximately 4 m, resulting in the formation of a new marine terrace (Figure 5). This uplift was also confirmed by 2.5 D analysis, pixel offset analysis, and SAR interferometry analysis conducted by the Geospatial Information Authority of Japan using ALOS-2 data (Geospatial Information Authority of Japan 2024). The presence of wave-cut terraces and cliffs further evidences the extent of coastal uplift. Additionally, sea organisms such as oysters, bivalves, gastropods, and shellfish that were attached to the seawall and uplifted clearly indicate the pre-earthquake sea level, which can be observed at the Kaiso fishing port.

Coseismic crustal deformation caused by the 2011 Great East Japan Earthquake resulted in horizontal displacements of up to 5 m and vertical displacements of approximately 1 m near the epicenter (Kamiyama et al. 2017). Similarly, the 2016 Kumamoto Earthquake on Kyushu Island induced horizontal displacements of about 1.6 m and subsidence of nearly 2 m, as determined through Phased Array type L-band Synthetic Aperture Radar-2 (PALSAR-2) pixel tracking and Interferometric Synthetic Aperture Radar (InSAR) analyses (Himematsu and Furuya 2020). Global Navigation Satellite System (GNSS) observations recorded around 2 m of southwest-directed displacement and 1.3 m of uplift in Wajima. Meanwhile, Advanced Land Observing Satellite-2 (ALOS-2) data revealed 4 m of uplift and 2 m of westward displacement in Wajima City, along with 2 m of uplift and 3 m of horizontal displacement in northern Suzu City. In Suzu's northern region, reverse faulting caused approximately 2 m of land uplift, elevating the Wakayama River bed and leading to the damming of the river, which has since formed a preserved pond. These crustal deformations are part of a series of active faults distributed along the Wakayama River, which crosses its meandering path. At one observation site in Suzu City, the fault intersects the road perpendicularly, emphasizing the geomorphic impact of the earthquake-induced surface ruptures (Figure 6).

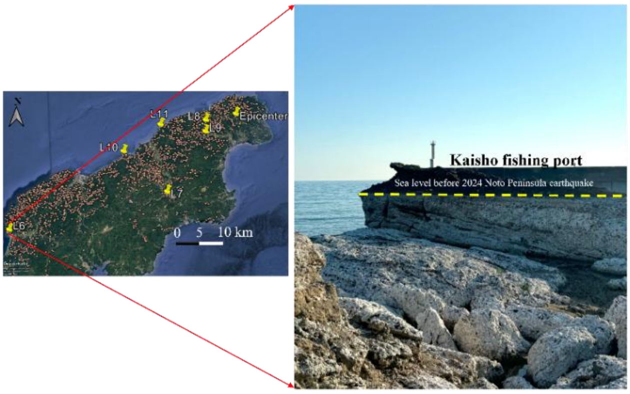

Figure 5, Kaiso fishing port uplifted by the Noto Peninsula Earthquake (date of photographs taken: August 3, 2024).

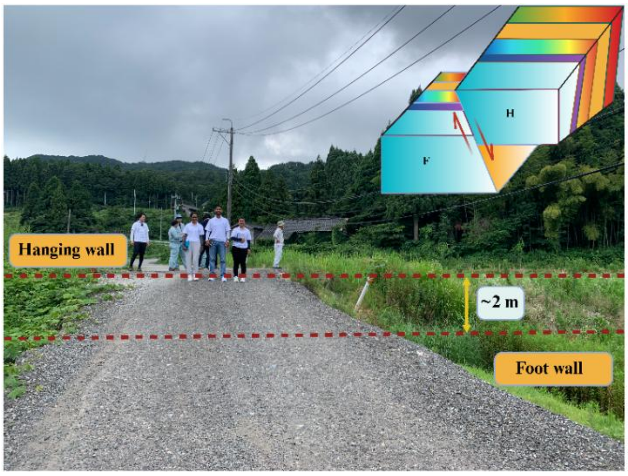

Figure 6, Land uplift of approximately 2 m by reverse faulting along the Wakayama River in Northern Suzu city (F and H represent footwall and hanging wall, respectively) (date of photographs taken: August 4, 2024).

Structural Collapse and Tunnel Failure

The Noto region experienced significant damage to structural stability due to the severe shaking of the earthquake, as well as the impacts of liquefaction and landslides, reminding of prior calamities such as the Haiti earthquake in 2010 (DesRoches et al. 2011), the Gorkha earthquake in 2015 (Liu et al. 2021), and the Kumamoto earthquake in 2016 (Setiawan et al. 2017). This study assessed damage to houses, indicating that the typical architectural style comprises wooden structures with timber mud walls and dark roof tiles. Numerous wooden houses either completely collapsed or incurred significant damage. Traditional two-story timber-framed houses experienced considerable damage during the 2024 Noto earthquake due to lateral movement, analogous to the destruction witnessed during the Kobe earthquake in 1995 (Yamazaki and Murao 2000) and the Tohoku-Oki earthquake in 2011 (Uchida and Bürgmann 2021).

On August 21, the official website of Ishikawa Prefecture announced updated damage statistics: 5,190 buildings collapsed, 16,231 residences sustained partial damage, and 60,426 structures displayed varying levels of damage across the Prefecture (Disaster Prevention, Safety and Security, Ishikawa Prefecture, 2024). In the Wajima and Suzu regions, many houses were destroyed or significantly tilted due to substandard construction practices. In the Uchinada region, numerous residences were damaged due to subsidence, lateral spread, and slope failures induced by liquefaction. Figure 7 illustrates some representative collapsed wooden buildings observed in the study area. The Saida Ohashi Bridge in Uchinada has been unusable due to lateral displacement caused by liquefaction. This phenomenon has similarly impacted other notable structures, including the Noto Island Ohashi Bridge and the Twin Bridge linking Noto Island with the Peninsula (Mizuno et al. 2024).

Figure 7, (a) Completely collapsed building along Wajima city; (b) tilted building; (c) building inspection certificate; and (d) inspection certificate attached to a building suffered with uplift and subsidence (date of photographs taken: August 3, 2024).

In Japan, mountain tunnels are constructed with earthquake-resistant stability; however, earthquakes with great magnitude result in either fully buried or unstable concrete tunnel lining. In the case of mountainous tunnels, earthquakes provoke landslides and damage the tunnel (Pai and Wu 2021). Otani tunnel (782 m length and 6.5 m width) is part of the Otani road (7.8 km), a National Route R249 in Suzu city, closed in many sections after the earthquake. The Otani tunnel was constructed within a DGSD zone in the Utsuyama region. Deep-seated landslides including DGSD and shallow slope failures, are primarily triggered by strong ground shaking. The 2024 Noto earthquake triggered a landslide around the area, disturbing the stability of the Otani tunnel resulting in the tunnel spalling about 100 m. The movement caused by the earthquake triggered the landslide and moved the whole mass laterally around 40 cm on the roadway towards the Karasugawa loop bridge. The spalled tunnel lining concrete was kept in front of the tunnel mouth on the roadside. Even eight months after the disaster, the expressway connecting Suzu City and Otani-Cho remained obstructed due to the tunnel collapse and slope on R249. Likewise, Maura-machi in Suzu City is one of the disaster-struck locations that suffered from a large-scale collapse near the Osaka tunnel on National Highway 249. The tunnel entrance is completely obscured by the debris from the landslides and slope failure. The condition of the Osaka tunnel can be observed before and after the earthquake of 2024. The 2024 Noto earthquake has majorly damaged roads such as National Highway 249 and Prefectural Road 1, which are partially closed and take time to be repaired fully.

After the earthquake, the landslide in the Utsuyama area impacted on the stability of the Otani tunnel, leading to the tunnel liner spalling (Figure 8). The spalled lining materials have been mocked out of the tunnel and kept on the roadside. The landslide caused the ground to slip laterally around 40 cm on the road and the Otani loop bridge (Figure 8d).

Figure 8, (a) Otani tunnel damaged by the sliding mass; (b) schematic diagram of liner spalling; (c) concrete liner mocked out from the tunnel; and (d) lateral slip observed along the roadside near the tunnel entrance (date of photographs taken: August 4, 2024).

The route between Suzu City and Otani-Cho remains closed due to the tunnel collapse, even eight months after the disaster. Similarly, the Osaka Tunnel on the northwest side of Mauramachi has been entirely covered by landslide debris and slope failure, rendering the tunnel entrance unrecognisable today (Figure 9).

Figure 9, Collapsed Osaka tunnel before and after the 2024 Noto earthquake [date of photograph taken (after): August 4, 2024].

Earthquake-induced landslides

The 2024 Noto earthquake has triggered numerous landslides, some of which were examined during field investigations (Figure 10). Emergency aerial images from January 2 2024, revealed approximately 930 coseismic landslides in mountainous and coastal regions, with a mean area of 5,353 m^2 and the largest one covering 373,962 m^2 (Gomez 2024). In total, the 2024 Noto earthquake caused over 2,300 landslides across a large area. Although this total is substantial, it is comparatively lower than other recent events of similar or greater magnitude: the 2002 Mid-Niigata Prefecture earthquake (>5,000 landslides), the 2018 Hokkaido Iburi earthquake (~6,000 landslides) (Loi et al. 2024), the 2016 Kumamoto earthquake (~3,467 landslides) (Xu et al. 2017), and the 2011Tohoku earthquake in 2011 (~3,477 landslides) (Wartman et al. 2013). Table 2 compares the sediment-related disasters triggered by the 2024 Noto earthquake with previous major earthquakes.

Earthquake-induced landslides can be categorized into several types, including rock falls, shallow landslides and dry debris flows, deep-seated landslides, and cut-fill slope failures, as described by Dahal (2015). In the study area of Wajima City, numerous deep-seated landslides, typically characterized by subsidence and the spreading of the upper part of a rock slope, along with outward movement or bulging at the base's slope, were observed. These landslides have also blocked the highway, necessitating the construction of alternative transportation routes. In Tsubata, Kahoku District, a significant landslide displaced a large mass of earth, exposing the foundations of houses and increasing their vulnerability. To mitigate further damage, plastic sheeting has been applied to the exposed land to prevent rainfall infiltration, thereby reducing the risk of additional movement or collapse. Areas prone to landslides face a high risk of secondary disasters due to future rainfall on unstable sediment and driftwood accumulated on slopes and in mountain streams. Consequently, the government actively implements emergency landslide countermeasures in these high-risk areas.

Earthquake-induced sediment movement poses a critical hazard in seismic regions, as intense ground shaking can trigger landslides, debris flows, and large-scale hillslope failures. The 2024 Noto earthquake caused around 420 cases of sediment movement within the Ishikawa Prefecture, 18 in Niigata Prefecture, and 13 in Toyama Prefecture, which resulted in numerous casualties damaging 57 infrastructures completely, 33 destroyed partially and 17 partially damaged (Ohno et al. 2024). Recent study also identified hillslope slumps exceeding 15 km in spatial extent; the first time such large-scale slumps and their associated toe scarps were quantified using satellite imagery (Fukushima et al. 2024). A four-day field investigation by the International Consortium on Geo-disaster Reduction (ICGdR) team revealed that most coseismic landslides in the affected area were controlled by preexisting geological features, such as large joint systems or secondary faults within original slopes, and predominantly occurred in mudstone units (Peng et al. 2025). Fukushima et al. (2024) documented meter-scale slope movements along flexural faults and activation of secondary inland faults, indicating synchronized ruptures.

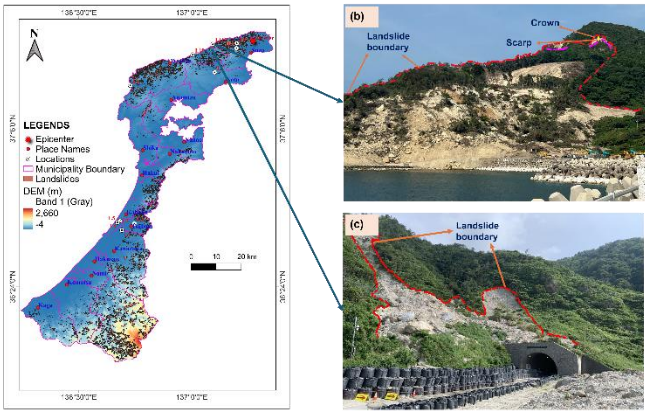

Figure 10, (a) Landslide distribution map along the Noto Peninsula; (b) large landslide mass covering the Osaka tunnel entrance; and (c) tunnel damaged by the landslide mass (date of photographs taken: August 4, 2024).

Cut and fill slope failures are also serious engineering concerns in the affected regions. Many roadside slopes in mountainous areas have suffered from these failures, primarily due to improper excavation practices and the instability to place or filled material on the slopes. Poor compaction and weathered-filled materials might have caused the fillings to slide downward. Another reason for this slide could be ~40 mm/day precipitation the day before the earthquake occurred. Road pavement buckling and lifting during earthquakes is very common in cut-and-fill engineering practices, which can lead to differential settlement. A similar pattern of extensive damage was observed during the 2016 Kumamoto earthquake, where the road pavements were constructed on liquefiable soil or fill materials experienced differential settlement, which created an undulating structure in the pavement (Kuribayashi et al. 2021).

Evaluating the Road to Recovery: Mitigation and Restoration Efforts

The aftermath of the 2024 Noto earthquake has left intensely damaged Ishikawa Prefecture with extensive recovery challenges. The direct field observations indicated that the damage repair progress has been markedly slower than in previous major earthquakes (Itatani et al., 2024). This delay may stem from the Prefecture's unique geography, characterized by its narrow and elongated north-south topography and limited road connectivity. Figure 11 presents a detailed January–August 2024 timeline of utility restorations, housing interventions, and infrastructure repairs.

Although essential utilities such as electricity and water supply have been restored, and temporary houses have been made available for the displaced residents, additional temporary houses are still being constructed in Wajima and Suzu city.

Table 2 Comparative summary of the 2024 Noto, 2016 Kumamoto, and 2011 Tohoku earthquakes

Parameter	Noto Earthquake, 2024	Kumamoto Earthquake, 2016	Tohoku Earthquake, 2011
Magnitude (Mw)	7.6	7.0	9.0
Houses damaged	5,190 buildings collapsed; 16,231 partially damaged; 60,426 with varying damage levels (Disaster Prevention, Safety and Security, Ishikawa Prefecture 2024).	198,000 (completely destroyed: 8642, half: 34,389, partially: 155,227) (Takeda and Inaba 2022)	~128,530 completely or half destroyed; 240,332 partially destroyed or damaged (Kazama and Noda 2012)
Sediment disasters (slope failure and landslides)	>2,300 landslides (Gomez 2024)	3,467 landslides (Xu et al. 2017)	3,477 landslides (Wartman et al. 2013)
Ground uplift magnitude	~4 m vertical uplift (field verification)	~1.6 m horizontal uplift and ~2 m subsidence (Himematsu and Furuya 2020)	~5 m horizontal uplift and ~1 m vertical uplift (Kamiyama et al. 2017)
Liquefaction indicators	Lateral spreading, ground upheaval, ground settlement, sinking of utility poles, and the presence of sand ejecta	Sand and water boiling, tilting buildings, road undulation and collapse (Wakamatsu et al. 2017)	Sand boils, floating manholes, tilting and damaged housing, levees collapse, the collapse, subsidence, cracking, and irregularity of road (Kazama and Noda 2012)
Estimated cost of damage	¥1.1 trillion to ¥2.6 trillion (The Japan news 2024)	~¥3.8 trillion (Takeda and Inaba 2022)	~¥16.9 trillion (Kazama and Noda 2012)

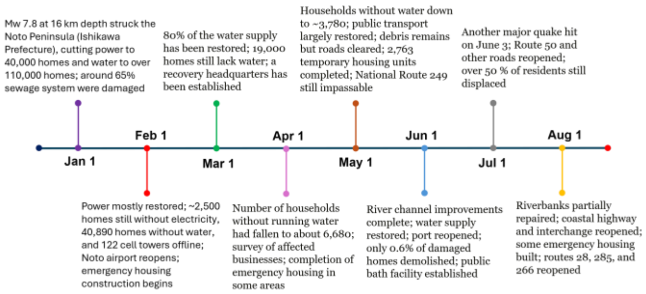

Figure 11, post-disaster recovery timeline (Jan–Aug 2024) in Ishikawa Prefecture after the 2024 Noto earthquake, showing utility restorations, housing, and infrastructure repairs.

Even though the road debris was removed for emergency movements, many collapsed structures remain untouched, and critical infrastructure repairs are yet to progress significantly. Among completely or partially damaged houses, yet many remain standing without being demolished, and as of May 26, only 2% have been demolished and removed (Ishikawa Noto Earthquake Interim Report 2024). Demolition requires specialized skills, but the number of qualified contractors is limited. The reason the demolition process is taking so long is the lack of a number of qualified contractors and adequate worker accommodation. The quake-hit area is still full of rubble, which might be due to delays in damage assessment surveys by the local government. Many tilted houses are still in danger of collapsing. The condition of the houses has been inspected, and inspection certificates are attached to the outer walls to inform residents of their condition (as depicted in Fig. 7).

The fishing port area, which has suffered severe damage and uplift, has rendered the area unstable, halting fishing activities vital to the local community. In many places, landslide-prone regions have been covered with water-resistant tarpaulin; however, long-term management strategies for these vulnerable areas remain lacking.

As recovery continues, the study area emphasizes "building back better". It can be clearly stated that Ishikawa Prefecture's approach introduces a more structured and efficient model for recovery in the affected region. Its clear transition from emergency to permanent housing, and higher levels of community engagement represent significant improvements, despite delays in damage repair (Yang et al 2024). The lessons learned from this earthquake highlighted the critical need for proactive disaster risk reduction measures, ensuring that future earthquakes will have less severe impacts on the people and infrastructure of the region. With scientists warning of the potential for a devastating Nankai Trough megathrust earthquake in southwestern Japan (Fukushima et al. 2023), there is an urgent need for concerned bodies and the local community to prioritize preparedness. Regions characterized by highly saturated, unconsolidated soils such as Kathmandu Valley, Nepal (Subedi and Acharya 2022), and parts of Chile (Verdugo and González 2015), face similar liquefaction hazards during seismic events and the threat of liquefaction demands that both authorities and communities prioritize preparedness now. From Ishikawa's example, three key strategies stand out for earthquake-prone areas: combining quick digital surveys, pre-positioned resources, and community-focused reconstruction. Together these strategies can cut recovery time, boost infrastructure resilience, and protect vulnerable populations. While every disaster has its own distinct characteristics and not every lesson will directly apply, consistently documenting these events builds a valuable knowledge base that enhances future prevention and mitigation efforts.

Conclusion

This study provides a comprehensive update on the current state of the Noto Peninsula and evaluates the damage and engineering geological challenges resulting from the earthquake. The severe tremors caused significant issues, including land uplift, structural collapses from soil liquefaction, tunnel failures, and landslides. The findings highlight that the mountainous terrain of the Noto Peninsula is particularly vulnerable to slope failures, emphasizing the need for thorough geological assessments and reinforcement in similar areas to reduce landslide risks. Liquefaction and land subsidence were the major engineering concerns, causing severe damage to human settlements and infrastructure, especially in rural areas. Notably, cut-and-fill slopes along mountainous roads were extensively damaged, indicating a need for seismic-resistant road design. Traditional wooden houses also sustained substantial damage, underscoring the importance of enhancing their seismic resistance and preparing for potential collapses in the affected area and across Japan. The affected area`s structured, community-focused model demonstrates a clear path toward more efficient, resilient recovery, despite lingering delays in repair work. Overall, Ishikawa Prefecture is focused on recovery and rebuilding from the 2024 Noto earthquake. For future resilience, it's crucial to address the engineering challenges revealed by the disaster and ensure that infrastructure and buildings are designed to withstand future seismic events since research has warned about the potential for a megathrust earthquake along the Nankai Trough.

Acknowledgement

We extend our deepest gratitude to the Japan Society for the Promotion of Science (JSPS) for awarding Dr. Ranjan Kumar Dahal the 2024 JSPS BRIDGE Fellowship, enabling this invaluable collaborative research program. We thank Prof. Dr. Shuichi Hasegawa of Kagawa University for his invaluable time, insights, and guidance during this field excursion. We also wish to express our sincere appreciation to the YON-C Consultants Co., Inc. staff in Takamatsu, Kagawa Prefecture, for their unwavering support and active participation in our field investigations. We are profoundly grateful to Prof. Dr. Tetsuya Kogure of Kyoto University for his valuable comments and constructive suggestions.

References

Dahal (2015). Engineering geological issues after Gorkha Earthquake 2015 in Nepal—a preliminary understanding. 10th Asian Regional Conference of IAEG, Kyoto, Japan.

DesRoches R., Comerio M., Eberhard M., Mooney W. and Rix G.J. (2011). Overview of the 2010 Haiti earthquake. Earthquake Spectra 27, 1–21. https://doi.org/10.1193/1.3630129

Disaster Prevention, Safety and Security, Ishikawa Prefecture (2024). Information on the Noto Peninsula Earthquake in 2024 by purpose. https://www.pref.ishikawa.lg.jp/saigai/202401jishin-taisakuhonbu.html#higai (in Japanese). Accessed on 6 Sept 2024.

Fukushima Y., Ishimura D., Takahashi N., Iwasa Y., Malatesta L.C., Takahashi T., Tang C.H., Yoshida K. and Toda S. (2024). Landscape changes caused by the 2024 Noto Peninsula earthquake in Japan. Science Advances 10, eadp9193. https://doi.org/10.1126/sciadv.adp9193

Fukushima Y., Nishikawa T. and Kano Y. (2023). High probability of successive occurrence of Nankai megathrust earthquakes. Scientific Reports 13, 63. https://doi.org/10.1038/s41598-022-26455-w

Geospatial Information Authority of Japan. (2024). Coastline change caused by the 2024 Noto Peninsula Earthquake detected by ALOS-2 SAR satellite image (Jan. 4, 2024). Retrieved from https://www.gsi.go.jp/uchusokuchi/uchusokuchi-e31001.html. Accessed on 8 Sept 2024.

Gomez C. (2024). The January 1st 2024 Noto Peninsula co-seismic landslides hazards: preliminary results. 31 January 2024, PREPRINT (Version 1) available at Research Square https://doi.org/10.21203/rs.3.rs-3904468/v1

Himematsu Y., Furuya M. (2020). Coseismic and postseismic crustal deformation associated with the 2016 Kumamoto earthquake sequence revealed by PALSAR-2 Pixel tracking and InSAR. Earth and Space Science 7, e2020EA001200. https://doi.org/10.1029/2020EA001200

Honda R., Hiramatsu Y., Kono Y. and Katagawa H. (2008). Gravity anomalies and the geologic block structures in and around the aftershock area of the 2007 Noto Hanto Earthquake. Earth, Planets and Space 60, 111–115. https://doi.org/10.1186/BF03352770

Ishikawa Noto Earthquake Interim Report (2024). Retrieved from https://pbv.or.jp/wp_en/wp-content/uploads/2024/06/ENG_2024_Noto-Report.pdf. Accessed on 15 Sept 2024.

Ishikawa Y. and Bai L. (2024). The 2024 Mj 7.6 Noto Peninsula, Japan earthquake caused by the fluid flow in the crust. Earthquake Research Advances 4, 100292. https://doi.org/10.1016/j.eqrea.2024.100292

Itatani T., Kojima M., Tanaka J., Horiike R., Sibata K. and Sasaki R. (2024). Operational management and improvement strategies of evacuation centers during the 2024 Noto Peninsula earthquake—a case study of Wajima city. Safety 10, 62. https://doi.org/10.3390/safety10030062

Kamiyama M., Koide H., Sawada Y., Akita H. and Chiba N. (2017). Monitoring of crustal deformation and its application to mitigation of earthquake disasters. Journal of JSCE 5, 206–225. https://doi.org/10.2208/journalofjsce.5.1_206

Kataoka K., Urabe A., Nishii R., Matsumoto T., Niiya H., Watanabe N., Kawashima K., Watabe S., Takashimizu Y., Fujibayashi N. and Miyabuchi Y. (2024). Extensive liquefaction and building damage on the Niigata Plain due to the 1 January 2024 Noto Peninsula Earthquake: Geomorphological and geological aspects and land-use in coastal and lowland areas, EGU General Assembly 2024, Vienna, Austria, 14–19 Apr 2024, EGU24-22541, https://doi.org/10.5194/egusphere-egu24-22541.

Kato A. (2024). Implications of fault-valve behavior from immediate aftershocks following the 2023 M6.5 earthquake beneath the Noto Peninsula, Central Japan. Geophysical Research Letters 51, e2023GL106444. https://doi.org/10.1029/2023GL106444

Kazama M. and Noda T. (2012). Damage statistics (summary of the 2011 off the Pacific Coast of Tohoku Earthquake damage). Soils and Foundations, Special issue on geotechnical aspects of the 2011 off the Pacific Coast of Tohoku Earthquake 52(5), 780–792. https://doi.org/10.1016/j.sandf.2012.11.003

Kuribayashi K., Hara T., Sakabe A. and Kuroda S. (2021). A study on road embankment damage on liquefied ground. Journal of the Japan Association for Earthquake Engineering 21(1):46-1_63. (In Japanese). https://doi.org/10.5610/jaee.21.1_46

Liu C., Fang D. and Zhao L. (2021). Reflection on earthquake damage of buildings in 2015 Nepal earthquake and seismic measures for post-earthquake reconstruction. Structures 30, 647–658. https://doi.org/10.1016/j.istruc.2020.12.089

Loi D.H., Jayakody S., Sassa K., Konagai K., Hirota K., Ono A., Takanaka T., Oki T. and Minamitani T. (2024). Landslides triggered by the 2024 Noto Peninsula earthquake. Landslides 21:2583–2590 https://doi.org/10.1007/s10346-024-02333-6

Mizuno C., Wang X. and Dang J. (2024). A fast survey report about bridge damages by the 2024 Noto Peninsula Earthquake. Earthquake Research Advances 5(4):100312. https://doi.org/10.1016/j.eqrea.2024.100312

Nishimura T., Hiramatsu Y. and Ohta, Y. (2023). Episodic transient deformation revealed by the analysis of multiple GNSS networks in the Noto Peninsula, central Japan. Scientific Reports 13, 8381. https://doi.org/10.1038/s41598-023-35459-z

Ohno H., Tsutsumi D., Furuya G., Takiguchi S., Ikeda M., Miyagi A., Miike T. and Sawa Y. (2024). Sediment-related disasters induced by the Noto Peninsula Earthquake in January 2024. International Journal of Erosion Control Engineering 17(4):42–50. https://doi.org/10.13101/ijece.17.42

Pai L. and Wu H. (2021). Multi-attribute seismic data spectrum analysis of tunnel orthogonal underpass landslide shaking table test. Soil Dynamics and Earthquake Engineering 150, 106889. https://doi.org/10.1016/j.soildyn.2021.106889

Peng X., Wang F., Miyajima M., Yoshida M., Zhang S. and Fu Z. (2025). Brief report of a field investigation in Noto Peninsula, Japan, after the 2024 Noto earthquake. Geoenvironmental Disasters 12, 11. https://doi.org/10.1186/s40677-025-00315-x

Seno T., Stein S. and Gripp A.E. (1993). A model for the motion of the Philippine Sea Plate consistent with NUVEL-1 and geological data. Journal of Geophysical Research: Solid Earth 98, 17941–17948. https://doi.org/10.1029/93JB00782

Setiawan H., Serikawa Y., Nakamura M., Miyajima M. and Yoshida M. (2017). Structural damage to houses and buildings induced by liquefaction in the 2016 Kumamoto Earthquake, Japan. Geoenvironmental Disasters 4, 13. https://doi.org/10.1186/s40677-017-0077-x

Shishikura M., Echigo T. and Namegaya Y. (2009). Evidence for coseismic and aseismic uplift in the last 1000 years in the focal area of a shallow thrust earthquake on the Noto Peninsula, west-central Japan. Geophysical Research Letters 36. https://doi.org/10.1029/2008GL036252

Subedi M. and Acharya I.P. (2022). Liquefaction hazard assessment and ground failure probability analysis in the Kathmandu Valley of Nepal. Geoenvironmental Disasters 9, 1. https://doi.org/10.1186/s40677-021-00203-0

Suppasri A., Kitamura M., Alexander D., Seto S. and Imamura F. (2024). The 2024 Noto Peninsula earthquake: preliminary observations and lessons to be learned. International Journal of Disaster Risk Reduction 110, 104611. https://doi.org/10.1016/j.ijdrr.2024.104611

Takeda K. and Inaba K. (2022). The damage and reconstruction of the Kumamoto earthquake: an analysis on the impact of changes in expenditures with multi-regional input–output table for Kumamoto Prefecture. Journal of Economic Structures 11, 20. https://doi.org/10.1186/s40008-022-00276-6

The Japan News (2024). Earthquake damage in Ishikawa, Toyama, Niigata Prefectures estimated to cost up to ¥2.6 Trillion. https://japannews.yomiuri.co.jp/society/noto-peninsula-earthquake/20240126-164732/. Accessed on 13 Sept 2024.

Toda S. and Stein R.S. (2024). Intense seismic swarm punctuated by a magnitude 7.5 Japan shock. Temblor.net. https://temblor.net/temblor/intense-seismic-swarm magnitude-7-5-japan-earthquake-15891/. Accessed on 26 Aug 2024.

Uchida N. and Bürgmann R. (2021). A decade of lessons learned from the 2011 Tohoku-Oki earthquake. Reviews of Geophysics 59(2):e2020RG000713. https://doi.org/10.1029/2020RG000713

Umeda K., Yamazaki Y. and Sumino H. (2024). Geochemical signature of deep fluids triggering earthquake swarm in the Noto Peninsula, Central Japan. Geophysical Research Letters 51, e2024GL108581. https://doi.org/10.1029/2024GL108581

USGS (2024). M 7.5 - 2024 Noto Peninsula, Japan Earthquake.https://earthquake.usgs.gov/earthquakes/eventpage/us6000m0xl/executive. Accessed on 16 Sept 2024.

Verdugo R. and González J. (2015). Liquefaction-induced ground damages during the 2010 Chile earthquake. Soil Dynamics and Earthquake Engineering 79, 280–295. https://doi.org/10.1016/j.soildyn.2015.04.016

Wakamatsu K., Senna S. and Ozawa K. (2017). Liquefaction during the Kumamoto Earthquakes on April 14 and 16, 2016. Lowland Technology International Journal 19(3):191–202. Retrieved from https://cot.unhas.ac.id/journals/index.php/ialt_lti/article/view/517/408. Accessed on 25 Aug 2024.

Wang Q.Y., Cui X., Frank W.B., Lu Y., Hirose T. and Obara K. (2024). Untangling the environmental and tectonic drivers of the Noto earthquake swarm in Japan. Science Advances 10(19):eado1469. https://doi.org/10.1126/sciadv.ado1469

Wartman J., Dunham L., Tiwari B. and Pradel D. (2013). Landslides in Eastern Honshu Induced by the 2011 Tohoku Earthquake. Bulletin of the Seismological Society of America 103 (2B):1503–1521. https://doi.org/10.1785/0120120128

Xu C., Ma S., Tan Z., Xie C., Toda S. and Huang X. (2017). Landslides triggered by the 2016 Mj 7.3 Kumamoto, Japan, earthquake. Landslides 15, 551–564. https://doi.org/ 10.1007/s10346-017-0929-1

Yamazaki F. and Murao O. (2000). Vulnerability functions for Japanese buildings based on damage data from the 1995 Kobe earthquake, in: Implications of Recent Earthquakes on Seismic Risk, Series on Innovation in Structures and Construction. Published by Imperial College press and distributed by world scientific publishing co., pp. 91–102. https://doi.org/10.1142/9781848160194_0007

Yang D., Minami M., Fahim A. U. and Kawashita T. (2024). A timeline-based study of the early reconstruction phases in Ishikawa Prefecture following the 2024 Noto Peninsula earthquake. Sustainability, 16(24):10838. https://doi.org/ 10.3390/su162410838

Asian Journal of Engineering Geology, 2024, Vol. 1 No. 1 and 2, 17-26

Research Article **DOI: https://doi.org/10.64862/ajeg.112.03** **Open Access**

Red Relief Image Maps to Visualize Landslide Risks in Master-Planned Storage-Type Hydropower Projects in Nepal Using a Free and Open-Source GIS Approach

Milan Kumar Rai[1]* and Anjila Babu Malla[2, 3]

[1]GEOCE Consultants Pvt. Ltd., Jhamsikhel, Lalitpur, Nepal
[2]Geotech Solutions International, Dhobighat, Lalitpur, Nepal
[3]Department of Earth Science, Shimane University, Matsue, Japan

*(*Corresponding E-mail: egeologistmilan@gmail.com)*

Received: August 09, 2024, Accepted on November 13, 2024

Abstract: The development of storage-type hydropower projects is crucial for enhancing energy security and managing water resources in Nepal. However, these projects often face significant challenges related to terrain stability, particularly in landslide-prone regions of the Nepal Himalayas. This study presents an innovative approach to terrain visualization using Red Relief Image Maps (RRIM) generated through free and open-source GIS tools. This article presents RRIM visualization techniques developed entirely with free and open-source GIS tools, such as QGIS and Topographic Openness. The selection criteria for these techniques prioritize simplicity and speed of implementation while ensuring their suitability for effective visualization. The study focuses on the application of these techniques to Nationwide Master Planned Storage-type Hydropower Projects in Nepal. By generating and analyzing several RRIM, the article demonstrates how these tools can aid in visualizing terrain features and identifying potential risks associated with deep-seated landslides distribution. The RRIM has been prepared for all 20-master planned storage-type hydropower, diversion and multipurpose projects of Nepal. Additionally, the integration of 3D map visualization of the RRIM enhances the understanding of the terrain's topography and landform. The findings highlight the effectiveness of RRIM and open-source GIS tools in enhancing geohazard assessment and planning for sustainable infrastructure development in future.

Keywords: ***ALOS PALSAR, Deep-seated Landslides, Landslide Risks, Open-Source GIS Tools, QGIS, Red Relief Map, RRIM, Remote Sensing, Storage-type Hydropower, Topographic Openness, 3D Terrain Visualization***

Introduction

Government of Nepal intends to develop the hydropower potential of Nepal in an economically efficient and sustainable manner to meet the growing power demand in the country. In the line with the hydropower development policy Government of Nepal intends to carryout Feasibility Studies and Environmental studies of hydropower projects under Hydropower Project Study Program utilizing Nepal Government's resources. In this regards, Government of Nepal (GoN), Department of Electricity Development (DoED) conducting the Feasibility and Environmental Impact Assessment (EIA) Study of different storage-type hydropower projects. These projects are listed in the Nationwide Master Plan Study on Storage-Type Hydropower Projects conducted by the Nepal Electricity Authority in 2014. This master plan provides a strategic framework for developing storage-type hydropower projects across Nepal.

Landslides, particularly in deep-seated landslide areas, frequently damage infrastructure, leading to major economic losses and public suffering every year in Nepal (Bhandary et al. 2011). In the Himalayan region, where many of these projects are planned, it presents unique challenges due to its complex terrain and susceptibility to natural hazards such as landslides. Traditional methods of terrain analysis may not fully address these challenges, necessitating advanced visualization techniques to improve understanding and risk assessment. Large-scale landslide inventory mapping in the Lesser Himalaya has demonstrated that the spatial distribution of landslides is strongly influenced by terrain morphology, geological structures, and slope conditions, underscoring the effectiveness of GIS-based methodologies for comprehensive hazard assessment (Timilsina et al. 2017).

This article introduces an innovative approach to terrain visualization using Red Relief Image Maps (RRIM), generated with free and open-source GIS tools such as QGIS and Topographic Openness. These tools are chosen for their simplicity, speed of implementation, and effectiveness in providing detailed visualizations. By applying these techniques to master-planned storage-type hydropower projects in Nepal, this study demonstrates how RRIM can enhance the 3D visualization of terrain features and identify potential risks, especially related to deep-seated landslides distribution in the reservoir area.

Most of the small-scale landslides are found to occur on the large-scale landslide or deep-seated landslide topography (Dahal, 2015). Identifying such risks is crucial for ensuring the stability of the reservoir and surrounding infrastructure. Deep-seated landslides can trigger waves or reservoir tsunamis, leading to damage or even failure of dam structures. They can also contribute to excessive sedimentation, reducing water storage capacity and increasing maintenance costs. Additionally, landslides may affect access roads, tunnels, and other key infrastructure, posing risks to long-term operations. These hazards can also lead to the displacement of communities and have significant ecological impacts. Early identification of these risks allows for proactive mitigation strategies, ensuring cost-effective and safe project execution.

This study focuses on 20-master plan storage-type hydropower, diversion and multipurpose projects across Nepal, analyzing their terrain characteristics and associated risks. The findings of this study aim to support the GoN's efforts in developing sustainable infrastructure in the challenging mountainous terrain, improving the planning and risk management of future storage- type hydropower projects.

The Government of Nepal has prioritized the sustainable and economically viable development of its hydropower potential to meet the country's increasing energy demands. In alignment with national hydropower development policies, the Department of Electricity Development (DoED) is conducting feasibility studies and Environmental Impact Assessments (EIA) for various storage-type hydropower projects identified in the Nationwide Master Plan Study on Storage-Type Hydroelectric Projects prepared by the Nepal Electricity Authority (NEA and JICA, 2014). These projects are predominantly located in the Himalayan region, characterized by complex terrain and a high susceptibility to geohazards, particularly landslides.

Landslides, especially deep-seated ones, have caused significant damage to infrastructure in Nepal, resulting in economic losses and public safety concerns (Bhandary et al. 2011 and Dahal 2015). Moreover, small-scale landslides often occur within broader zones of deep-seated instability (Dahal, 2015), increasing the risk to hydropower infrastructure. This study introduces an advanced terrain visualization method using Red Relief Image Maps (RRIM), generated through open-source GIS platforms such as QGIS and Topographic Openness. Applied to 20 master plan storage-type and multipurpose hydropower projects, this approach enhances the identification of potential landslide-prone zones. The findings aim to improve planning and hazard mitigation strategies, thereby supporting the safe and sustainable development of hydropower infrastructure in Nepal's mountainous regions.

Study area

The study area includes 20 storage-type hydropower, diversion and multipurpose projects as shown in Table 1, identified in the Nationwide Master Plan Nationwide Master Plan Study on Storage-Type Hydropower Projects conducted by the Nepal Electricity Authority (NEA) and some of them being under Feasibility Study & Environmental Impact Assessment (EIA) Study are conducting by the Department of Electricity Development (DoED), Department of Water Resources & Irrigation (DWRI). Figure 1 shows the geographic distribution of these projects across Nepal.

Table 1, List of Master planned Storage-type Hydropower, Diversion and Multipurpose Projects of Nepal

S.N.	Project Name	Geographic Location	Geo-tectonic Location	Administrative location		FSL (masl)	Reservoir area (km^2)
				Province	District		
1	Budhigandaki Hydropower Project	Central Nepal	Lesser Himalaya	Gandaki and Bagmati	Gorkha and Dhading	540	63
2	Bharbung Storage Hydropower Project	Western Nepal	Higher Himalaya	Karnali	Dolpa	3350	8.20
3	Dudh Koshi Storage Hydropower Project	Eastern Nepal	Lesser Himalaya	Koshi	Khotang, Okhaldhunga and Solukhumbu	640	20.01
4	Kaligandaki Storage Hydropower Project	Western Nepal	Lesser Himalaya	Gandaki and Lumbini	Parbat, Baglung and Gulmi	750	21.06
5	Kaligandaki-2 Storage Hydropower Project	Western Nepal	Lesser Himalaya	Gandaki and Lumbini	Syanja, Palpa, Nawalparasi (East) and Tanahu	370	92.12
6	Kankai Multipurpose Project	Eastern Nepal	Siwaliks	Koshi	Ilam and Jhapa	200	48.88
7	Khimti Those Siwalaya Storage Hydropower Project	Eastern Nepal	Lesser Himalaya	Bagmati	Dolakha and Ramechhap	1885	9.00
8	Kokhajor Storage Hydropower Project	Central Nepal	Siwaliks	Bagmati	Sindhuli and Kabhrepalanchok	460	6.17
9	Kulekhani Hydropower Project	Central Nepal	Lesser Himalaya	Bagmati	Makawanpur	1530	2.2
10	Lower Badigad Storage Hydropower Project	Western Nepal	Lesser Himalaya	Lumbini	Gulmi	700	17.53
11	Madi Siti Storage Hydropower Project	Western Nepal	Lesser Himalaya	Gandaki	Kaski and Lamjung	640	8.74
12	Manahari Multipurpose Project	Western Nepal	Lesser Himalaya	Bagmati	Makawanpur	540	5.95
13	Mugu Karnali Hydropower Project	Far Western Nepal	Lesser Himalaya	Karnali and Sudurpaschim	Bajura, Mugu and Humla	1350	40.66
14	Nalgad Storage Hydropower Project	Western Nepal	Lesser Himalaya	Karnali	Jajarkot	1580	7.66
15	Naumure Storage Hydropower Project	Western Nepal	Siwaliks	Lumbini	Argakhanchi and Pyuthan	524	19.73
16	SR-6 Storage Hydropower Project	Far Western Nepal	Lesser Himalaya	Sudurpaschim	Doti and Achham	603	50.80
17	Sun Koshi 3 Storage Hydropower Project	Eastern Nepal	Lesser Himalaya	Bagmati	Kabhrepalanchok, Sindhupalchok and Ramechhap	700	53.38
18	Sunkoshi Marin Diversion Multipurpose Project	Central Nepal	Lesser Himalaya	Bagmati	Sindhuli and Ramechhap	476	3.44
19	Tamor Storage Hydropower Project	Eastern Nepal	Lesser Himalaya	Koshi	Panchthar, Terhathum and Taplejung	550	39.02
20	Tanahu Hydropower Project (Upper Seti)	Western Nepal	Lesser Himalaya	Gandaki	Tanahu	417	8.27

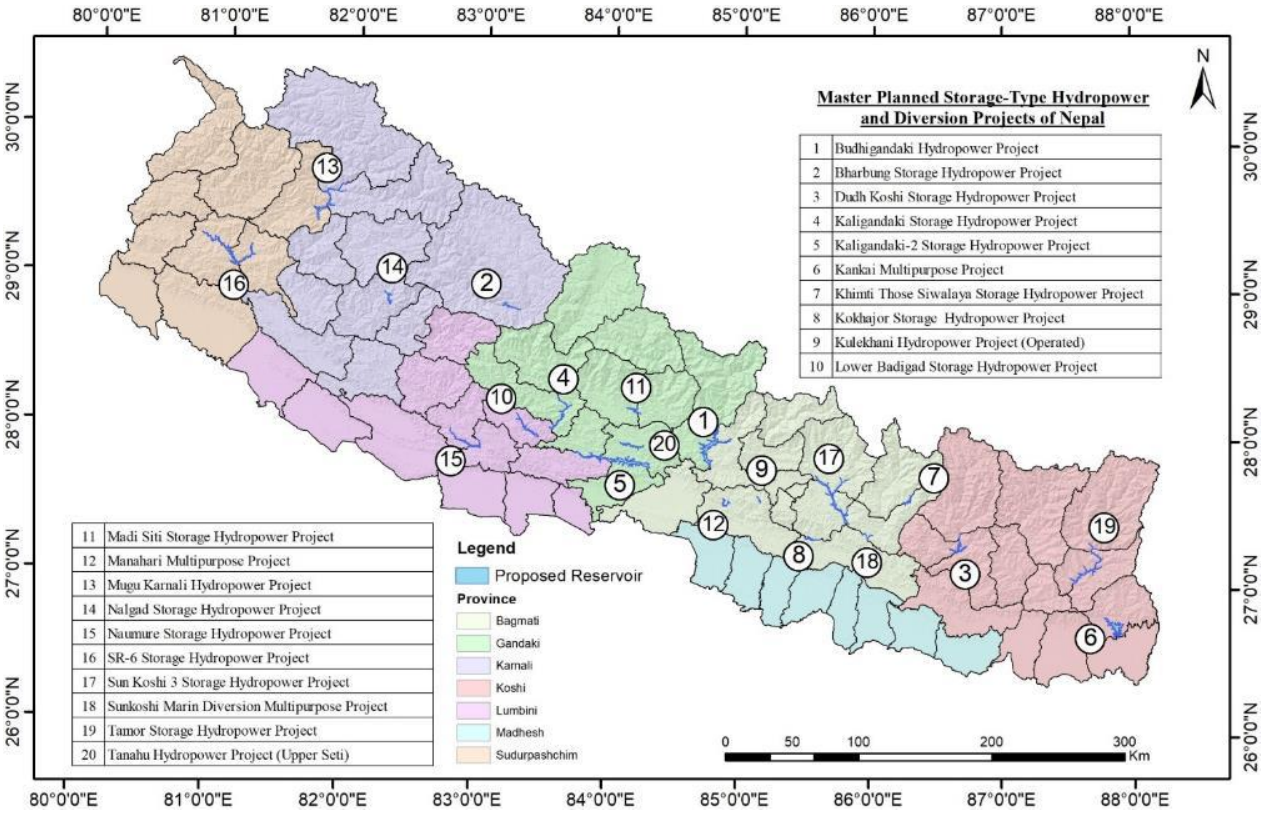

Figure 1, Location map of the 20-master planned storage-type projects of Nepal.

Methodology

The main concept of RRIM from DEMs is based on Topographic Slope and Topographic Openness i.e., Positive Openness (Op), Negative Openness (On). Positive and negative openness were defined by Yokoyama et al. (2002). Positive openness represents convexity of the surface and Negative openness represents surface concavity of the surface. Positive openness represents higher values such as ridges, peaks and crests while negative openness takes higher value such as valley, gully, pit, landslides and inside of craters. Figure 2 is a conceptual diagram of positive and negative openness. The Op and On are shown schematically for values less than 90 degrees. L is radial limit of calculation for chosen points (P1 and P2) on a DEM. Chiba et al. (2008) calculated a new parameter called differential openness from Op and On like below,

Differential Openness = (Positive Openness - Negative Openness)/2

$$\text{i.e., } I = \frac{(Op\text{-}On)}{2} \qquad - (1)$$

Where, Op is positive openness and On is negative openness. The Op and On are shown schematically for values less than 90 degrees. I is a ridge and valley index. In RRIM, index is expressed by gray-scale image layer and topographic slope is red color layer.

According to Chiba et al. (2008), that red color has the richest tone for human eyes, especially under computer-oriented color spaces. RRIM effectively represents large-scale land features as well as fine structure at the same time in a wide variety of topographic situations. This dual representation is invaluable for understanding terrain characteristics and identifying potential instability risks. Figure 3 is a sample color diagram of RRIM method. Topographic slope is shown as Chroma value of red (y axis) and (Op-On)/2 is shown as brightness (x axis). As a result, the top of ridges is shown as white, bottom of valleys is shown as black, steep slopes are shown as bright red and flat surfaces are shown as gray in RRIM.

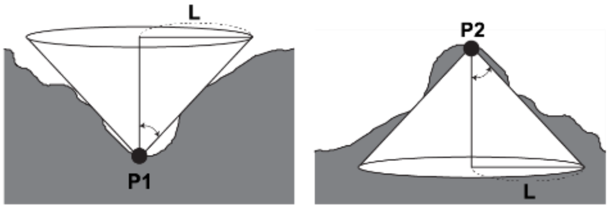

Figure 2, Conceptual diagram of positive openness and negative openness.

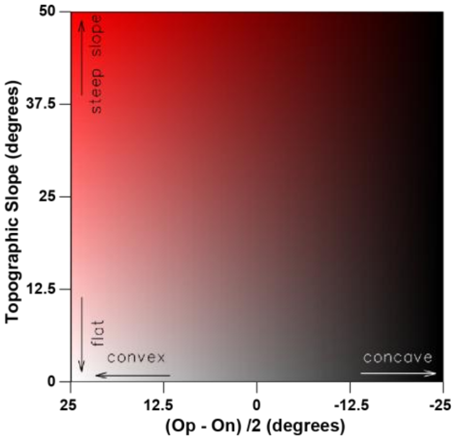

Figure 3, Color diagram of RRIM (example).

Preparation RRIM by using Digital Elevation Model (DEM)

All the raster maps are readily determined in the QGIS tool based on the DEM retrieved and analyzed by using the model as shown in Figure 4 for RRIM.

Data Acquisition and Processing in QGIS

The primary data source in this study is the ALOS PALSAR Digital Elevation Model (DEM) with a resolution of 12.5 x 12.5 meters and obtained from Alaska (2024).

The open-source software QGIS can be downloaded from its home page (https://www.qgis.org/). This powerful Geographic Information System (GIS) tool allows users to visualize, analyze, and manage spatial data effectively. Additionally, we provide a step-by-step tutorial for the preparation of a Red Relief Image Map (RRIM) in Appendix-I. This supplementary guide covers each step of the procedure, from data import to visualization, enabling you to create effective terrain analyses.

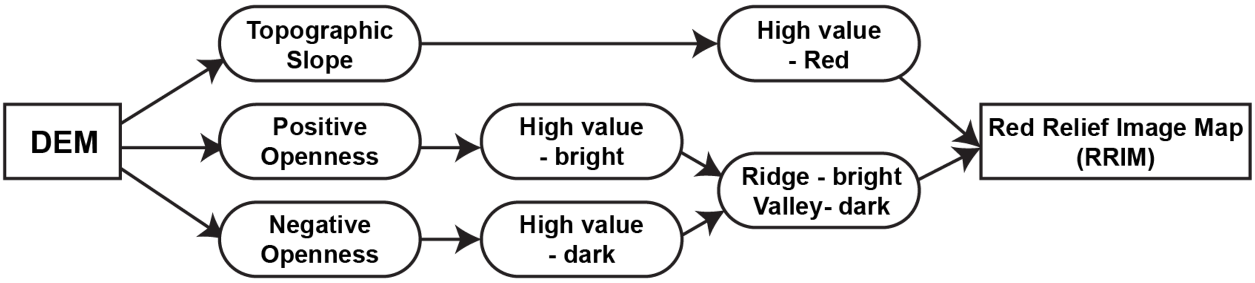

Figure 4, Model of preparation the Red Relief Image Map by using DEM.

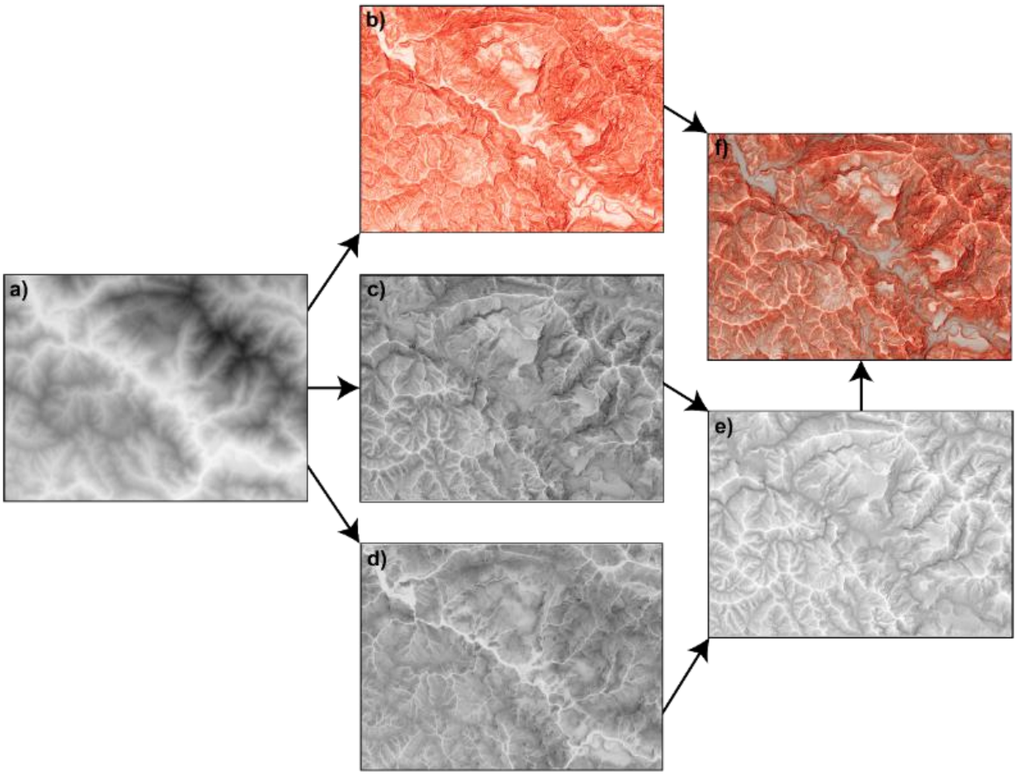

Figure 5, Flow of preparation RRIM. a) DEM, b) Slope, c) Positive Openness, d) Negative Openness, e) Differential Openness, and e) Final Red Relief Image Map.

Results and Discussion

The RRIM has been prepared for all 20-master plan storage-type hydropower, diversion and multipurpose projects of Nepal as shown in Figure 6. The resulting RRIM successfully enhanced the identification of deep-seated landslides distribution at the study area and proved to be an effective tool for illustrating the complexity of the terrain and highlighting areas susceptible to deep-seated landslides. The distinct red color of the slope layer, combined with the grayscale representation of openness, facilitates a clear visualization of critical terrain features. In contrast, the normal hill shade technique, while beneficial for providing an overview of the topography, falls short in emphasizing the underlying landslide hazards. This technique tends to obscure important details related to the concavity and convexity of the terrain, which are crucial for assessing landslide hazard risks.

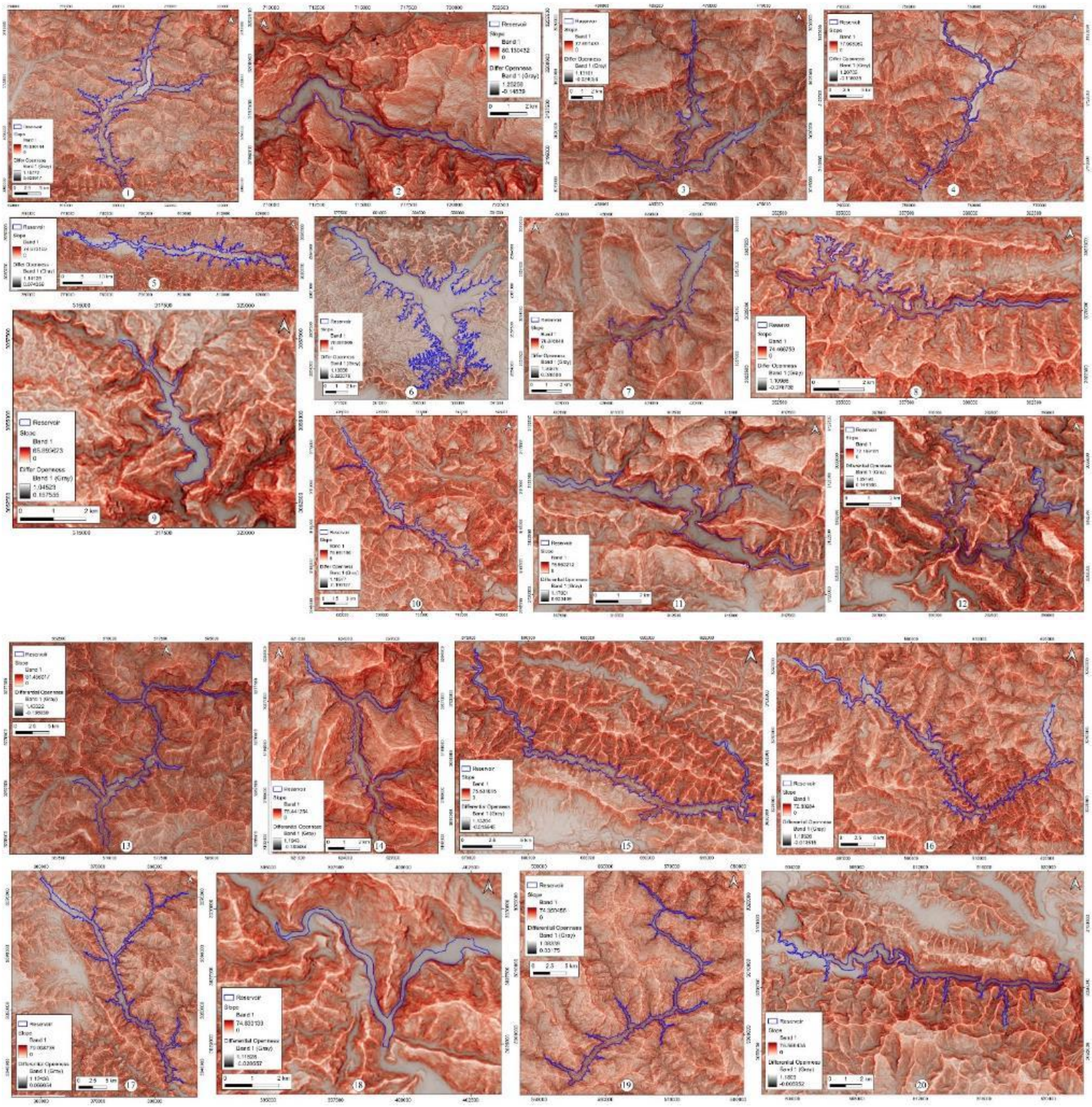

Figure 6, RRIM map of all 20-master plan storage-type projects.

Case study: Lower Badigad Storage Hydropower Project

This case study focuses on the geomorphic features and terrain analysis conducted for the Lower Badigad Storage Hydropower Project, located in a highly landslide-prone area, which presents significant relevance for this study, specifically emphasizing the identification and visualization of deep-seated landslides using both the RRIM and normal hill shade techniques. Various geological and geomorphological evidence has been found to trace the Badi Gad Fault in the region (Timalsina and Paudyal 2018). However, there have been very few studies on the fault's existence and its extent. Figure 7, RRIM map showing marked both old and recent landslides in the Lower Badigad Storage Hydropower Project area.

Comparison of Visualization Techniques

The primary objective of this study was to visualize terrain morphology in a way that traditional hill shade or satellite imagery may not reveal. Figure 8 presents a comparative analysis and field verification of a landslide event within the study area. Figure 8a displays the landslide as captured by Sentinel-2 (Copernicus, 2024) imagery using a false-color combination, which enhances vegetation and soil contrast, making the landslide scar more distinguishable from the surrounding terrain. The landslide-affected area appears as a distinct light-toned zone, indicating the exposed soil and debris. Figure 8b provides a field photograph taken during the site visit, confirming the presence and characteristics of the landslide observed in the satellite imagery. Visible features such as slope failure, exposed bedrock, and displaced materials validate the remote sensing interpretation. Figure 8c includes the Google Earth image of the same location, offering a visual context with high-resolution optical imagery for cross-verification of landslide extent and surrounding features. This multi-source comparison enhances the reliability of landslide identification and supports the integration of remote sensing and field-based approaches in RRIM mapping and validation. Figure 9a illustrates the RRIM, with landslides clearly marked, highlighting the spatial distribution of these hazards in relation to the proposed dam site and the reservoir area. The enhanced visibility of risk zones in the RRIM allows for more informed decision-making during the planning and risk management phases of project development. Conversely, Figure 9b presents the normal hill shade for comparative analysis. While it provides a general overview of the landform, it lacks the detailed depiction of deep-seated landslide distribution, which is also not apparent in the Google Earth imagery shown in Figure 10b.

Additionally, the integration of 3D map visualization of the RRIM enhances the understanding of the terrain's topography and the spatial relationships between various landform features. The 3D representation provides an immersive perspective, allowing stakeholders to visualize the landscape more intuitively. Figure 11 demonstrates the 3D RRIM visualization, which can significantly aid in identifying critical areas for potential landslide occurrences and assessing their impacts on storage type hydropower project planning.

Importantly, while Yokoyama et al. (2002) and Chiba et al. (2008) have previously developed RRIM techniques in Japan, the present study represents the first application of these methodologies in the mountainous terrain of Nepal. The resulting maps not only provide effective visualization of terrain features and geomorphological aspects but also contribute to a deeper understanding of landslide dynamics in this challenging region. This study is grounded in a completely free and open-source GIS approach, promoting accessibility and sustainability in geospatial analysis.

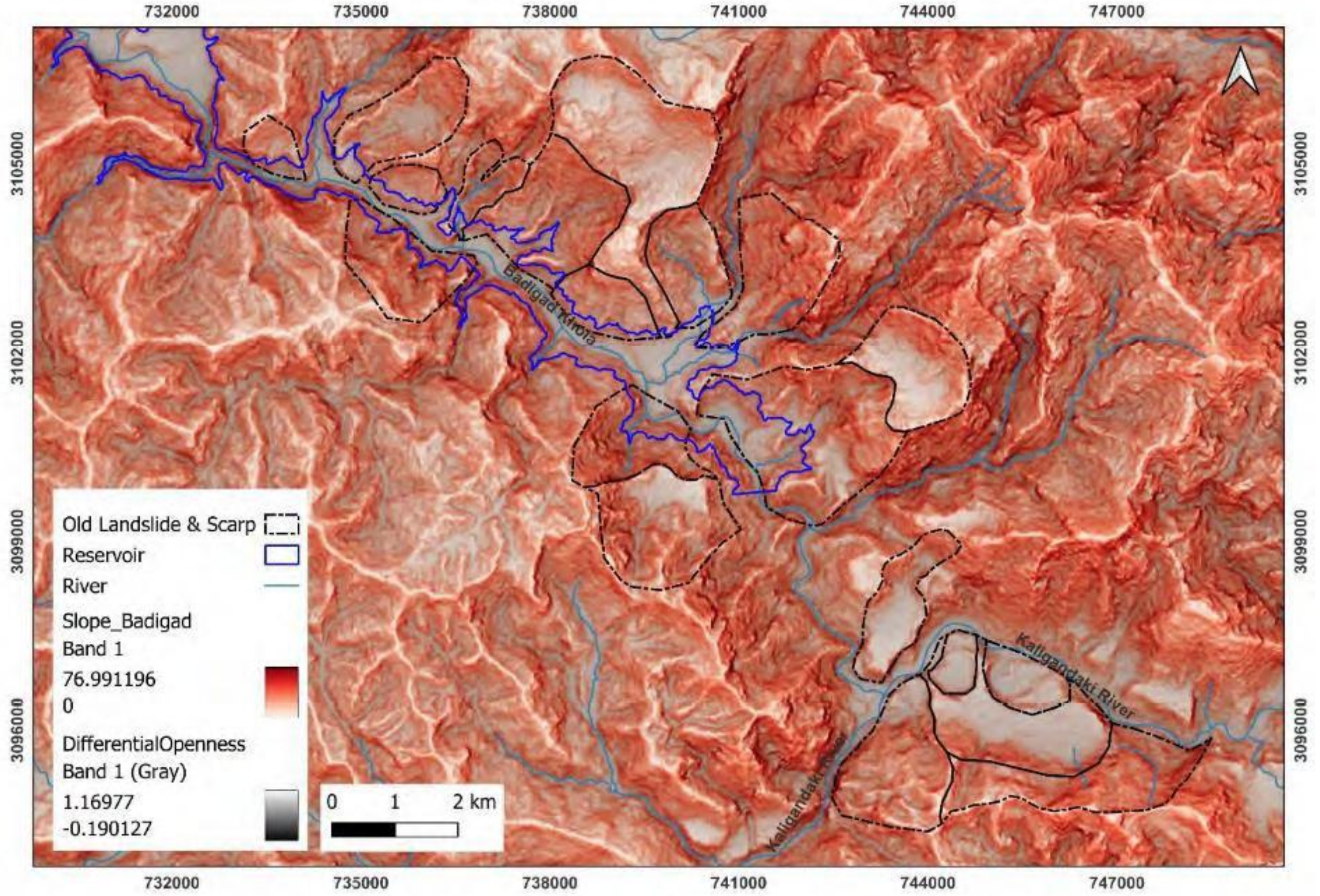

Figure 7, RRIM map showing marked deep-seated landslides within the Lower Badigad Storage Hydropower project area.

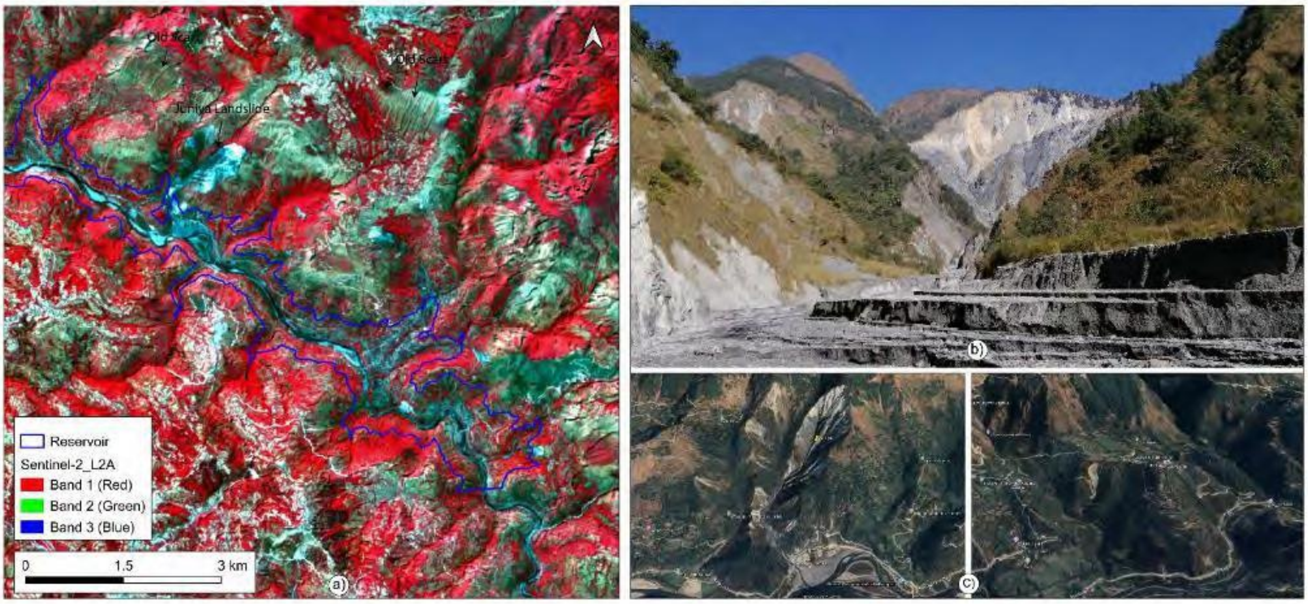

Figure 8, Comparisons and field verifications: a) Landslide as captured by Sentinel-2 imagery in false color combination, b) corresponding field photograph, and c) imagery from Google Earth.

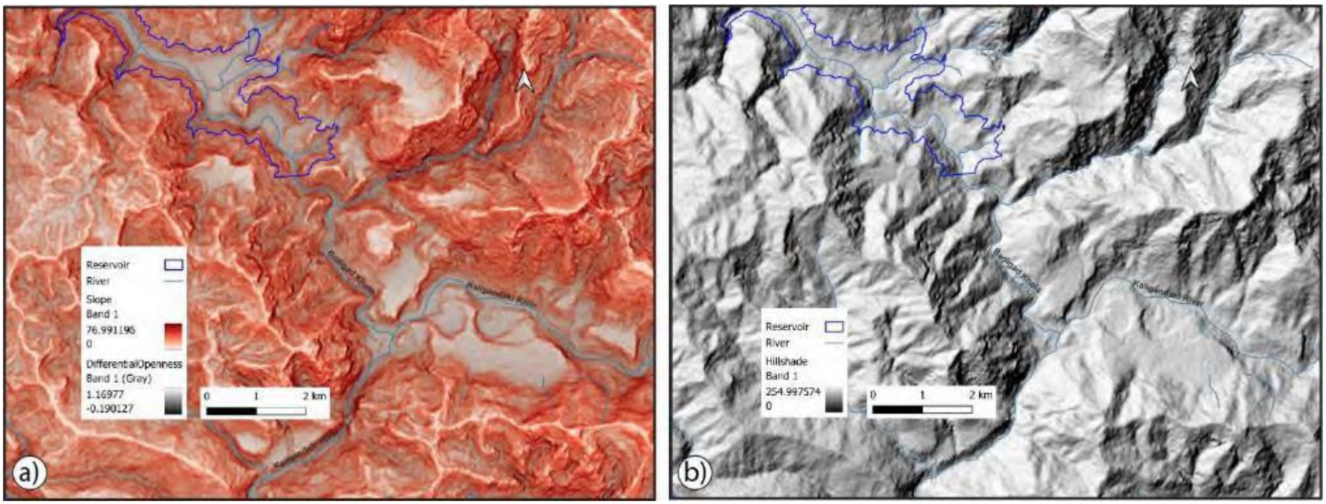

Figure 9, Comparisons between RRIM and normal Hill shade, a) RRIM and b) Hill shade.

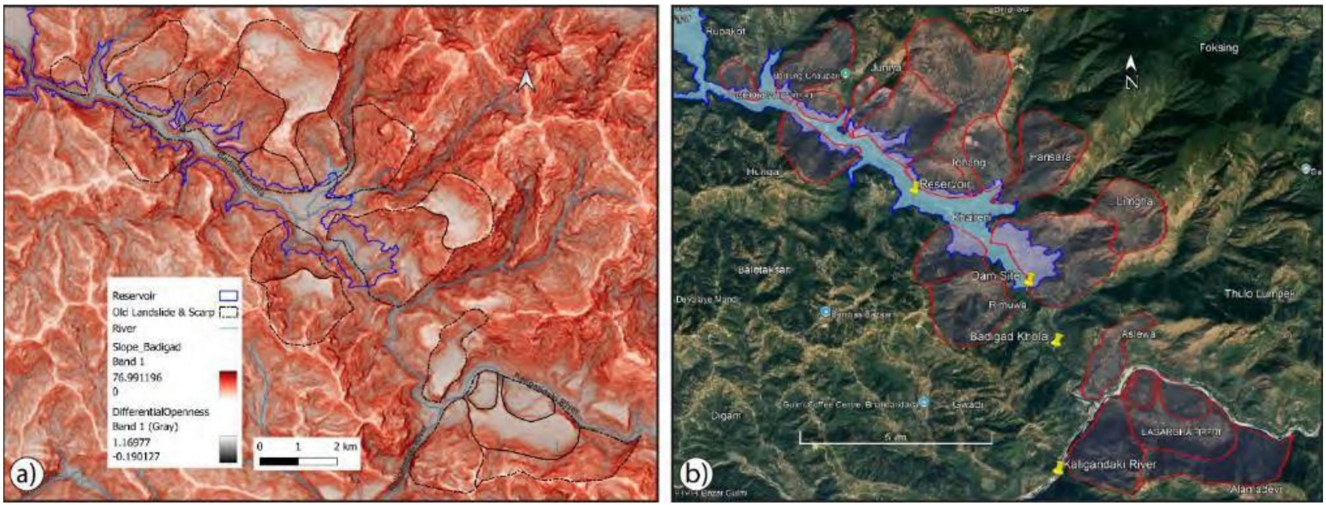

Figure 10, Comparisons between RRIM and Google Earth imagery, a) RRIM, and b) Google Map.

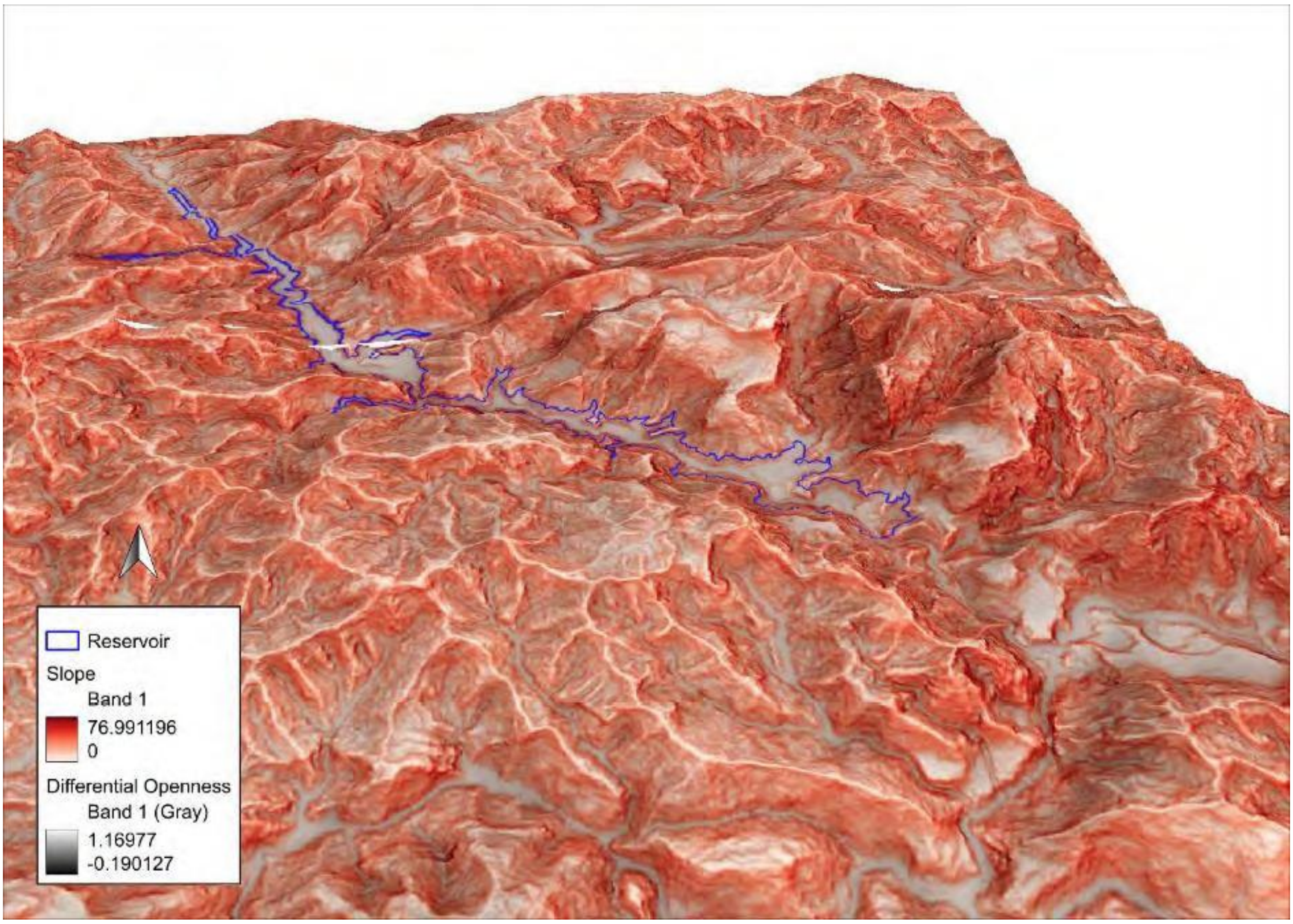

Figure 11, 3D Red Relief Image Map (3D RRIM) Visualization.

Implications for Risk Assessment in storage type Hydropower Projects

The findings from this analysis underscore the importance of utilizing advanced visualization techniques, such as 3D RRIM, in the planning and development of storage type hydropower projects situated in landslide-prone areas. By providing clearer insight into potential landslide risks, these tools can assist stakeholders in making more informed decisions concerning site selection, design modifications, and mitigation strategies. Integrating RRIM and 3D visualizations into feasibility studies and environmental assessments is vital for ensuring the safety and sustainability of hydropower infrastructures, particularly in challenging terrains like the Himalayan region.

Challenges and Limitations

A key limitation in this study is the resolution of 12.5 m x12.5 m pixels DEM data used for the preparation of RRIM. Although this dataset was the most accessible, it is recognized that using higher-resolution data, such as LiDAR or airborne surveys, would yield significantly better results, especially in complex mountainous regions and provide more reliable risk assessments.

Figure 12 illustrates an RRIM generated from high-resolution LiDAR survey data, showcasing its effectiveness in detailed topographic representation. The RRIM technique enhances subtle terrain features by combining slope and openness, allowing for clearer visualization of surface morphology, including landslide scars, ridge lines, drainage patterns, and fault traces. The use of LiDAR data significantly improves the accuracy of elevation models, especially in densely vegetated or rugged terrain, making RRIM a valuable tool for geomorphological analysis and landslide susceptibility assessment. This example demonstrates the superior capability of LiDAR-derived RRIM in detecting micro-topographic variations that are often missed in conventional DEM-based visualizations.

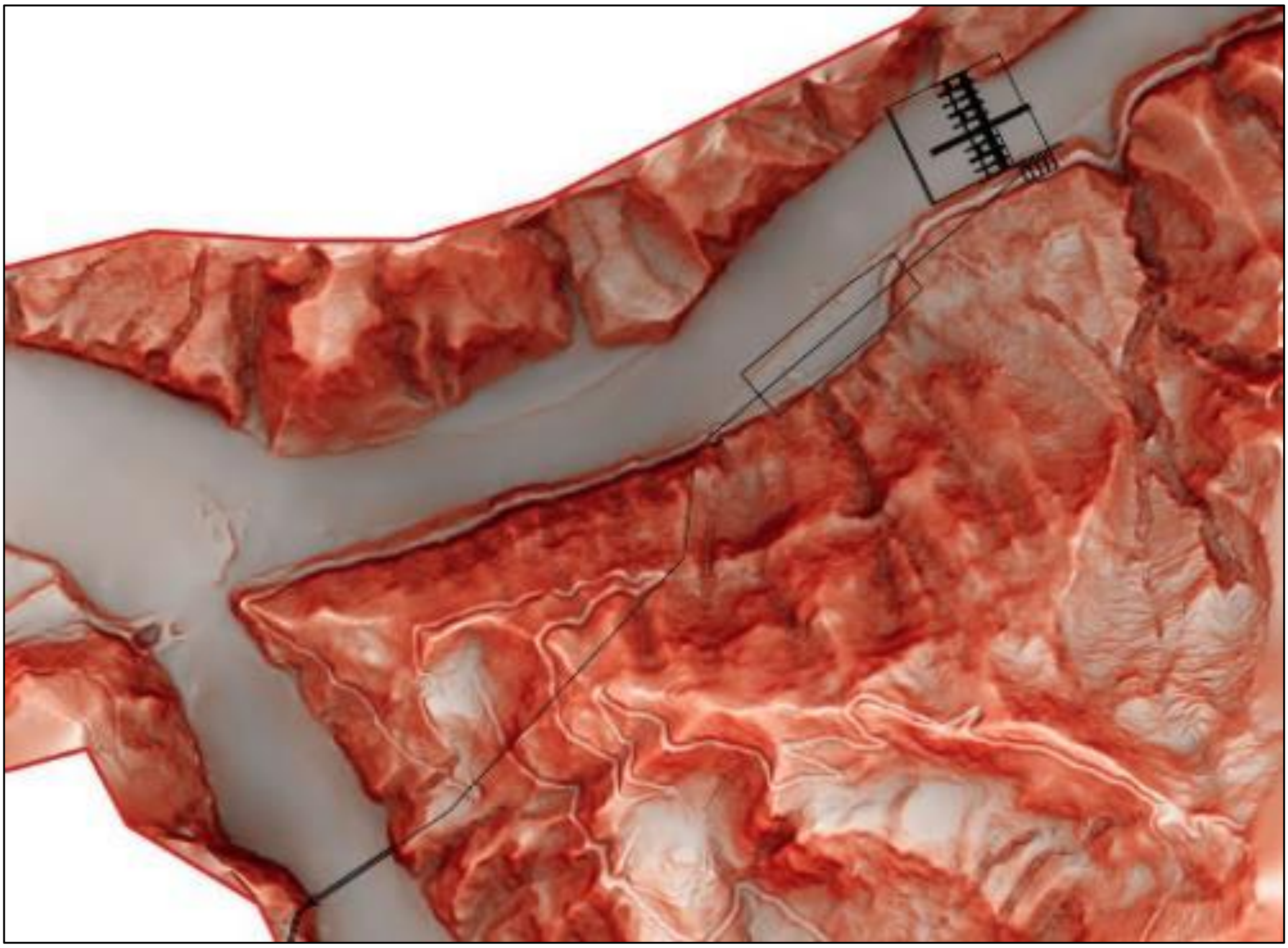

Figure 12, Example of a RRIM generated from LiDAR survey data.

Conclusions and Future Works

In conclusion, the RRIM has been prepared for all 20-master planned storage-type hydropower, diversion and multipurpose projects of Nepal. This study demonstrates the advantages of employing RRIM for terrain analysis in landslides prone area. Illustrating the complexity of the terrain and highlighting areas susceptible to deep-seated landslides. The addition of 3D visualization techniques further enriches the analysis, offering a more comprehensive understanding of the terrain. Future research should prioritize incorporating additional datasets, such as geological and hydrological information, along with reservoir slope stability and modeling approaches, to enhance the understanding of landslide dynamics and advance risk assessment methodologies. To further refine this technique, it is recommended that future projects incorporate higher-resolution DEM data, such as LiDAR or airborne surveys, to enhance the accuracy of the RRIM. Furthermore, the identification of deep-seated landslides should be verified through InSAR analysis or other suitable remote sensing techniques. This should be combined with field surveys to validate the results and ensure that critical terrain features are accurately captured. Moreover, expanding the use of this approach across the broader hydropower sector, particularly in evaluating reservoir slope stability, addressing potential slope failures during impoundment or rapid drawdown, and supporting mitigation planning, will contribute significantly to improved project design, safety and risk management.

Supplementary Data

Appendix -I: A step-by-step tutorial for the preparation Red Relief Image Map (RRIM) using QGIS. Attached with the paper.

Appendix -II: Full format Red Relief Image Map of all 20 Master Plan Storage-Type Hydropower, Diversion and Multipurpose Projects of Nepal. Attached with the paper.

Acknowledgment

The authors express their sincere gratitude to all the reviewers for their valuable recommendations and insightful feedback, which significantly contributed to improving the quality of this manuscript.

Funding: This research received no external funding.

Data Availability Statement: All data sources utilized in this study are publicly available and have been clearly described within the article. No proprietary or restricted datasets were used.

The data supporting the findings of this study are available within the article and its supplementary materials.

Conflicts of Interest: The authors declare no conflict of interest.

References

Alaska (2024), Alaska Satellite Facility. Retrieved from https://asf.alaska.edu. Accessed on 2024-07-08.

Bhandary N. P., Yatabe R., Hasegawa S. and Dahal R. K. (2011). Characteristic features of deep-seated landslides in Mid-Nepal Himalayas: spatial distribution and mineralogical evaluation. In Geo-Frontiers 2011: Advances in Geotechnical Engineering, 1693-1702. https://doi.org/10.1061/41165(397)173.

Chiba T., Kaneta S. and Suzuki Y. (2008). Red relief image map: new visualization method for three-dimensional data. The International Archives of the Photogrammetry, Remote Sensing and Spatial Information Sciences, XXXVII, 1071-1076.

Copernicus (2024). Copernicus Open Access Hub. Sentinel-2 imagery. European Space Agency. Retrived from https://www.copernicus.eu/en. Accessed on 2024-02-03.

Dahal R.K. (2015). Understanding of Landslide Science in the Nepal Himalaya. In: Lollino, G., et al. Engineering Geology for Society and Territory- Volume 2. Springer, Cham. https://doi.org/10.1007/978-3-319-09057-3_228.

Daxer C. (2020). Topographic Openness Maps and Red Relief Image Maps in QGIS. Technical Report, 17p. https://doi.org/10.13140/RG.2.2.18958.31047.

DoED (2024) Department of Electricity Development (DoED), GoN Project Bank: Under Study Projects, Retrieved from http://www.doed.gov.np. Accessed on 2024-06-24.

NEA and JICA (2014). Nepal Electricity Authority (NEA) and Japan International Cooperation Agency (JICA) report of Nationwide Master Plan Study on Storage-type Hydropower Power Development in Nepal, NEA, Nepal. Unpublished Report, 102p. Retrieved from https://openjicareport.jica.go.jp/pdf/12147310.pdf Accessed on 2024-06-06.

Timalsina K. and Paudyal K. R. (2018). Fault-controlled geomorphic features in Ridi-Shantipur area of Gulmi District and their implications for active tectonics. Journal of Nepal Geological Society, 55 (1), 157–165. https://doi.org/10.3126/jngs.v55i1.22807.

Timilsina M., Bhandary N.P., Dahal R.K. and Yatabe R. (2017). Large-Scale Landslide Inventory Mapping in Lesser Himalaya of Nepal Using Geographic Information System. In: Yamagishi H., Bhandary N. (eds) GIS Landslide. Springer, Tokyo. https://doi.org/10.1007/978-4-431-54391-6_6 .

Yokoyama R., Shirasawa M. and Pike R.J. (2002). Visualizing topography by openness. A new application of image processing to DEMs. Photogrammetric Engineering & Remote Sensing, 68, 257-265. Retrieved from https://www.asprs.org/wp-content/uploads/pers/2002journal/march/2002_mar_257-265.pdf. Accessed on 2024-05-12.

Supplementary Data

Vol 1 No. 1 and 2, 17-25

Red Relief Image Maps to Visualize Landslide Risks in Master-Planned Storage-Type Hydropower Projects in Nepal Using a Free and Open-Source GIS Approach

Milan Kumar Rai and Anjila Babu Malla

Appendix - 1: A step-by-step tutorial for the preparation Red Relief Image Map (RRIM) using QGIS.

Appendix - 2: Full format Red Relief Image Map of all 20 Master Plan Storage-Type Hydropower, Diversion and Multipurpose Projects of Nepal

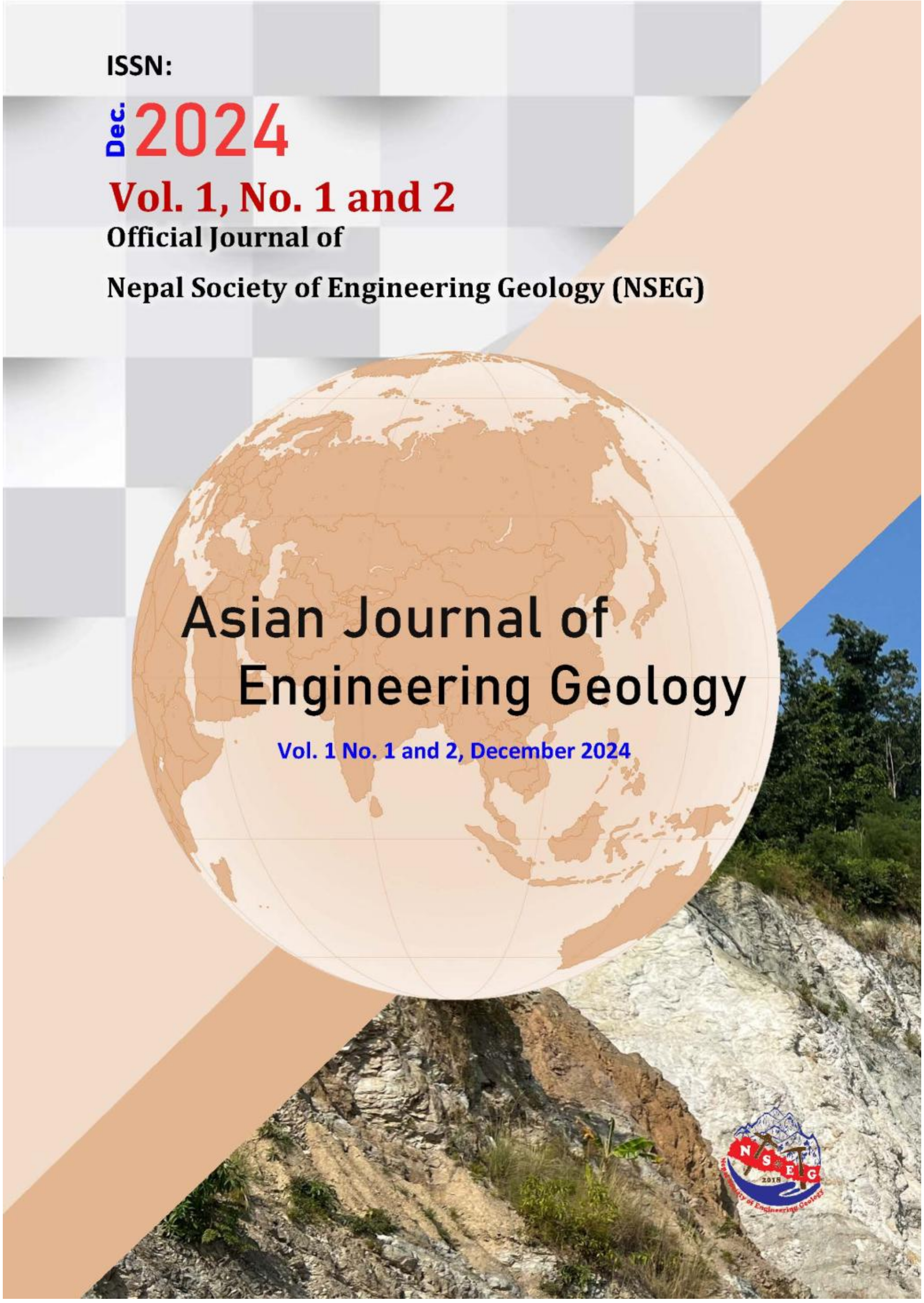

Appendix – 1

A step-by-step tutorial for the preparation Red Relief Image Map (RRIM) using QGIS.

Step 1: Add the DEM

First, we must add the DEM, either by dragging and dropping the raster file from its folder into the map window, or by clicking Layer - Add Layer - Add Raster Layer (Figure Sup 13).

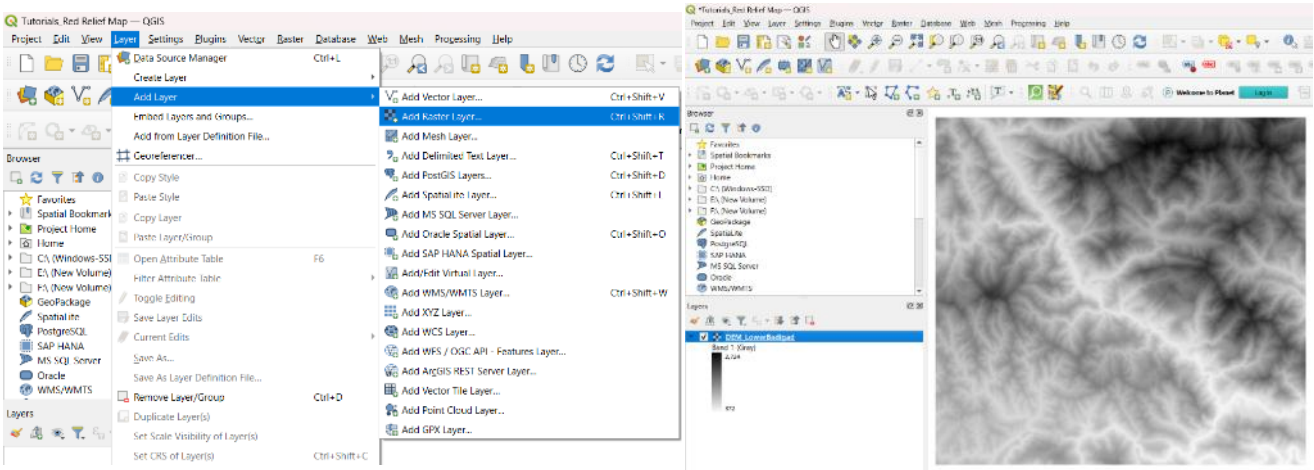

Figure Sup 13, Add Raster Layer.

Step 2: Calculating the Slope angle

For the calculation of slope angle, Search for the 'Slope' in the Processing Toolbox and click on it. Then 'Slope' window opens.

- Select required DEM as the elevation layer and click run (Figure Sup 14).

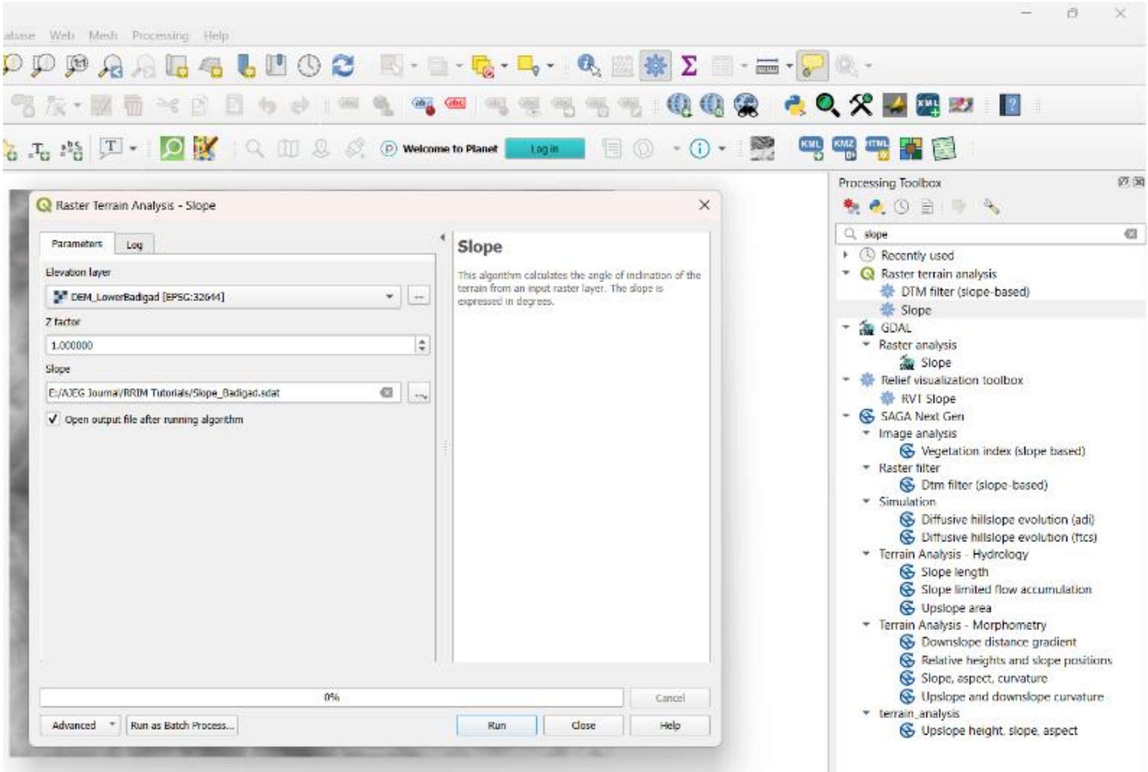

Elevation layer: DEM_LowerBadigad [EPSG:32644]

Z factor: 1.000000

Slope: E:/AJEG Journal/RRIM Tutorials/Slope_Badigad.sdat

☑ Open output file after running algorithm

Search: slope

Slope

This algorithm calculates the angle of inclination of the terrain from an input raster layer. The slope is expressed in degrees.

Figure Sup 14, Calculating the Slope angle.

- Changing the rendered colors of Slope map
- Click on Symbology in layer properties of slope map (Figure Sup 15).
- Render type – Single band gray to Single band pseudocolor
- Change the color ramp to 'Reds'
- Layer rendering – Blending mode – 'Multiply' – Click apply.

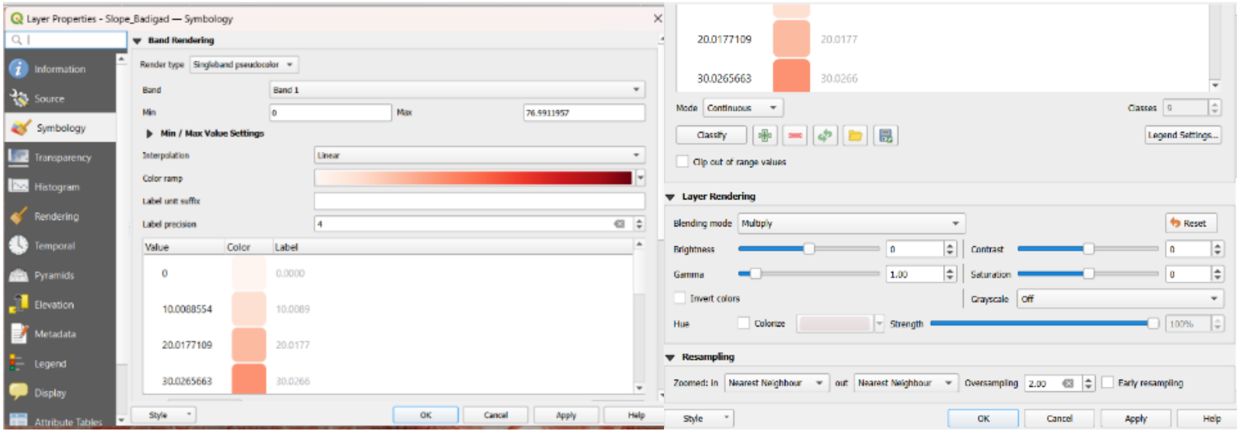

Layer Properties - Slope_Badigad — Symbology

Band Rendering

Render type: Singleband pseudocolor

Band: Band 1

Min: 0 Max: 76.9911957

Min / Max Value Settings

Interpolation: Linear

Label precision: 4

Value	Color	Label
0		0.0000
10.0088554		10.0089
20.0177109		20.0177
30.0265663		30.0266

Mode: Continuous Classes: 0

☐ Clip out of range values

Layer Rendering

Blending mode: Multiply

Brightness: 0 Contrast: 0

Gamma: 1.00 Saturation: 0

☐ Invert colors Grayscale: Off

Hue ☐ Colorize Strength: 100%

Resampling

Zoomed: in Nearest Neighbour out Nearest Neighbour Oversampling 2.00 ☐ Early resampling

Figure Sup 15, Symbology and layer rendering of Slope map.

The slope map looks like to Figure Sup 16.

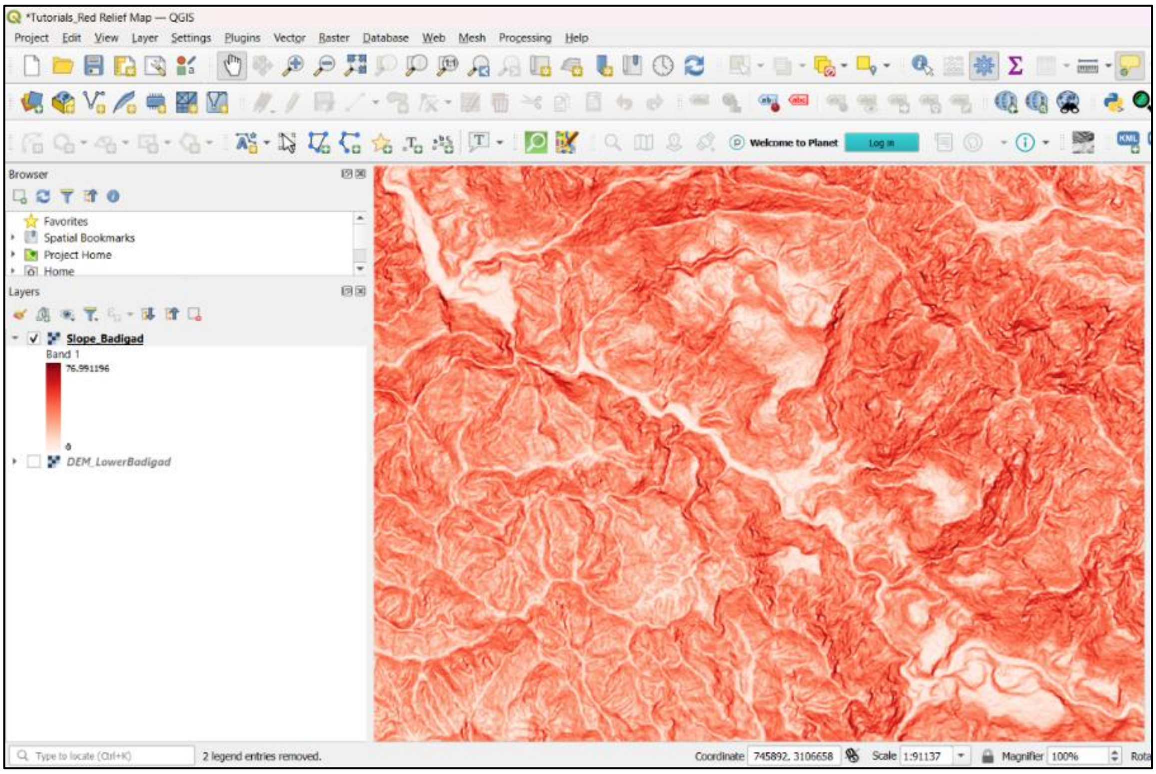

*Tutorials_Red Relief Map — QGIS

Layers: ☑ Slope_Badigad, Band 1, 76.991196, 0; ☐ DEM_LowerBadigad

2 legend entries removed.

Coordinate 745892, 3106658 Scale 1:91137 Magnifier 100%

Figure Sup 16, Slope map.

Step 3: Generating positive and negative openness maps

First of all, make sure that the SAGA –'System for Automated Geoscientific Analyses' plugin installed or not, if not, firstly download and install all the necessary modules as well as SAGA GIS and all its calculating algorithms as required computer operating system. If you are using latest versions of QGIS, you have to download SAGA GIS separately from official website of SAGA GIS (https://saga-gis.sourceforge.io/en/index.html)

For generate the positive openness and negative openness map, in the processing toolbox, search for 'Openness' and click on "Topographic Openness" or Go to SAGA next gen-Terrain analysis lighting-Topographic openness (Figure Sup 17).

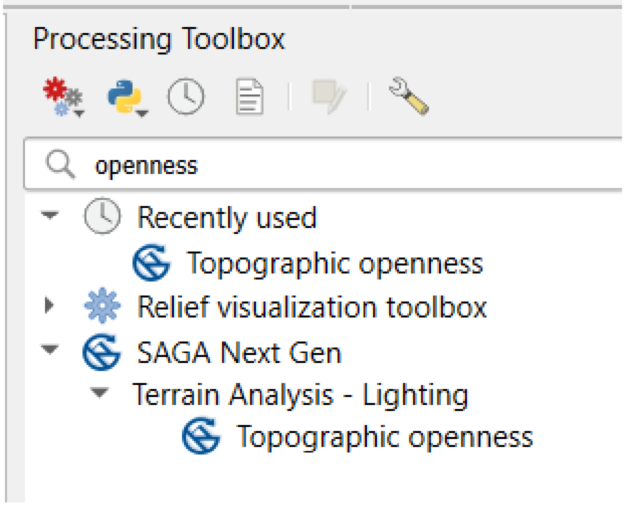

Figure Sup 17, Processing Toolbox for Topographic openness.

This will open the Topographic openness module window, where you can choose certain parameters (Figure Sup 18, Figure Sup 19 and Figure Sup 20).

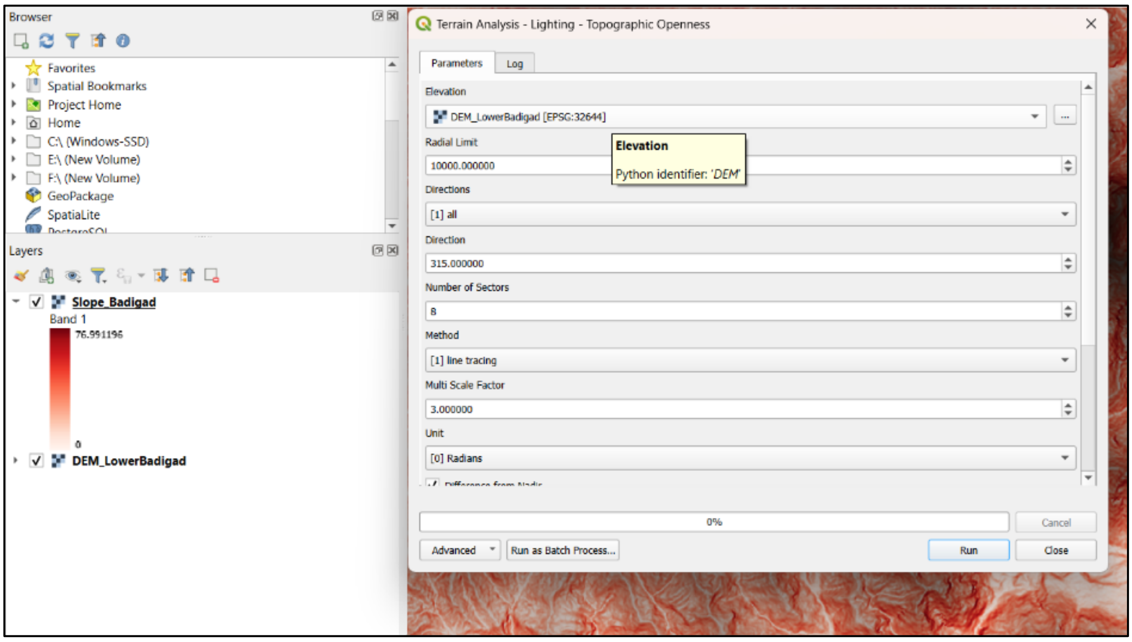

Elevation: DEM_LowerBadigad [EPSG:32644]
Radial Limit: 10000.000000
Directions: [1] all
Direction: 315.000000
Number of Sectors: 8
Method: [1] line tracing
Multi Scale Factor: 3.000000
Unit: [0] Radians

Figure Sup 18, Topographic openness module window.

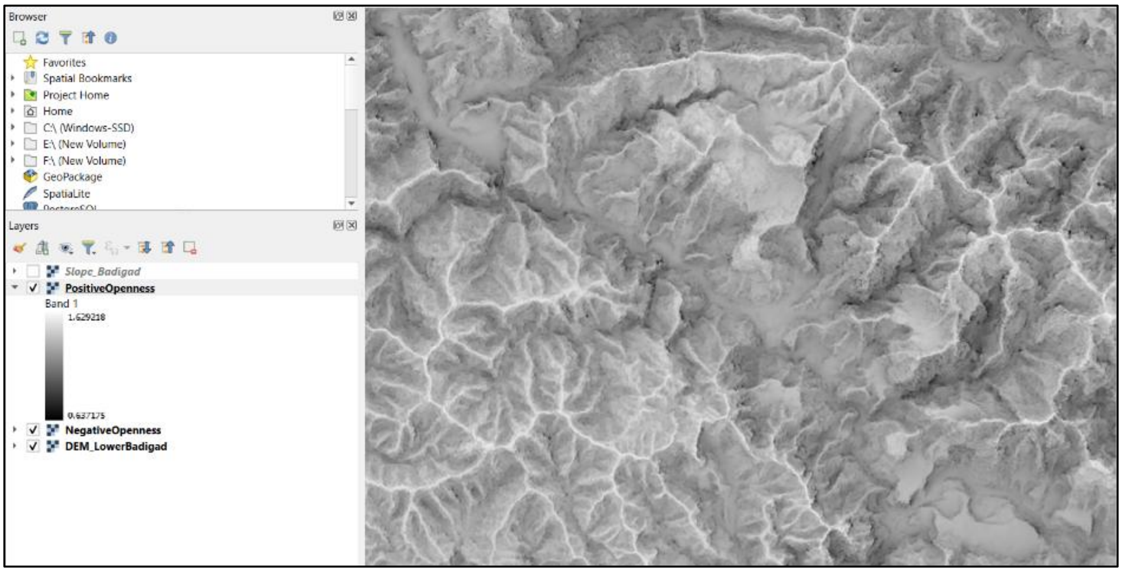

Figure Sup 19, Positive openness raster map.

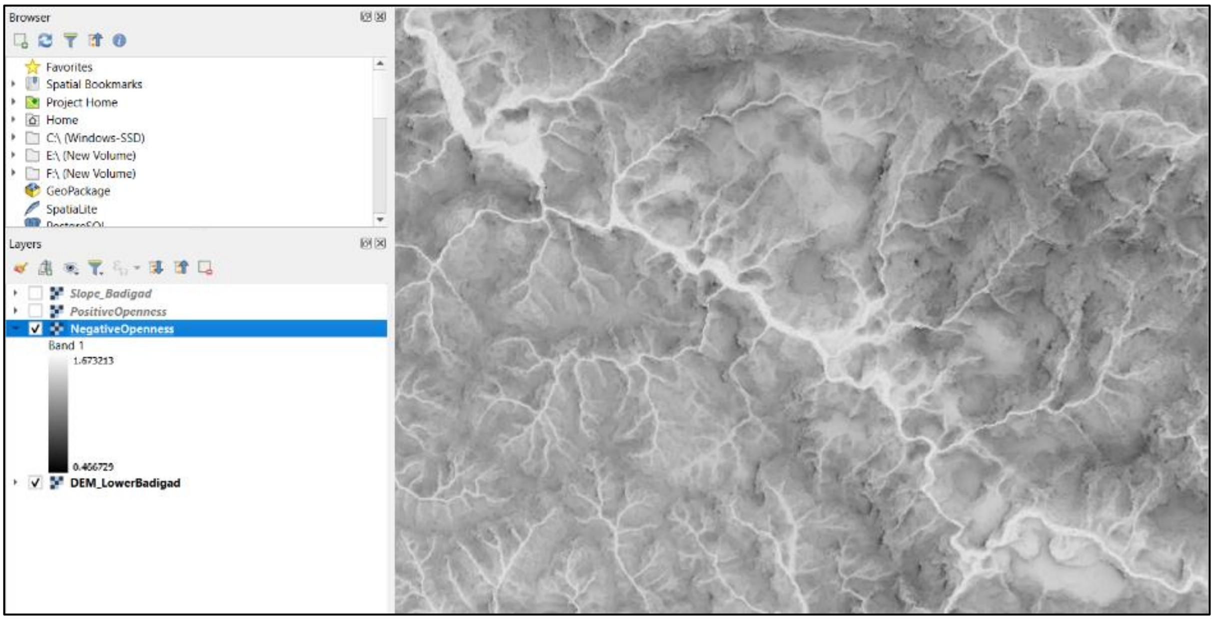

Figure Sup 20, Negative openness raster map.

Step 4: Calculating the Differential Openness raster

After generating the positive and negative openness raster, the raster calculator (Raster - Raster calculator) is used to calculate the differential openness raster as according to the formula (Figure Sup 21),

(Positive Openness – Negative Openness)/2

i.e. (Op-On)/2

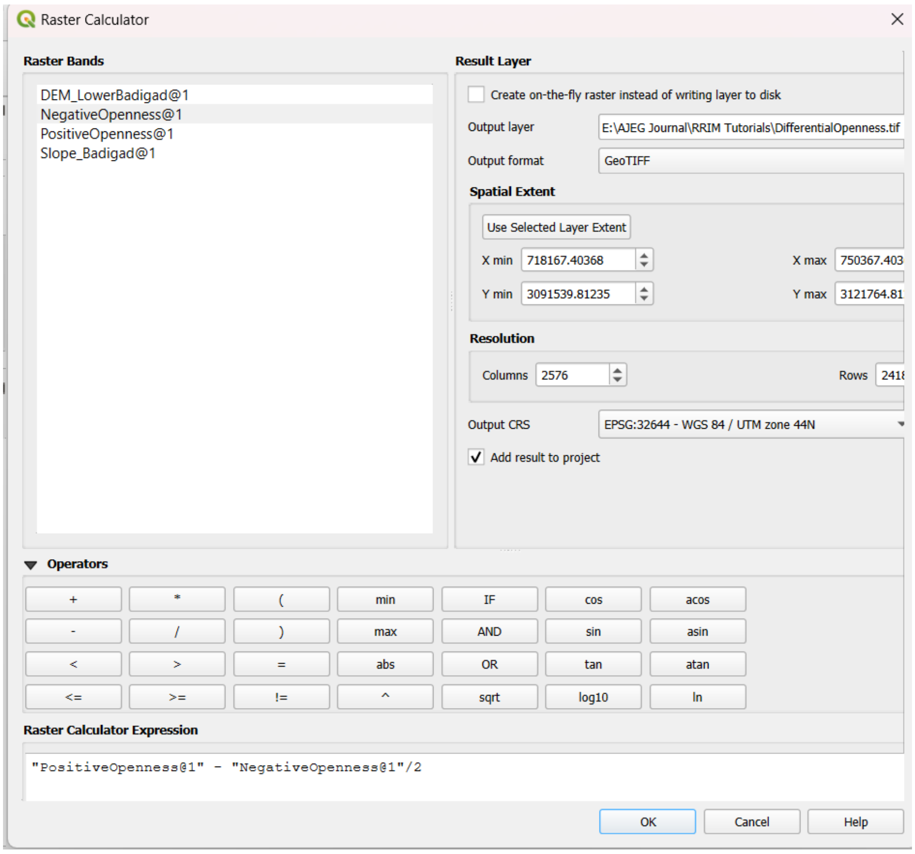

DEM_LowerBadigad@1
NegativeOpenness@1
PositiveOpenness@1
Slope_Badigad@1

☐ Create on-the-fly raster instead of writing layer to disk

Output layer: E:\AJEG Journal\RRIM Tutorials\DifferentialOpenness.tif

Output format: GeoTIFF

X min: 718167.40368

X max: 750367.403

Y min: 3091539.81235

Y max: 3121764.81

Columns: 2576

Rows: 241

Output CRS: EPSG:32644 - WGS 84 / UTM zone 44N

☑ Add result to project

Raster Calculator Expression

```
"PositiveOpenness@1" - "NegativeOpenness@1"/2
```

Figure Sup 21, Raster calculator module window.

Step 5: Enhancing the Differential Openness raster

After calculation, differential openness map should be enhanced to improve contrast for better visualization.

- Double click on the differential openness raster

- Click on Symbology in layer properties of raster.
- Contrast enhancement is set to Min/Max value settings (you can select several options depending on what should be highlighted) and click apply.

The result map looks like Figure Sup 22.

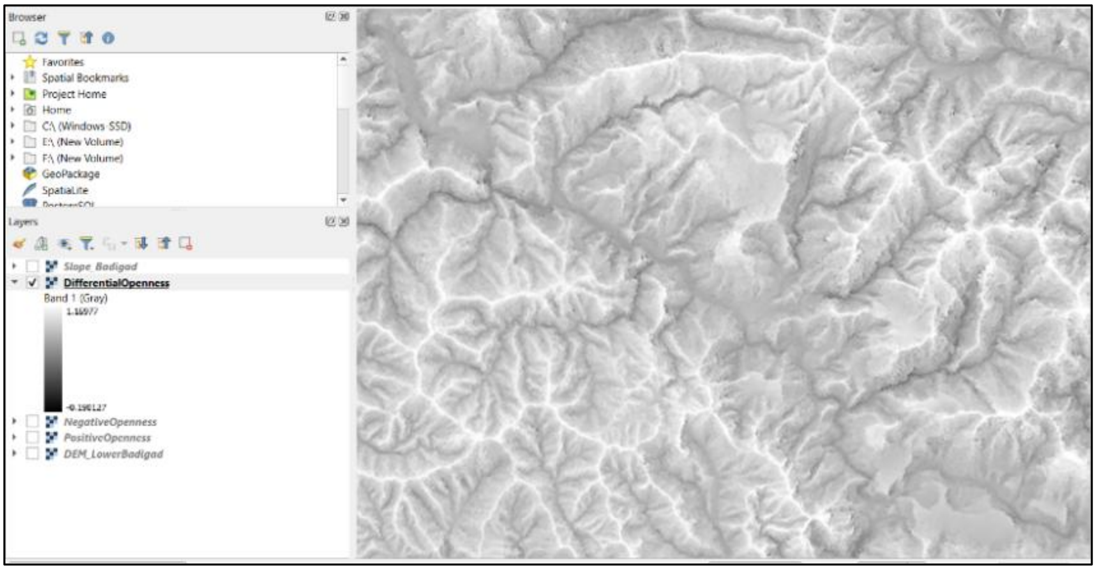

Figure Sup 22, Differential openness raster map.

At the last, first make sure that the slope raster is placed on top of the differential openness raster. The final RRIM map looks like to Figure Sup 23.

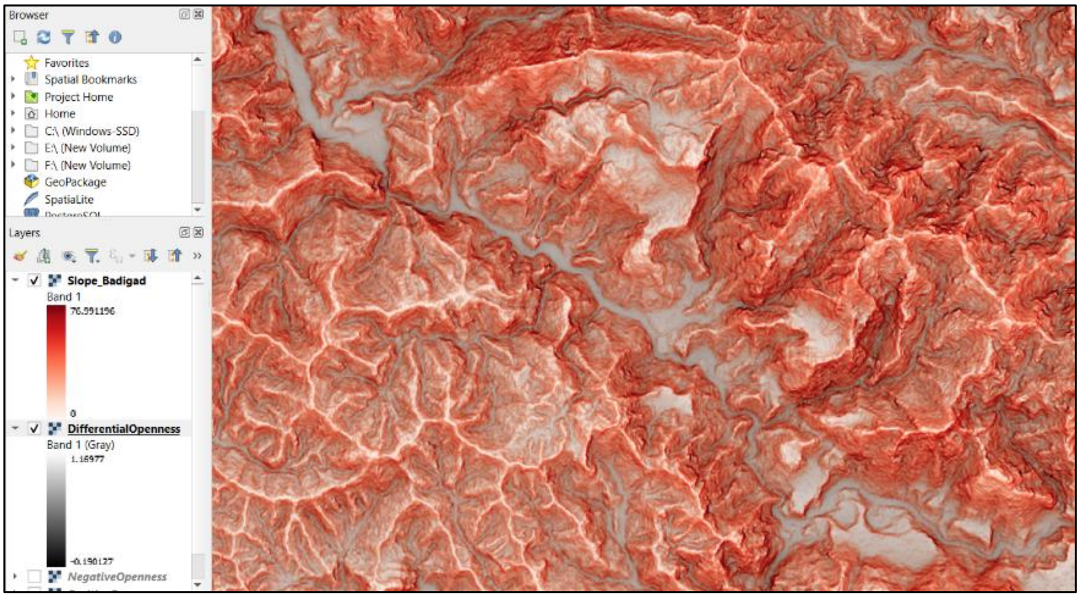

Figure Sup 23, Final Red Relief Image Map.

Step 6: 3D RRIM visualization

Worked on QGIS 3.x (e.g., 3.28, or newer)

1. Open the 3D Map View
    - In QGIS main window, go to the top menu bar.
    - Click View → New 3D Map View.
    - A new panel or window will appear with the 3D canvas.
2. Configure 3D Settings
    - Click the cogwheel icon ⚙ (top-right of the 3D Map View).
    - Under Terrain tab:

- Choose your DEM layer under "Elevation".
- Set a vertical scale factor to exaggerate the terrain for better visualization.

3. Apply RRIM as Surface Texture
    - In the same 3D configuration window:
    - Under "Surface" → "Map texture", choose your RRIM raster layer.
    - This overlays the RRIM onto the DEM in 3D.
4. Adjust Visualization Options
    - Pan, tilt, and zoom using mouse controls.
    - Adjust lighting and shading for enhanced terrain perception:
    - Settings → Lighting → Enable directional light or ambient light.

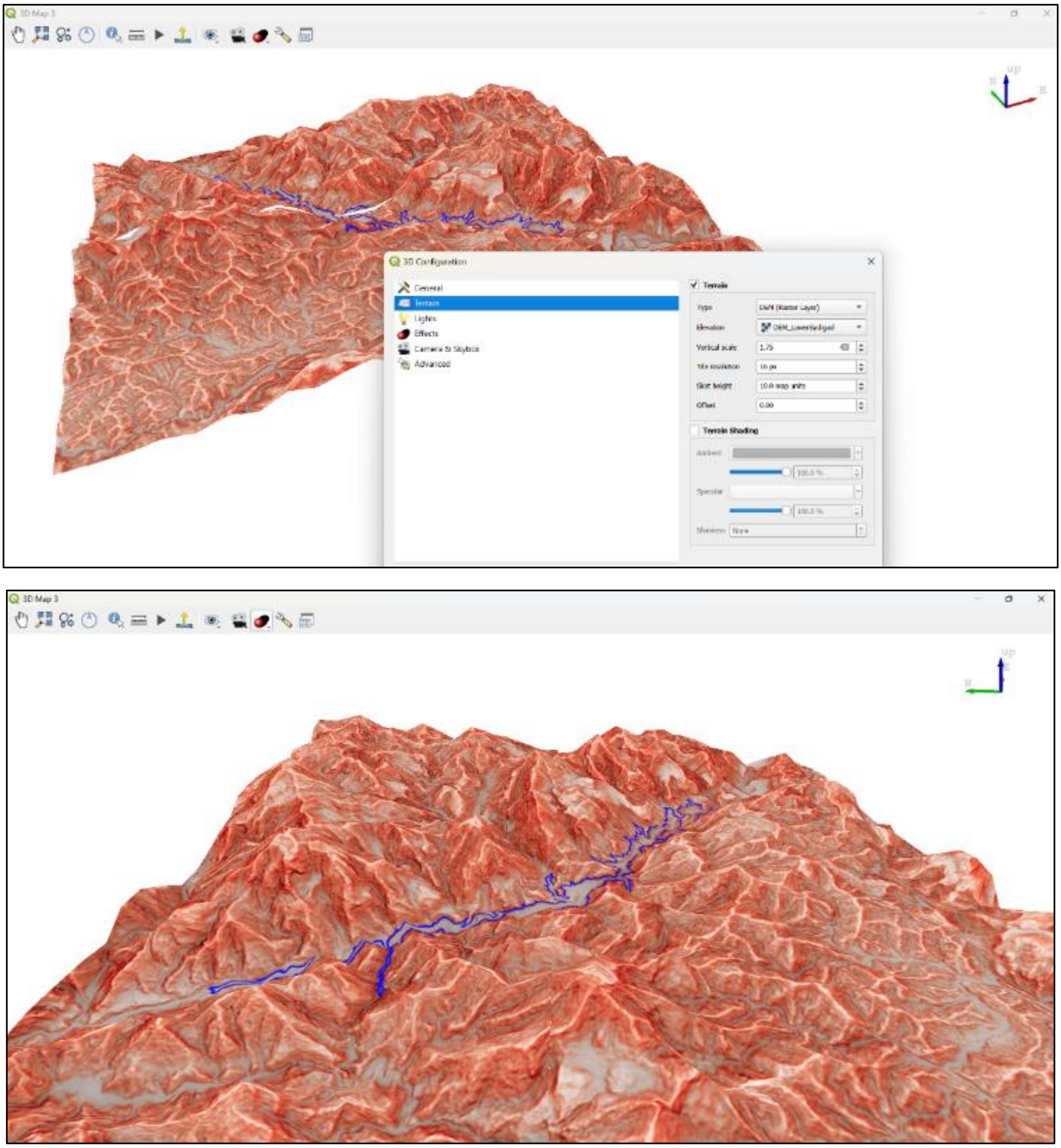

☑ Terrain

Type: DEM (Raster Layer)

Vertical scale: 1.75

Tile resolution: 16 px

Skirt height: 10.0 map units

Offset: 0.00

Figure Sup 24, 3D configuration window in QGIS.

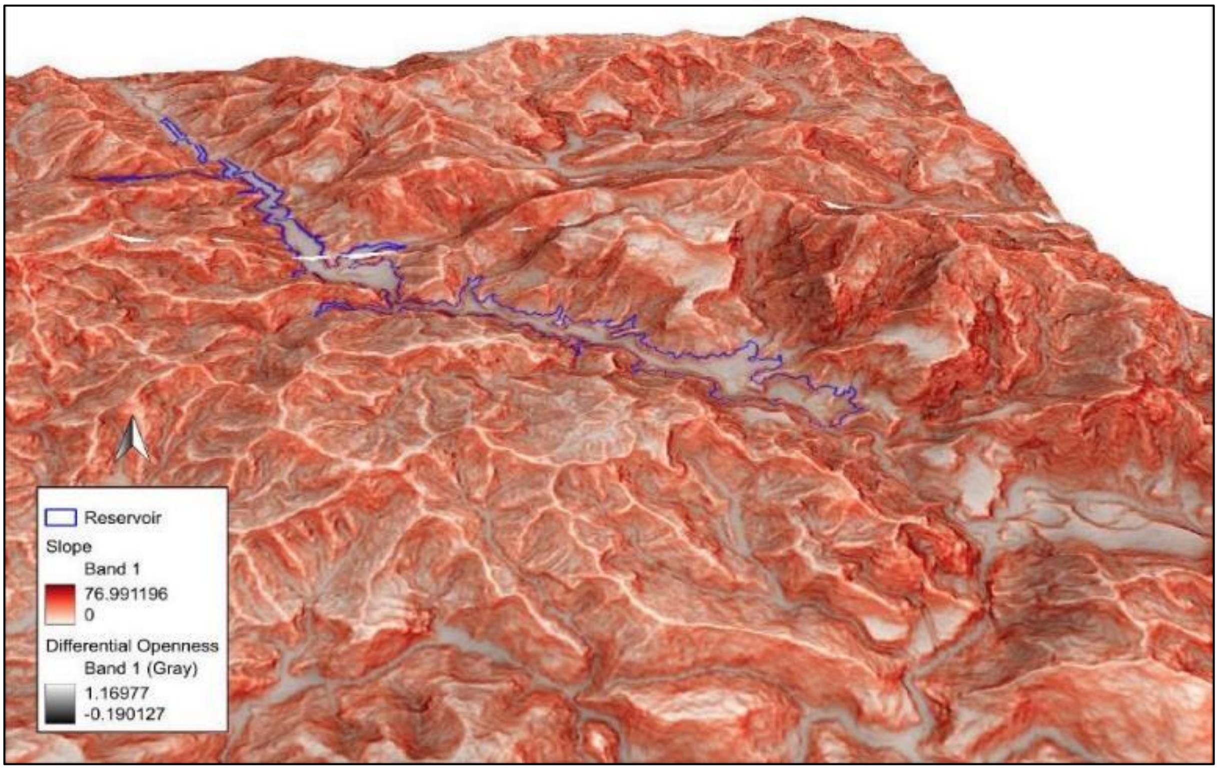

Figure Sup 25, 3D Red Relief Image Map (3D RRIM).

Appendix – 2

Full format Red Relief Image Map of all 20 Master Plan Storage-Type Hydropower, Diversion and Multipurpose Projects of Nepal

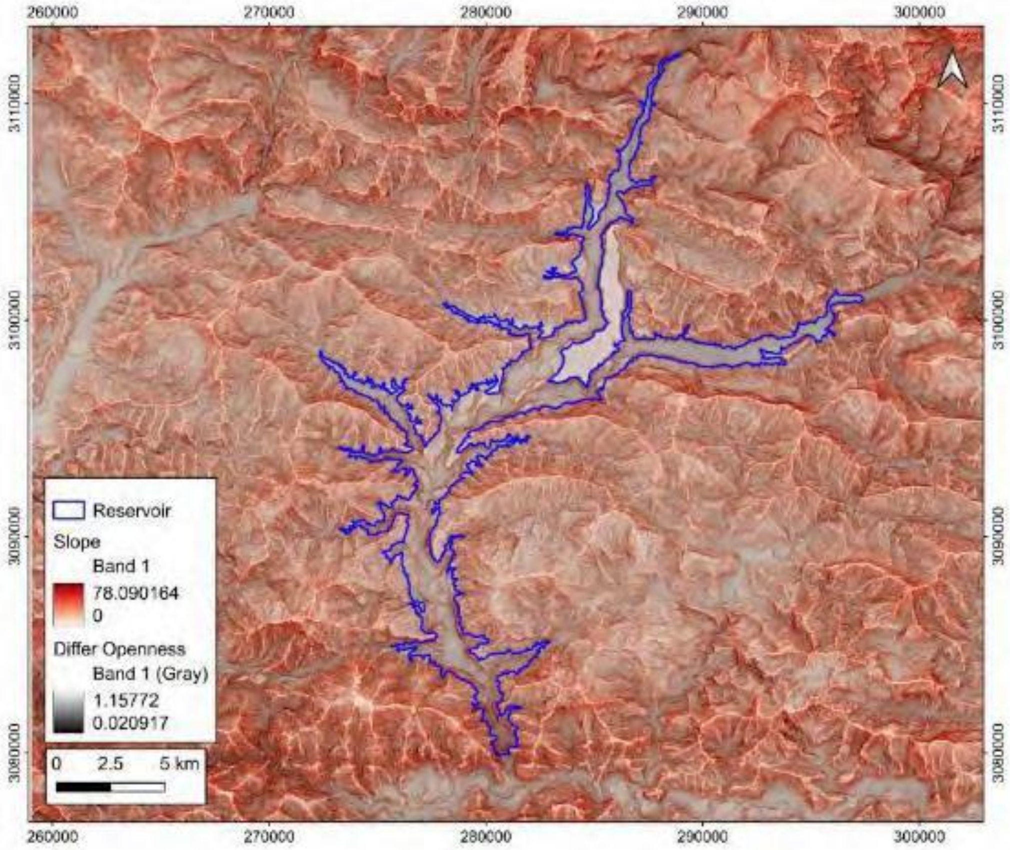

Figure Sup 26, Red Relief Image Map of Budhigandaki Hydropower Project.

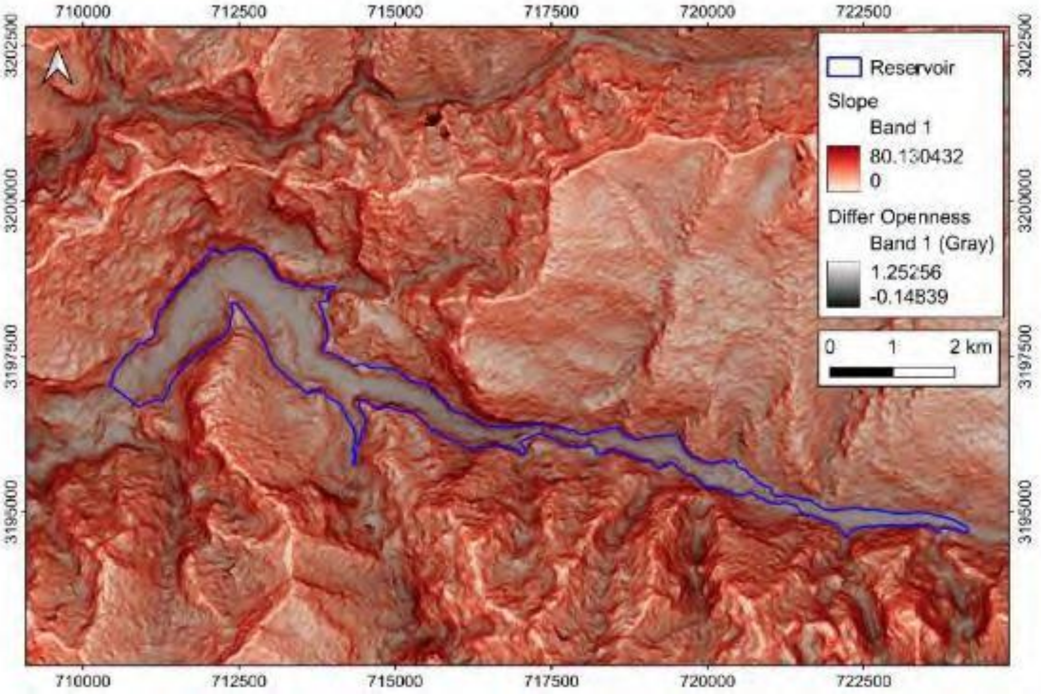

Figure Sup 27, Red Relief Image Map of Bharbung Storage Hydropower Project.

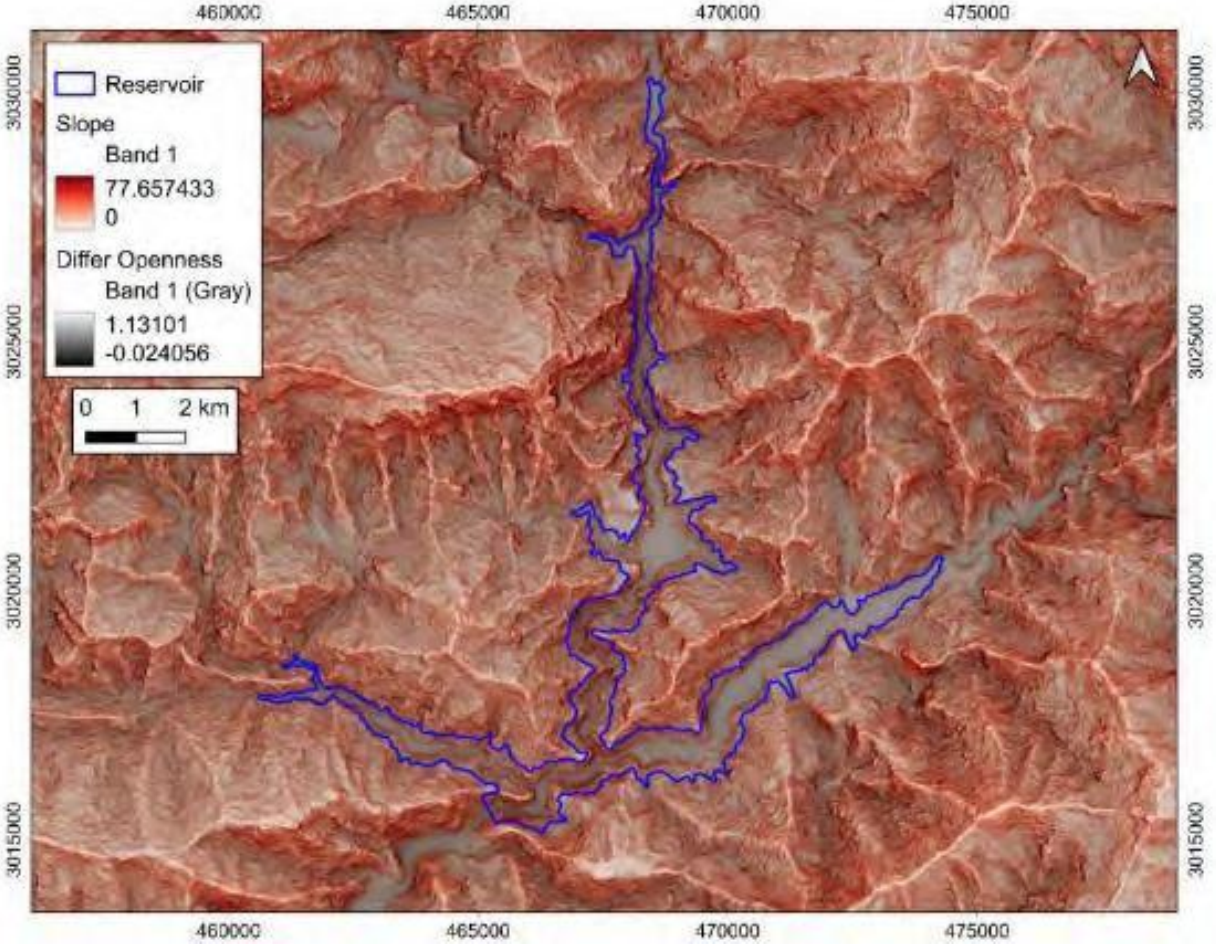

Figure Sup 28, Red Relief Image Map of Dudh Koshi Storage Hydropower Project.

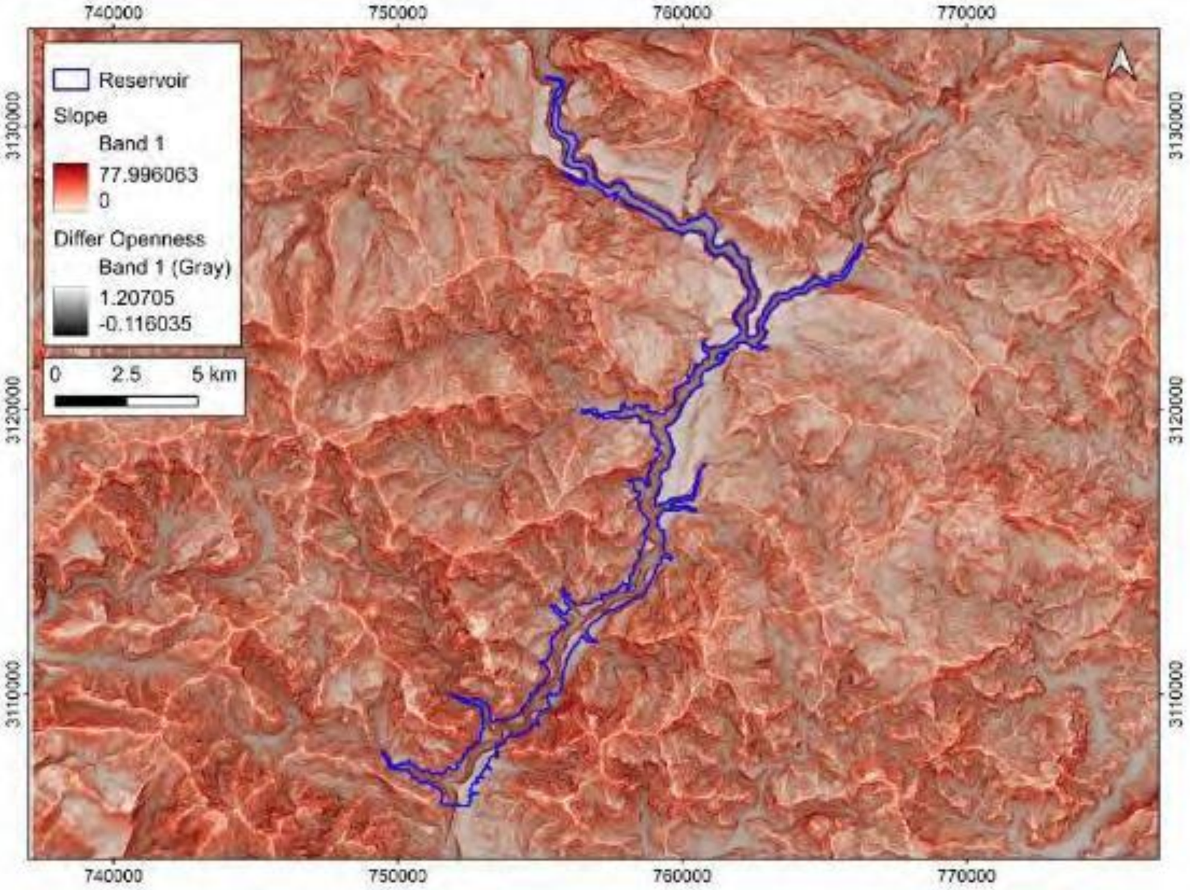

Figure Sup 29, Red Relief Image Map of Kaligandaki Storage Hydropower Project.

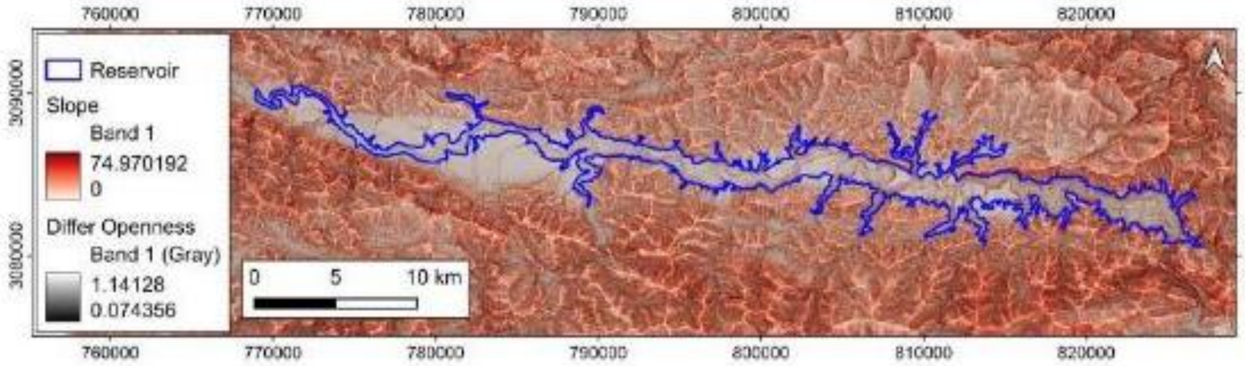

Figure Sup 30, Red Relief Image Map of Kaligandaki-2 Storage Hydropower Project.

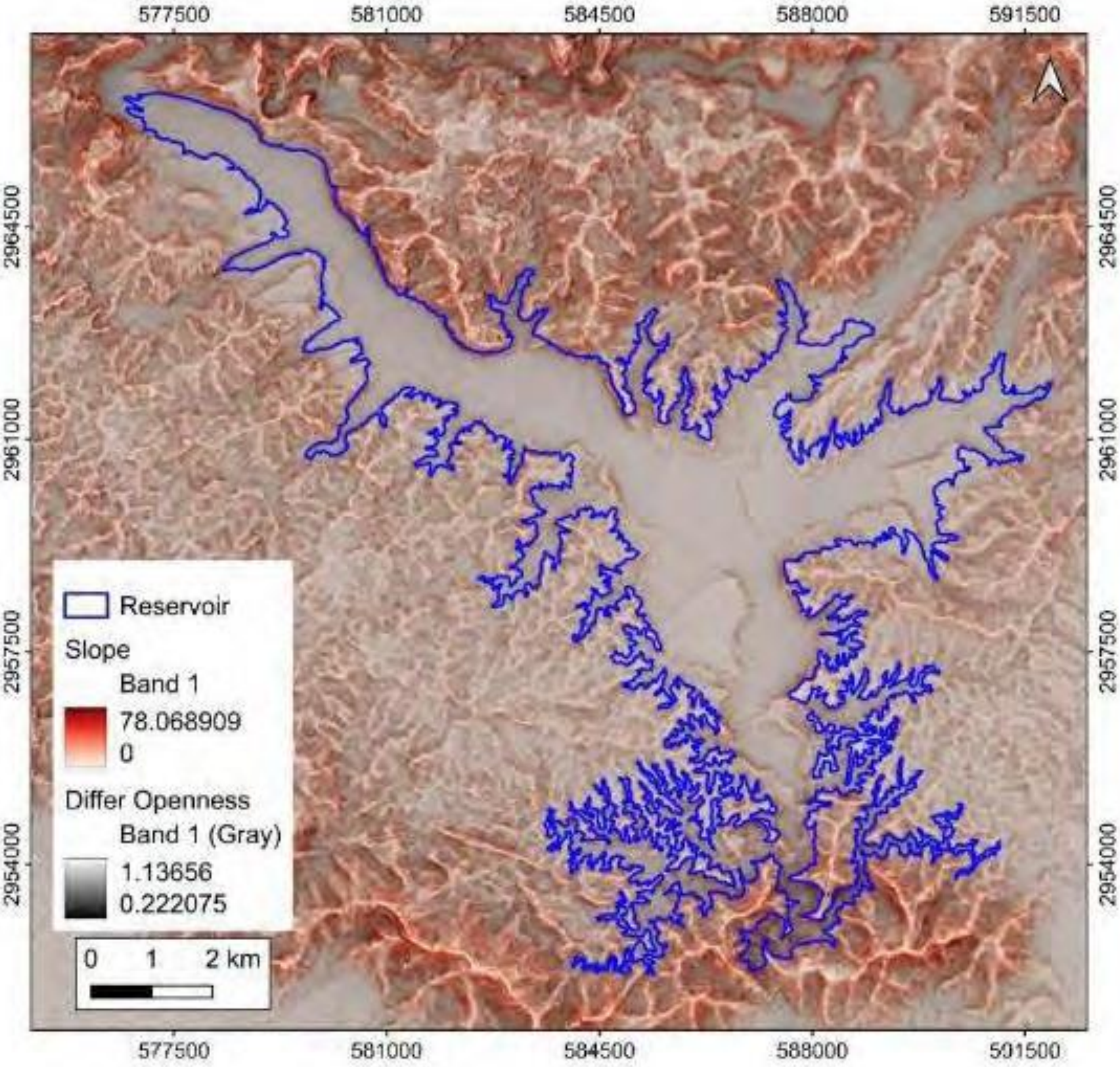

Figure Sup 31, Red Relief Image Map of Kankai Multipurpose Project.

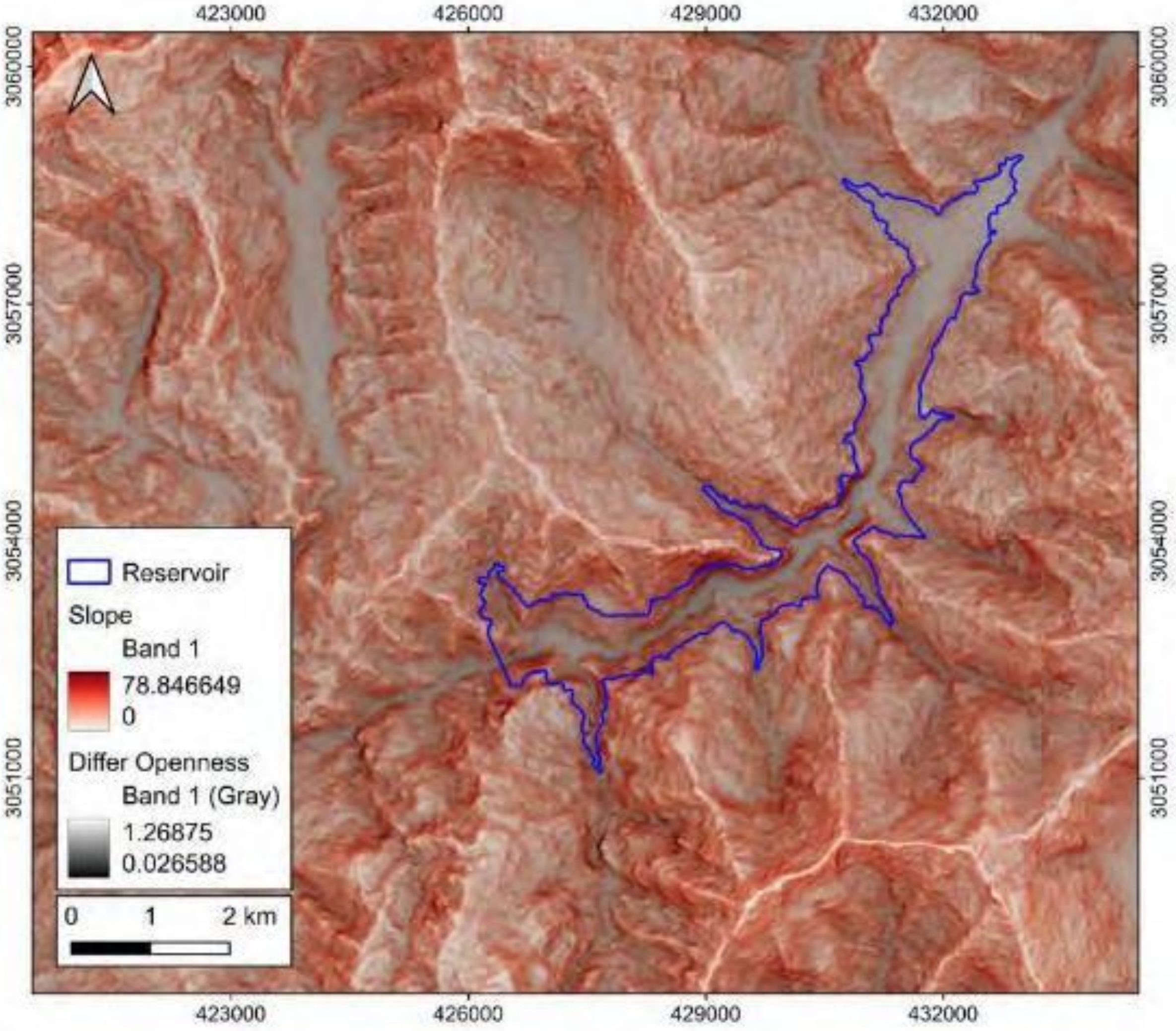

Figure Sup 32, *Red Relief Image Map of Khimti Those Siwalaya Storage Hydropower Project.*

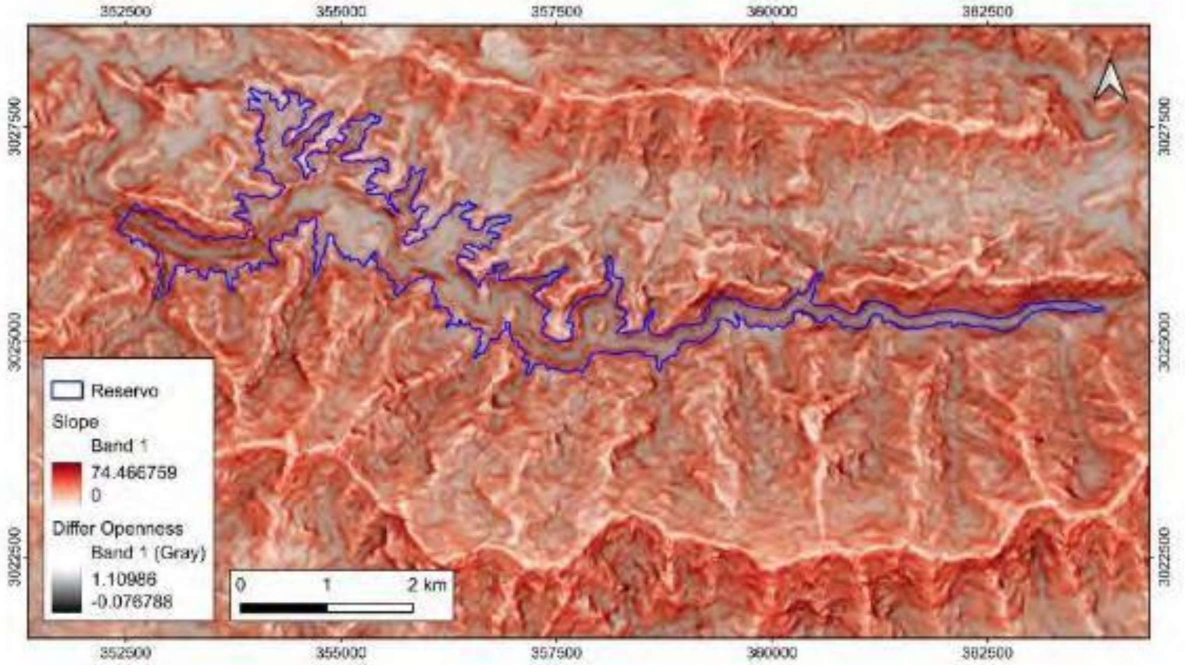

Figure Sup 33, *Red Relief Image Map of Kokhajor Storage Hydropower Project.*

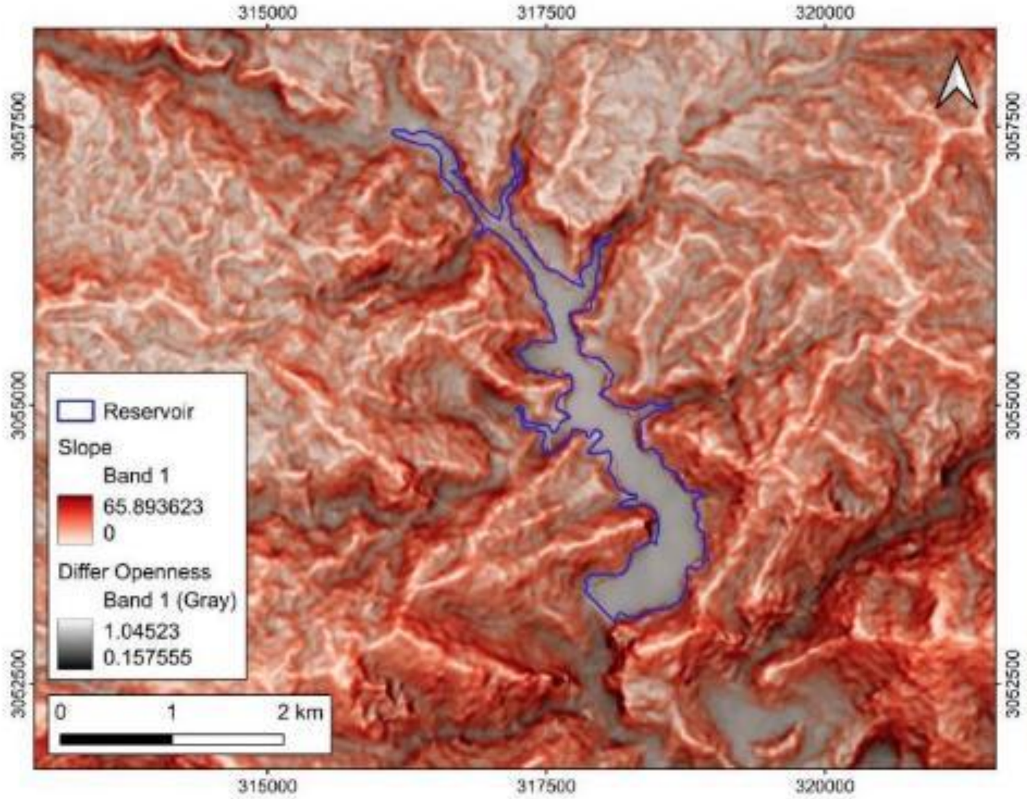

Figure Sup 34, Red Relief Image Map of Kulekhani Hydropower Project (Operated).

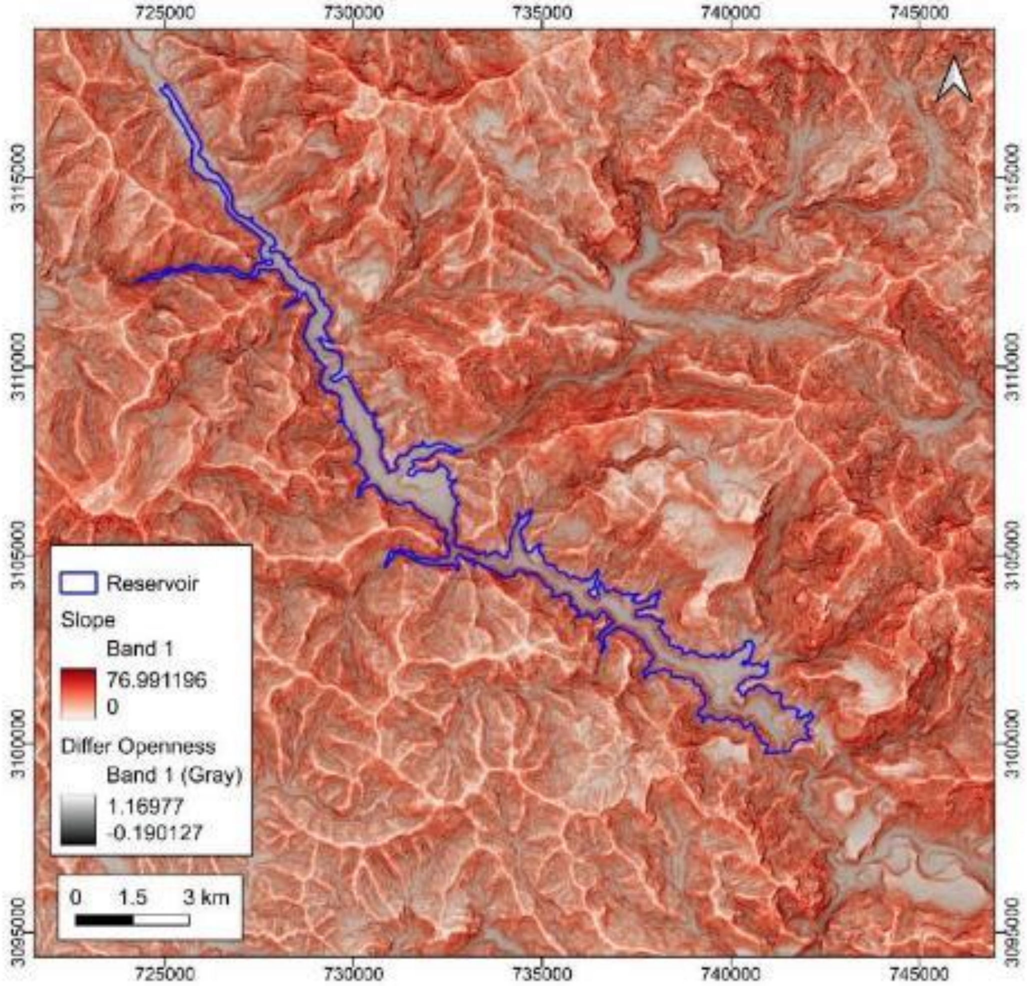

Figure Sup 35, Red Relief Image Map of Lower Badigad Storage Hydroelectric Project.

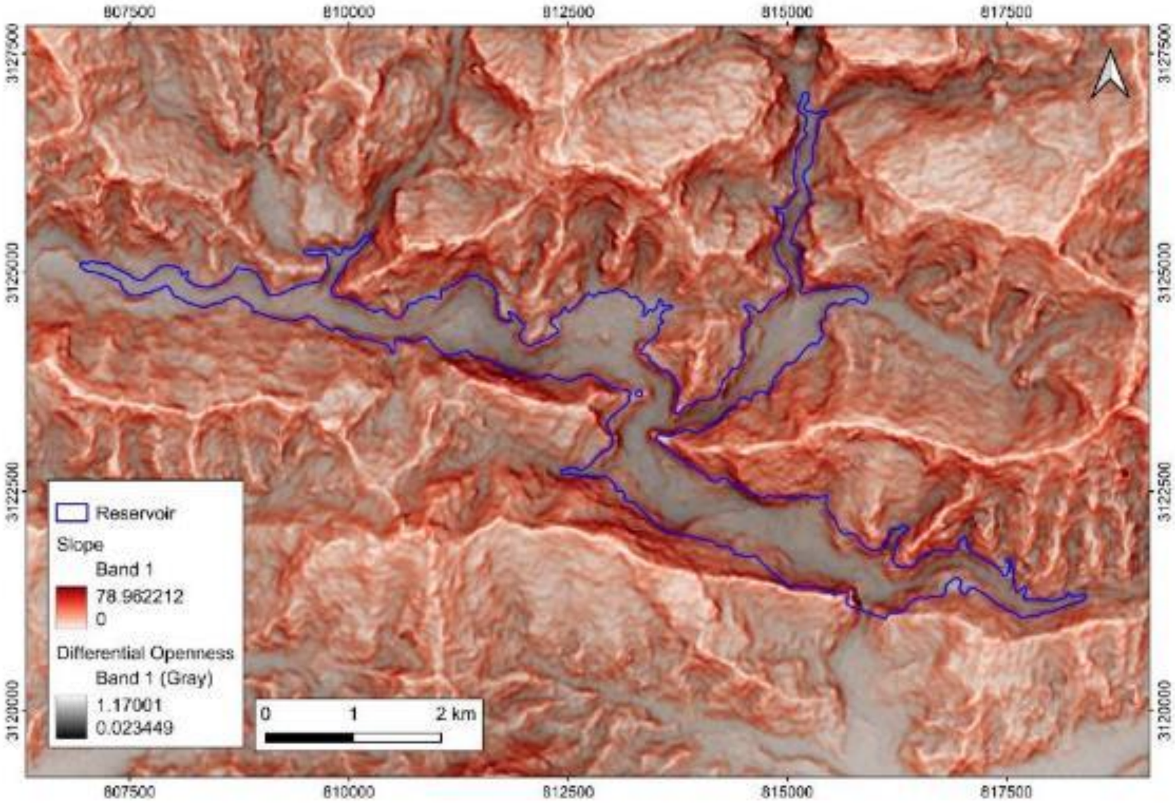

Figure Sup 36, Red Relief Image Map of Madi Siti Storage Hydropower Project.

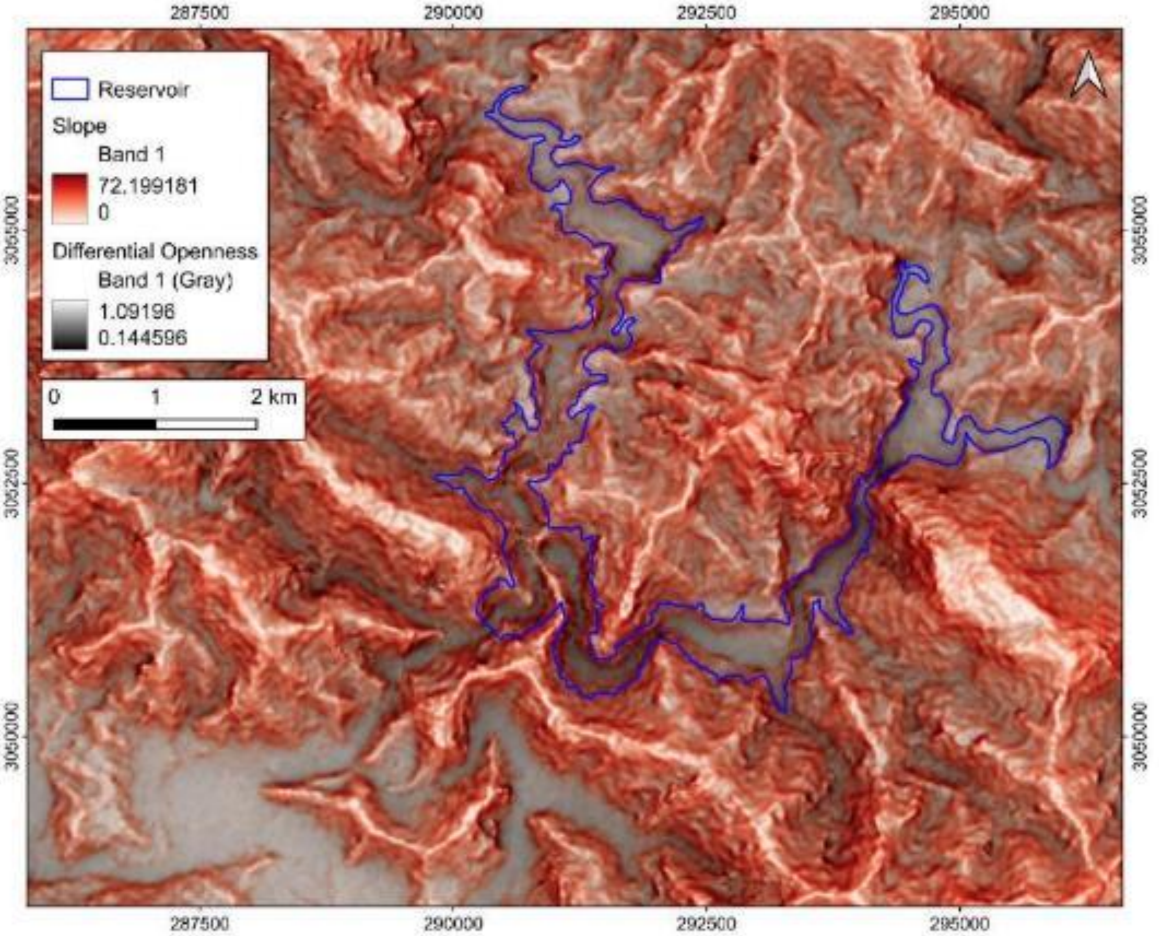

Figure Sup 37, Red Relief Image Map of Manahari Multipurpose Project.

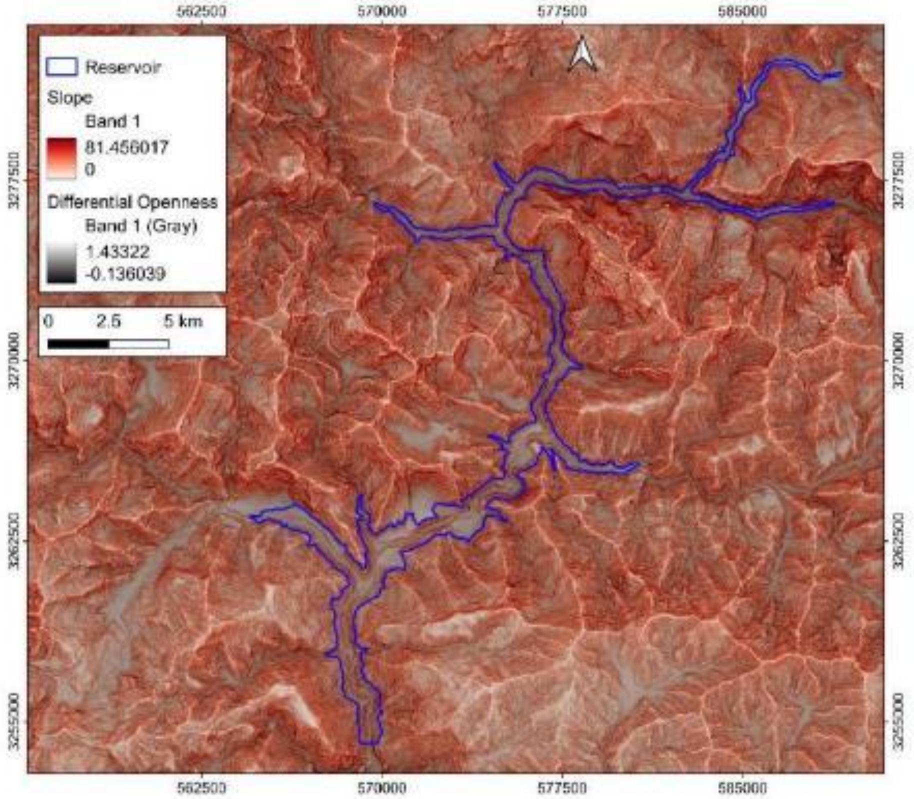

Figure Sup 38, Red Relief Image Map of Mugu Karnali Hydroelectric Project.

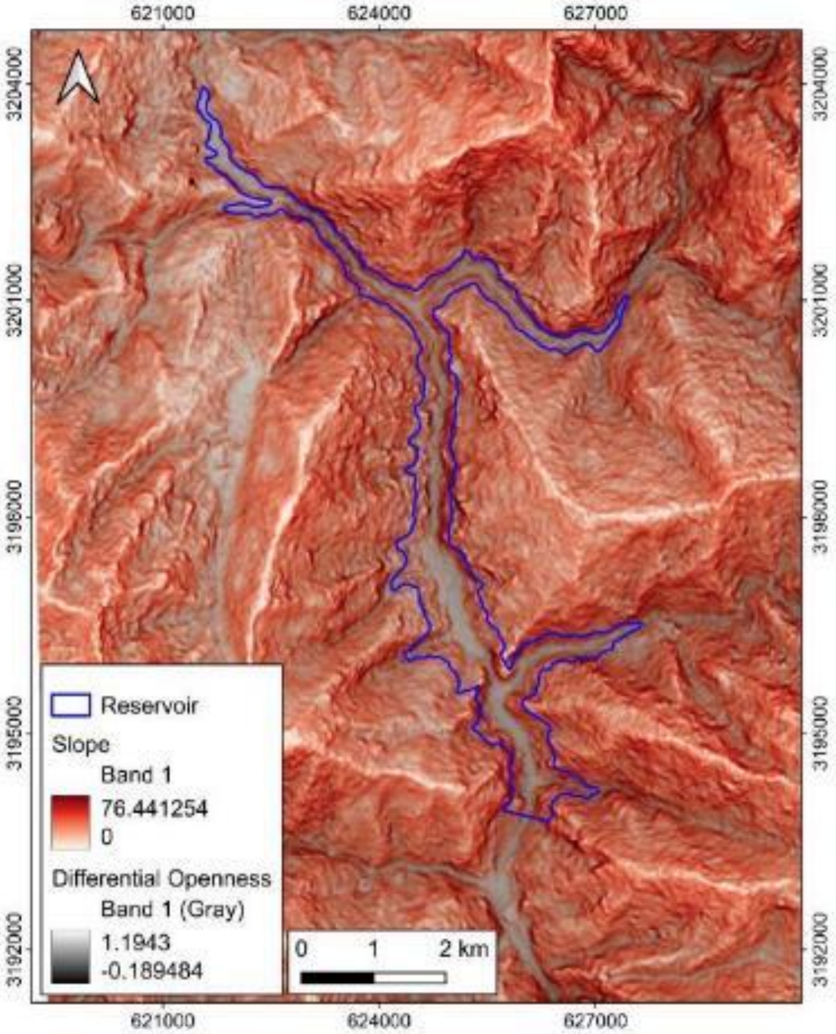

Figure Sup 39, Red Relief Image Map of Nalgad Storage Hydropower Project.

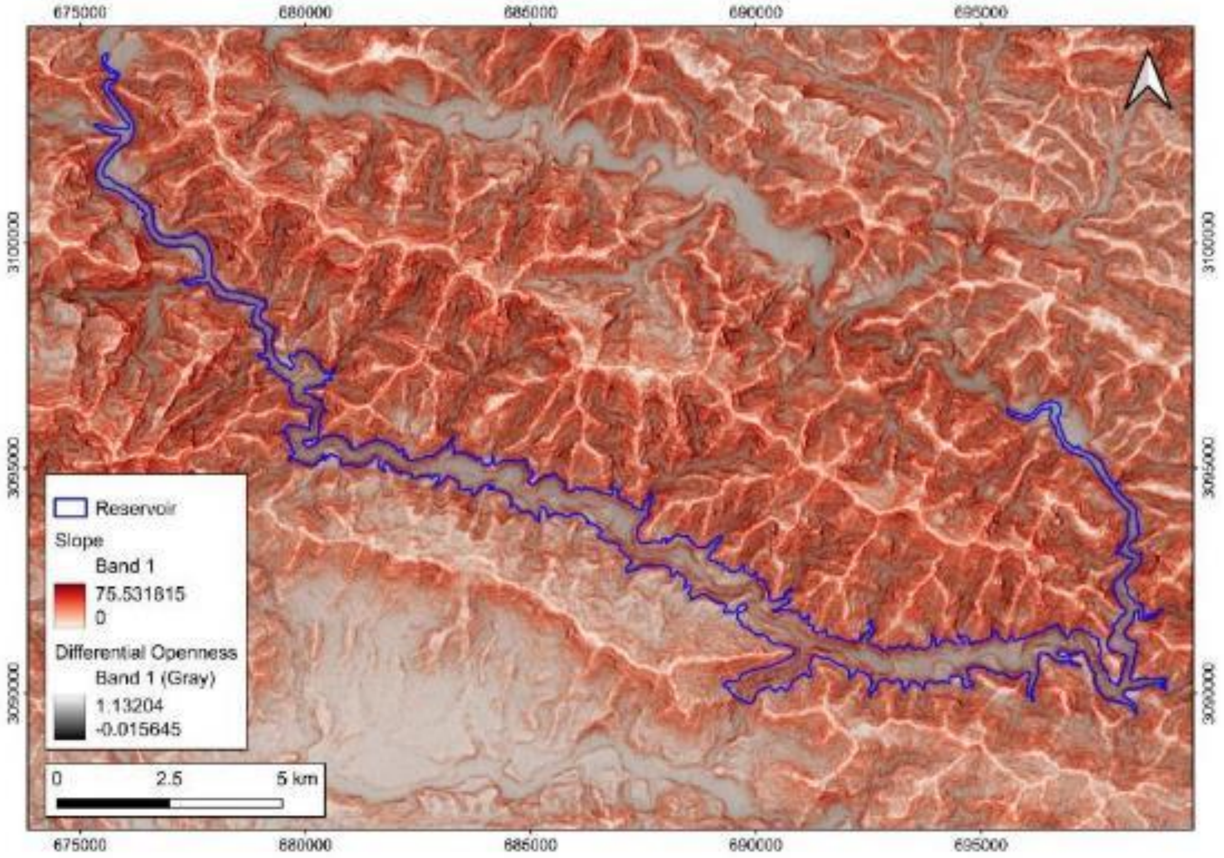

Figure Sup 40, Red Relief Image Map of Naumure Storage Hydropower Project.

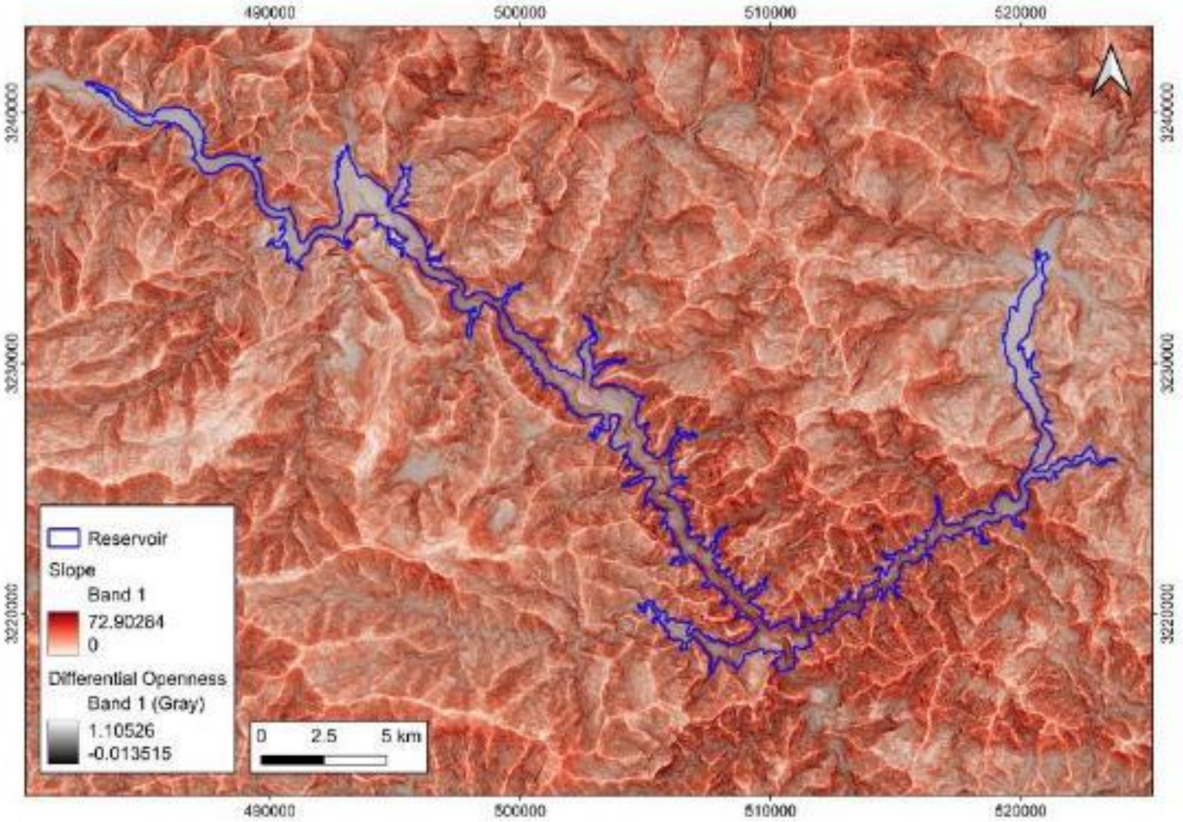

Figure Sup 41, Red Relief Image Map of SR-6 Storage Hydropower Project.

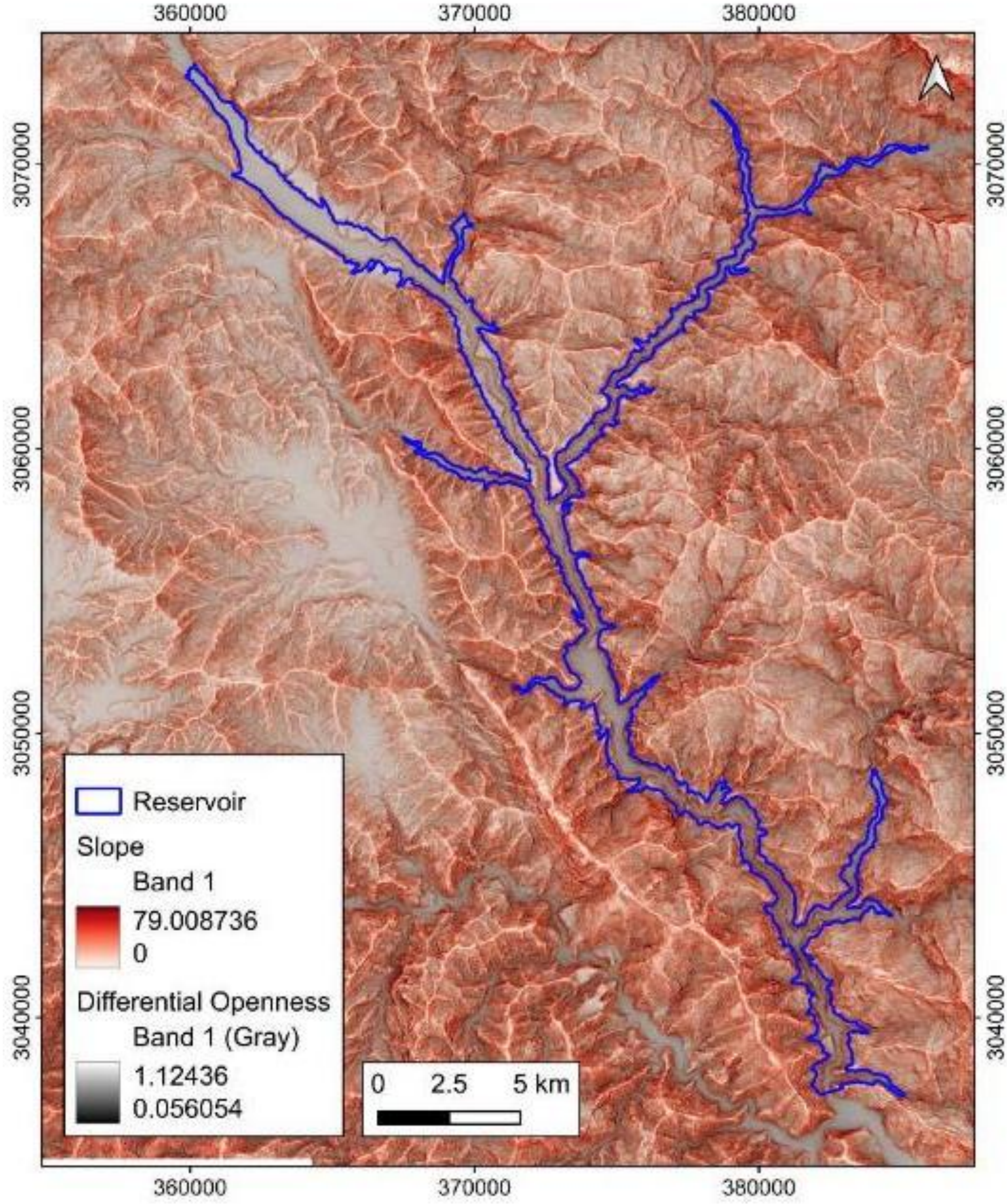

Figure Sup 42, Red Relief Image Map of Sun Koshi 3 Storage Hydropower Project.

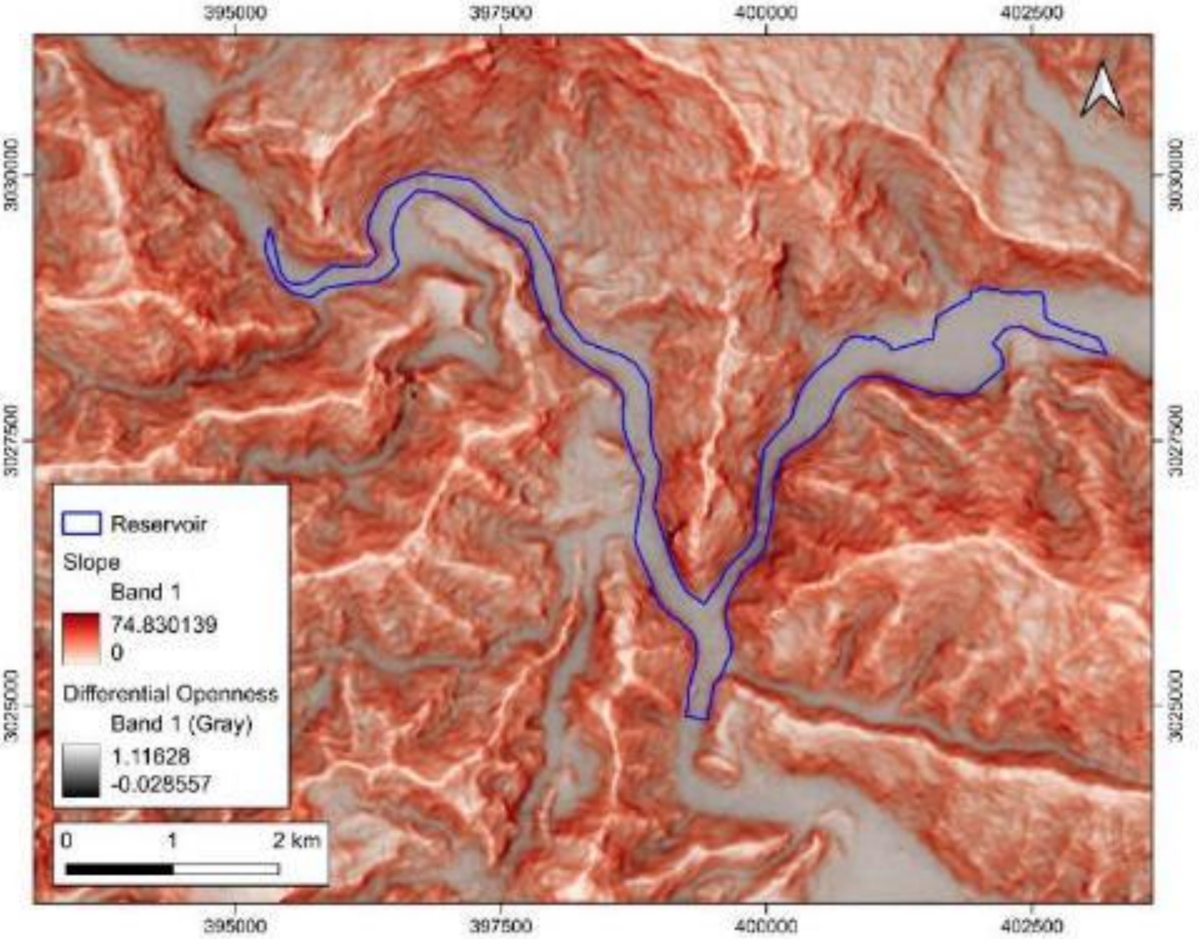

Figure Sup 43, *Red Relief Image Map of Sunkoshi Marin Diversion Multipurpose Project.*

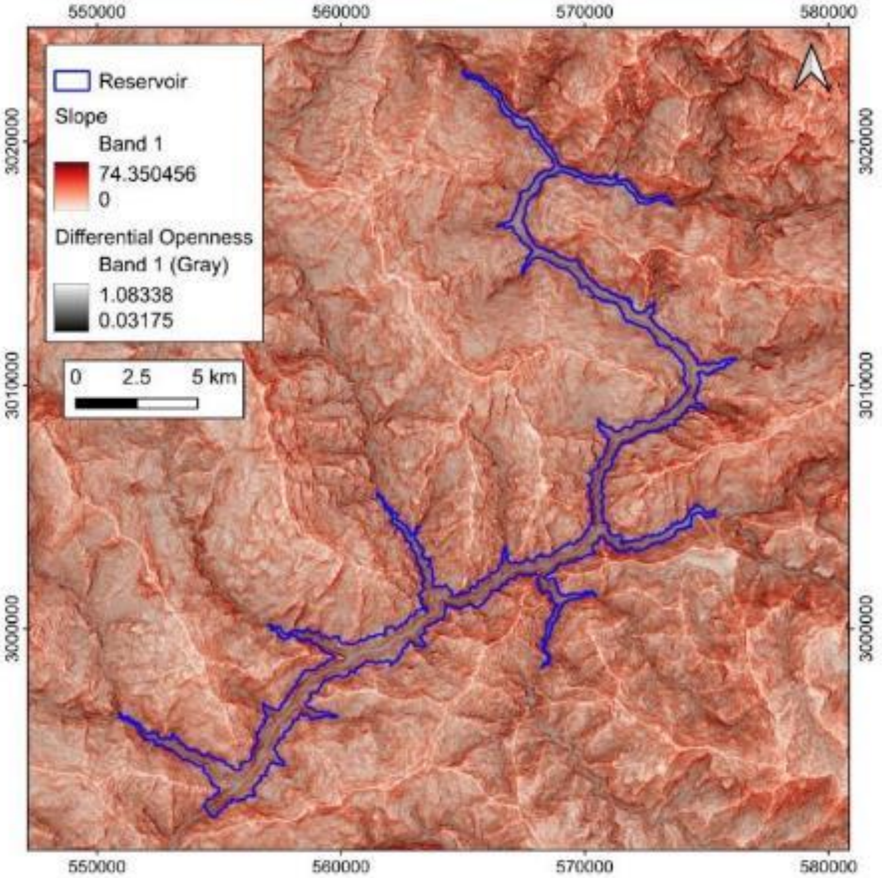

Figure Sup 44, *Red Relief Image Map of Tamor Storage Hydropower Project.*

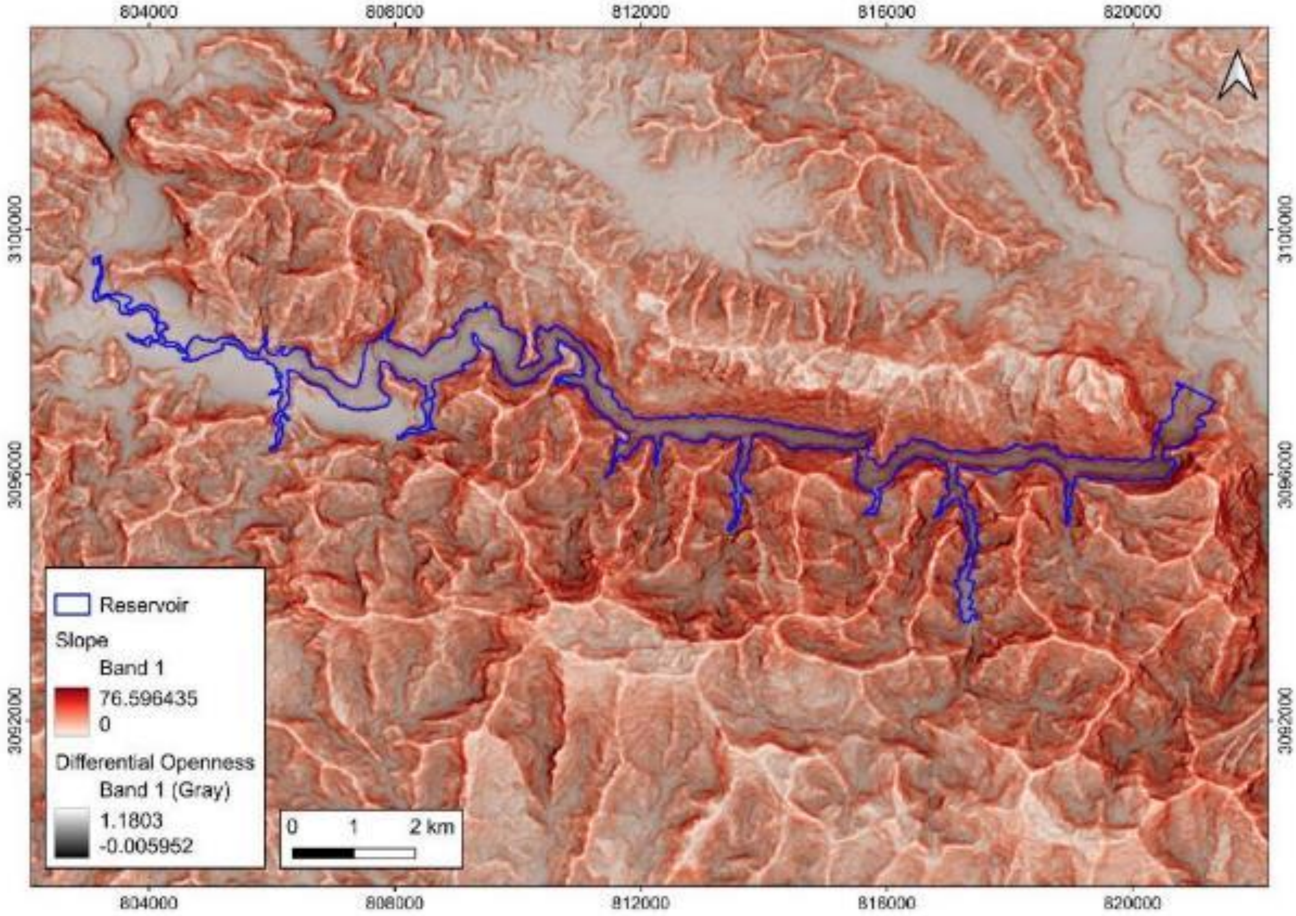

Figure Sup 45, Red Relief Image Map of Tanahu Hydropower Project (Upper Seti).

Asian Journal of Engineering Geology, 2024, Vol. 1 No. 1 and 2, 27-38

Research Article **DOI: https://doi.org/10.64862/ajeg.112.04** **Open Access**

Deformation Study of Gharkhola Hydroelectric Project Tunnel Emphasis on Squeezing, West Central Nepal

Mahendra Acharya[1]*, Kumar Timilsina[2], Ranjan Kumar Dahal[1]

[1]Central Department of Geology, Tribhuvan University, Kathmandu, Nepal
[2]Ghar Khola Hydroelectric Project, Myagdi, Nepal

*(*Corresponding E-mail: acharyamahendra.tu.edu.nep2019@gmail.com)*

Received: October 26, 2024, Accepted on December 18, 2024

Abstract: This research investigates the deformation and squeezing phenomena in the headrace tunnel of the Gharkhola Hydroelectric Project in Nepal, emphasizing the challenges posed by weak rock masses in the Himalayan region. The study employs a multifaceted methodology, integrating empirical, semi-analytical, and numerical approaches to evaluate the deformation modulus (Em) and predict tunnel stability. Utilizing regression analysis, the sensitivity of (Em) and predict tunnel stability. Utilizing regression analysis, the sensitivity of Em to rock mass classification Q, GSI, and RMR is scrutinized, revealing that equations proposed by Barton (2002), Hoek and Diederichs (2006), and Gokceoglu et al. (2003) exhibit the least sensitivity to rock mass variability, rendering them particularly efficacious for deformability estimation. The analysis identifies severe squeezing conditions in specific tunnel sections, with maximum wall closure reaching 0.432803 meters at an overburden height of 134 meters. Empirical and semi-analytical methods, including Singh et al. (1992) and Hoek and Marinos (2000), corroborate the prevalence of squeezing, while finite element modelling quantifies deformation, validating field observations. The study underscores the imperative of employing diverse methodologies to corroborate rock mass parameters, thereby enhancing the accuracy of squeezing predictions. The findings advocate for meticulous parameter selection and interdisciplinary validation to mitigate instability in tunneling projects within geologically complex terrains.

Keywords: ***Deformability, Squeezing, Support Pressure, numerical modeling.***

Introduction

In general, tunnel construction in hard rock can be taken as safe, and in weak rock, it is considered the most challenging based on the rock mass's mechanical behavior. In Himalayan countries like Nepal, Bhutan, and Northern parts of India there is good potential for waterpower generation tunnel construction is the most option given the economy and safety. Highly trustworthy rock mass qualities are necessary for the design and construction of rock tunnel structures, including support installation, safe excavation, and good performance (Hoek and Brown 1980a and Hoek and Diederichs 2006). In the complicated and fragile geological conditions, the occur several kinds of challenges to the underground works so, the rising risk of the excavations is managed by understanding the subsurface ground conditions, and understanding the stress conditions on the periphery of the excavation is the most necessary work.

The change in shape, size and structure resulting due to the stress is referred to as strain or deformation. Kayabasi et al. (2003) have shown that the deformation modulus is the most representative parameter of the pre-failure mechanical behavior of the rock material and a rock mass. Excavation in weak rock has greater stability problems, so the proper design of the underground openings is needed to consider the stress condition. The deformation modulus of a rock mass (Em) is one of the key parameters in rock engineering among the rock mass parameters. The design and successful completion of rock engineering projects depend heavily on the deformation modulus. In a tunnel, the anisotropic stress conditions generate problems like squeezing, rock bursting, and many stability-related problems (Selmer-Olsen and Broch, 19970). The instability in the tunnel that occurred in the weak rock is defined by the term squeezing. In this research, ground deformation is studied by details analysis of the discontinuity properties such as its pattern, block size, persistency, etc. Jaiswal et al. (2023) used a modeling technique to aid stress estimation and tunnel support evaluation for retards the problems that come in future development conducted by Mushahary et al. (2020). The direct evaluation of the tunnel squeezing is the most difficult task so using the several types of the empirical relationship given by the different researchers in the past using this empirical relation evaluation of the tunnel deformability was estimated.

A handful of the equations were based on the rock quality designation (RQD; Zhang and Einstein 2004), while the majority were based on the rock mass rating (RMR) as described by Bieniawski (1973), the tunneling quality index (Q; Barton et al. 1974), and the geological strength index (GSI). In this study, the RMR, GSI, and Q classification systems are used to estimate the deformation modulus values of the rock mass along the tunnel of the Gharkhola Hydroelectric Project using existing empirical equations. Squeezing will happen when a plastic zone forms around the tunnel, creating severe deformation in the tunnel's perimeter if the rock mass is very weak and malleable. Because of the fault zones and weak rocks (such as mudstone, shale, slate, phyllite, schist, and extremely schistose gneiss) that make up the mountains, tunnel squeezing is a frequent occurrence in the Himalayas (Panthi 2006).

Along the headrace tunnel of the Gharkhola Hydroelectric Project, excessive tunnel squeezing has taken place. The project management had substantial difficulties in battling the squeeze. In its research by utilizing intact rock properties and other index variables, the commercial computer application Roclab (Rocscience Ltd. 2011) is used to evaluate rock mass parameters. In addition to mechanical characteristics like rock mass strength, deformation modulus, and tensile strength, these rock mass qualities also contain strength factors like cohesion and friction angle (Hoek and Brown 1980 b). Tunnel squeezing analysis was carried out by using the commercially available software Phase 2 by using the different rock mass input parameters. It enables accurate modeling of an underground excavation where the rock exhibits plastic behavior close to the excavation and elastic behavior farther away from the excavation (Khadka et al., 2019). In this research work, the Gharkhola Hydroelectric Project is selected for this study. The main aim of this research is to study the sensitivity of the deformability equations and to identify the tunnel's stability conditions.

Study Area

Geological study area lies in the Lesser Himalaya of Nepal Himalaya at Myagdi district is located in western Nepal, which is part of Gandaki province (Figure 1). The district lies at latitude 28° 20’ 32.49” N and longitude 83° 33’ 57.78” E and has a maximum altitude is 8, 167 m (Dhaulagiri Himal) and a minimum altitude is 792 m (Ratnechaur). The district is surrounded by Mustang, Manang, Kaski, Parbat, Baglung, Rukum, and Dolpa districts. The location of the study area (Figure 1) is 304 km away from Kathmandu Valley towards the west. The study project lies at Annapurna Rural Municipality wards no. 5 and 6. The project is a run-of-river type project. The geographic coordinates of the study project are latitude 28° 27’ 02.53” and longitude 83° 39’ 53.36”. The region is a part of the Lower Nuwakot Group of the Lesser Himalaya geologically. It mostly consists of the white quartzite from the Fagfog Quartzite and the green phyllite from the Kuncha Formation, respectively. The foliation then dips moderately to steeply between 26° and 49° towards the north, with a NW-SE strike.

Geology of the project area

Geologically, the area lies in the Lesser Himalaya (Lower Nuwakot Group) region. Which dominantly consists of the green phyllite and white color quartzite of the Kuncha Formation and Fagfog Quartzite respectively. Along the tunnel alignment, phyllite with amphibolite bands and Quartzite were present as the dominant rock types. Then the foliation strikes NW-SE with moderate to steep dipping about 26°-49° towards the north.

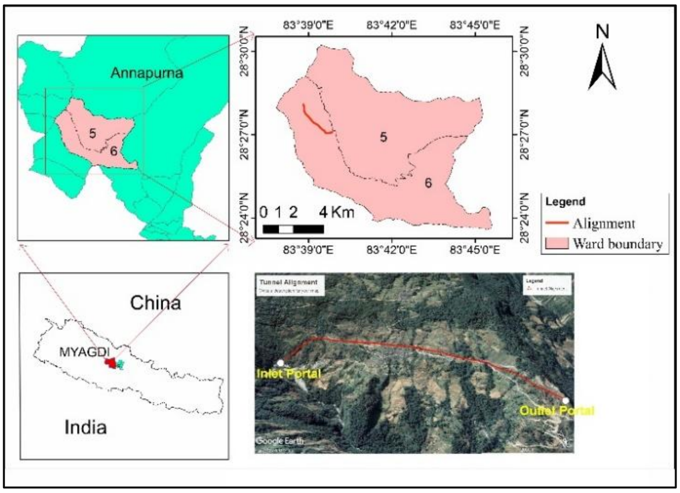

Figure 1, Location map of the study area.

Methodology

With that several methodologies were used to assess the different rock mass properties. The details of the methodology are discussed below.

Calculation of deformation modulus

There exist different types of equations which were derived from the regression analysis. In this study, Q, RMR, and GSI are used to estimate the deformation modulus value along the tunnel alignment. The deformation modulus value is calculated by the equation proposed by Barton (1995), Palmström, and Singh (2001), Barton (2002), and Grimstand and Barton (1993).

Barton (2002):

$$\mathrm{Em\ (Gpa)} = 10 \times \left(\mathrm{Q} \times \frac{\sigma c}{100}\right)1/3 \tag{1}$$

Barton (1983)

$$\mathrm{Em\ (Gpa)} = 10 \log \mathrm{Q}\ \text{(Minimum)} \tag{2}$$

Palmström and Singh (2001):

$$\mathrm{Em(Gpa)} = 8\mathrm{Q}^{0.4} \tag{3}$$

Grimastad and Barton (1993);

$$\mathrm{Em\ (Gpa)} = 25 \log \mathrm{Q}\ \ \text{(Average)} \tag{4}$$

$$\mathrm{Em\ (Gpa)} = 40 \times \log \mathrm{Q}\ \text{(Maximum)} \tag{5}$$

Then, the deformation modulus using GSI along the tunnel alignment the equation proposed by Hoek and Brown (1997), Carvalho (2004), Hoek and Diederichs (2006) and Beiki et al. (2010).

Using Beiki et al. (2010):

$$\mathrm{Em} = [\tan\,(1.56\ +\ (\ln\,(\mathrm{GSI}))\hat{}2]0.5 \times (\sigma_{ci})1/3 \tag{6}$$

Using Hoek and Diederichs (2006):

$$\mathrm{Em} = \left[\frac{10^5(1-0.5\mathrm{D})}{1+\mathrm{e}^{\left(\frac{(75+25\mathrm{D}-\mathrm{GSI})}{11}\right)}}\right] \quad (7)$$

Hoek and Diederichs (2006) using Ei:

$$\mathrm{Em} = \mathrm{Ei}\left[\frac{0.02+(1-0.5\mathrm{D})}{1+\mathrm{e}^{\left(\frac{60+15\mathrm{D}-\mathrm{GSI}}{11}\right)}}\right] \quad (8)$$

Using Hoek and Brown (1997):

$$\mathrm{Em} = \left(\frac{\sigma\mathrm{ci}}{100}\right)^{0.5} \times 10\left(\frac{\mathrm{GSI}-10}{40}\right) \quad (9)$$

Using Carvalho (2004):

$$\mathrm{Em} = \mathrm{Ei}(s)^{0.25}, \mathrm{S} = \mathrm{Exp}\left(\frac{\mathrm{GSI}-10}{9-3\mathrm{D}}\right) \quad (10)$$

Similarly, the deformation modulus using RMR along the tunnel alignment the equation proposed by Gokceoglu et al. (2003), Diederichs and Kaiser (1999), Mitri et al. (1994) and Serafim and Pereira (1983).

Using Gokceoglu et al. (2003):

$$\mathrm{Em} = 0.07555\ \mathrm{RMR} \quad (11)$$

Using Diederichs and Kaiser (1999):

$$\mathrm{Em} = \sqrt[7]{10^{(\mathrm{RMR}-44)/21}} \quad (12)$$

Using Mitri et al. (1994;

$$Em = 0.1\left(\frac{RMR}{100}\right)3 \quad (13)$$

Using Serafim and Pereira (1983):

$$Em = 10^{\left(\frac{RMR-10}{40}\right))} \quad (14)$$

Tunnel squeezing analysis

In its research, the different 51 sections of the tunnel were taken based on the problems that arose in the tunnel after the excavation, and the rock mass conditions existing tunnel. In its research, the following approaches were used to study the tunnel squeezing phenomenon.

Empirical approaches

Semi-analytical approaches

Numerical modeling approaches

Empirical approaches

Rock mass classification approach

Rock mass classification approaches in tunnel squeezing analysis Singh et al. 1992, and Goel et al. 1995, were used in this research.

Singh et al approach (1992)

Singh et al. 1992 give a clear demarcation line to find out the squeezing and non-squeezing conditions. In its research total of 51 sections of the tunnel, data is collected to delineate whether the squeezing or not by using the Singh et al. concept and to compare the analysis ground condition and real field condition. The following relationships were used for this.

The equation of a line

$$\mathrm{H} = 350\ \mathrm{Q}^{1/3}\ (\mathrm{m}) \quad (15)$$

The compressive strength of the rock mass was calculated by using a relation.

$\sigma\mathrm{cm} = 0.7\ \gamma\ \mathrm{Q}^{1/3}$Mpa) (H= Overburden height) (16)

Goel et al. (1995) approach

Goel et al. 1995 give an empirical approach to estimating the stability of tunnels based on rock mass number N, depth of overburden H, and tunnel diameter. In its research, the different tunnel section data were taken from the Gharkhola Hydroelectric Project to study the stability and squeezing conditions in the tunnel. The data were calculated using the empirical relationship given by Goel et al. (1995) and a graphical plot was carried out as per the Goel et al. standard.

$$\mathrm{H} = (275\mathrm{N}^{0.33})\mathrm{B}^{-0.1} \quad (17)$$

In which n rock mass number, B = Tunnel diameter, and H = Overburden height.

Semi-analytical approach

The Hoek and Marinos (2000) approach were used as the semi-analytical approach to find the tunnel squeezing. This approach is generally used to evaluate the deformation initiated by squeezing and similarly the determination of support pressure by taking the different data related to tunnel support. As per Hoek and Marinos the tunnel strain value plot against the σ_{cm}/P_o used to evaluate the tunneling issues.

The Hoek and Marinos curve obey the following relationship.

$$\varepsilon = \frac{\delta_i}{d_o} = \left[0.002 - 0.0025\ \frac{P_i}{P_o}\right]\left(\frac{\sigma_{cm}}{P_o}\right) \wedge \left(2.4\ \frac{P_i}{P_o} - 2\right) \quad (18)$$

For the unsupported condition in the above equation, Pi is zero. Then the compressive strength of the rock was calculated by using the following relation.

$$\sigma_{cm} = (0.0034 m_i^{0.8})\ \sigma_{ci}\{1.029 + 0.025\ e^{(-0.1 m_i)}\}\ GSI \quad (19)$$

Where,

GSI =Geological Strength Index,

m_i = material constant,

σ_{cm} = Compressive strength of rock mass,

P_i = Internal support pressure,

P_o = In-situ stress,

ε = Tunnel strain,

σ_{ci} =Intact rock strength

In its research, the above-mentioned relationship is used to calculate the tunnel strain, and this is interpreted as per Hoek and Marino's standard to find out the types of squeezing in the tunnel section.

Numerical modelling approaches

There exists several numerical modeling software then in this study Phase2 software was used for the different analyses. Phase2 is a two-dimensional modeling software that can be used to display the different stability conditions of the rock mass in an underground structure. Phase2 is one of the most familiar modeling software which calculates stress and can add different support structure designs for the underground structure. It uses the two-dimensional finite element method to encircle the opening and extend past the boundary element interface due to automatic generation in the pre-processor. The most common numerical techniques for designing tunnels and subterranean excavations in rock engineering were illustrated by Barla (2016).

Rocscience software is a finite element analysis application that has been used in this study by calculating the required parameters and techniques developed by Hoek and Brown (1997). The growing trend of the rock mass's failure and the support's reaction could be observed in Phase2 over several of the excavation's subsequent phases.

Results

Geology of headrace tunnel alignment

Geologically, the area lies in the Lesser Himalaya (Lower Nuwakot Group) region. Which dominantly consists of the green phyllite and white color quartzite of the Kuncha Formation and Fagfog Quartzite respectively. Along the tunnel alignment, phyllite with amphibolite bands and Quartzite were present as the dominant rock types. Then the foliation strikes NW-SE with moderate to steep dipping about 26^0-49^0 towards the north. The geological cross-section of the tunnel study section is shown below (Figure 3). The Main Central Thrust is the major tectonic structure that separates the Lesser Himalaya rocks from the Higher Himalaya rocks sequences. In the study area, the MCT lies about 3.6 km upstream of the project site near Dana. In the project area, a few centimeters to a few meters thick shear zones were found which are characterized by crenulation, weak to highly soft materials presence, and bright grey to green clay gouge with the presence of illite and chlorite.

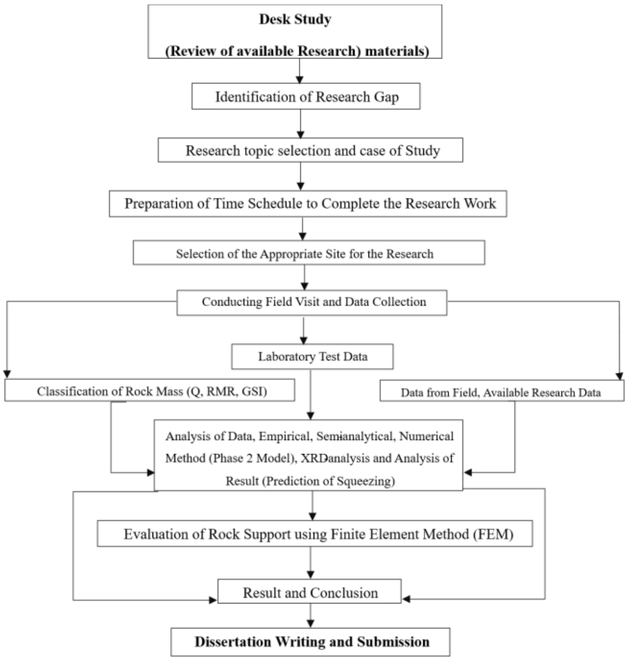

Figure 2, Methodological flowchart of the research work.

Tunnel deformability study

The different available empirical relations to calculate the deformation modulus of them deformation modulus using Q, GSI, and RMR were used for the study.

Deformation modulus using Q-method

Using this Q method the deformation modulus was calculated by using the empirical relationship given by Grimstad and Barton 1993, Palmström and Singh 2001, and Barton 1995. Due to the low value (<1) of Q some applied relations do not give an adequate result. Then the graphical plot of the deformation modulus from different empirical relations along the selected chainage is shown below (Figure 4). According to the chainage of each type of rock, the observed Em values for the relationships indicated above were plotted on a graph. The average, minimum, and maximum Em values for various rock types along the tunnel are displayed in Figure 3 below. Values are derived from Q.

From the above graphical plot (Figure 3) the different values of the deformation modulus were plotted and compared with each other. Among the three applicable empirical relations (i.e. Barton 1995, Palmström and Singh 2001 and Barton 2002) the sensitivity of the different empirical relations was checked with rock mass type and rock class. In them, Barton 2002 seems less sensitive than Barton (1995) and Palmström and Singh (2001).

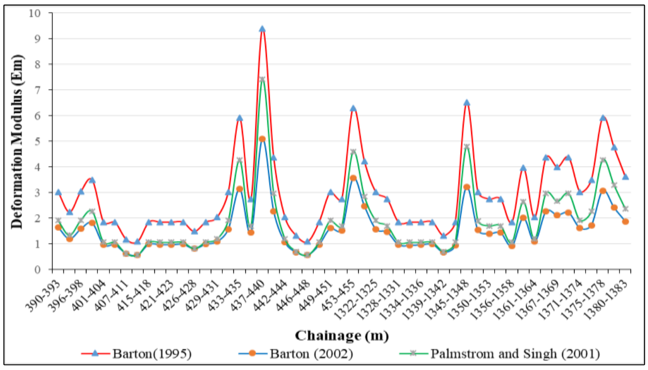

Figure 3, Comparison of deformability value using different empirical methods using Q.

Deformation modulus using GSI

Similarly, the deformation modulus of rock mass using GSI was also calculated using the different empirical relationships given by rock science researchers. Based on GSI the empirical relation given by Hoek and Brown (1997), Carvalho (2004), Hoek and Diderichs (2006), Beiki et al. (2010) and Hoek and Diderichs (2006) using Ei were used in its research. Then obtained value of the deformation modulus using different empirical relationships was compared by Plotting them (Figure 4). From this plot, Hoek and Diederichs using Ei seem less sensitive to change in rock class and rock mass type than the other empirical relation to calculating the deformation modulus. So, Hoek and Diederichs give a more satisfactory result compared to other methods.

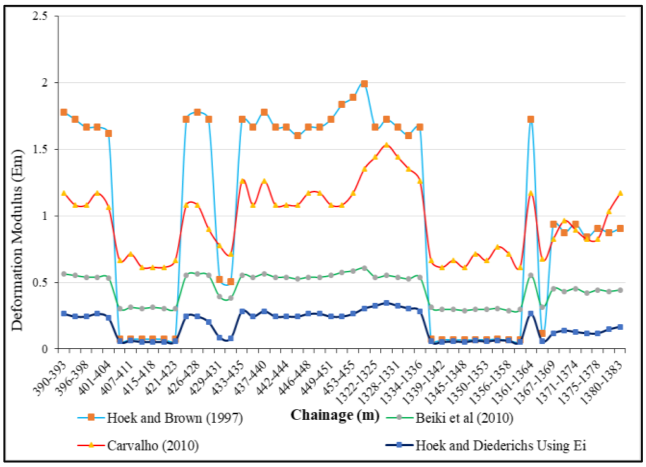

Figure 4, Comparison of deformation modulus from the empirical relationship using GSI.

Deformation modulus using RMR

Similarly, deformation modulus using RMR values were also used to calculate the deformation modulus of the rock mass. Different empirical relationships were used i.e. Serafim and Pereira 1983, Mitri et al. 1994, Diderichs and Kaiser 1999, Gokceoglu et al. 2003, and Palmström and Singh 2001. From this study (Figure 5), Gokceoglu et al. 2003 seems less sensitive to changes in rock mass types and class than the other equation used to estimate Em. So, it gives more satisfactory results than others.

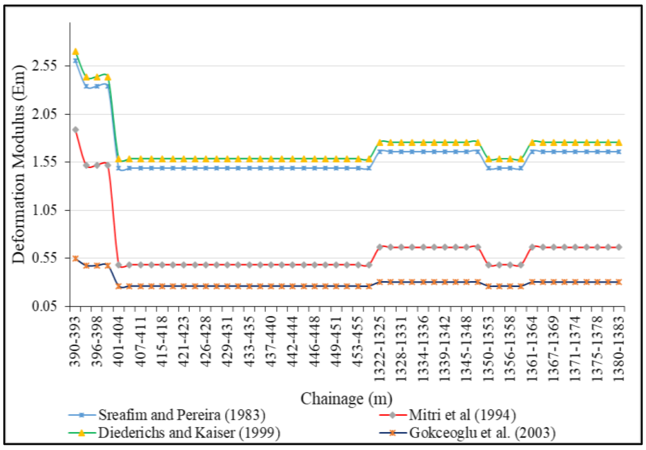

Figure 5, Comparison of deformation modulus values calculated using GSI.

Tunnel squeezing analysis

At locations where the squeezing issue was apparent, the tunnel's deformation was measured. Neither throughout the research period nor when the excavation was taking place were any tests on the parameters related to rock mass taken. Face mapping of the tunnel involved estimating the Q-value and recording the rock and support types. Other factors, such as the complete rock's unconfined compressive strength, Young's modulus, density, and Poisson's ratio, were not examined in the lab. So, all these required parameters were taken from the literature review based on the ground condition in field. In its research, the following approaches were used to study the tunnel squeezing phenomenon.

- Empirical approaches
- Semi-analytical approaches
- Numerical modeling approaches.

Empirical approaches

In its research work, rock mass classification approaches were used.

Rock mass classification approach

To predict tunnel squeeze, the rock mass classification approach was given in the past by different researchers. In this research, the following approaches were used to predict tunnel squeezing.

Singh et al. approach (1992)

In the past, Singh et al. gave the concept of finding out the ground condition and whether squeezing occurred or not. In which they take the different tunnel data and develop the standard graphical plot to delineate the squeezing ground conditions. They give a clear demarcation line to differentiate whether the ground is squeezing or not. Then the Q value and Height of the overburden were collected. In its study from the graphical plot of the study section (Figure 6) based on rock mass quality Q value of different selected sections of the tunnel, it seems 10% of the area of the tunnel section lies under the non-squeezing zone and 90 % of the area lies under the squeezing zone. The chainage 0+390, 0+396, 0+398, 0+433, and 0+437 lies under the non-squeezing zone which has overburden heights are 133 m, 132 m, 132 m, 142 m, and 143 m respectively. Then the remaining chainage lies under the squeezing zone.

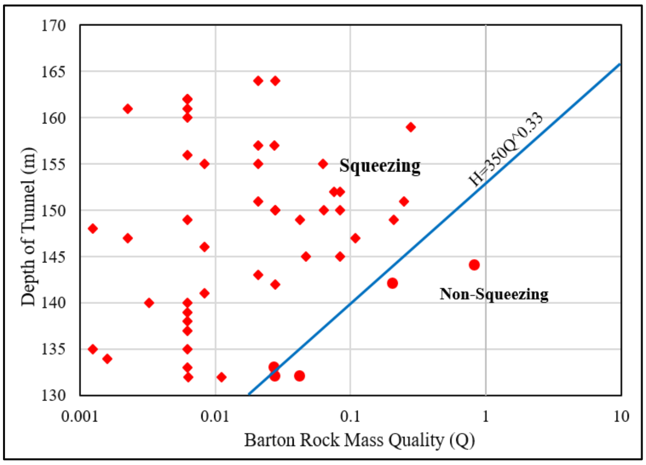

Figure 6, Prediction of the ground condition based on Q.

Goel approach (1994)

The rock mass number N which is referred to as Q with stress reduction factor (SRF) =1 was used by Goel (1994) to build an empirical method. N value was utilized to get around issues and uncertainties in the Q method's ability to rate the parameter stress reduction factor correctly. In its research, we have plotted the information that is currently available in log-log diagrams between N and HB0.1 considering the rock mass number N, depth of overburden H, and tunnel diameter B from the study tunnel. All the selected sections of the tunnel were plotted on the graph given by Goel to delineate whether the ground squeezing or not. A clear demarcation of lines separates this condition.

From the graphical plot, there seems that 41% of the area lies under the severe squeezing area, and about 59% fall under the minor squeezing zone. This result seems more closely related to the ground conditions in the real field.

Semi-analytical approach

Among these different semi-analytical methods, Hoek and Marinos 2000 were used in their research.

Hoek and Marinos 2000 approach

Hoek and Marinos's (2000) squeezing analysis method was applied to the semi-analytical method scenario with correlation to ground conditions. Using various parameters including the intact rock strength, material constant, depth of overburden Geological Strength Index (GSI), rock mass compressive strength, intact rock strength, and support pressure the tunnel strain was computed. The support employed in the tunnel like rock bolts, steel ribs, and shotcrete were used to calculate the tunnel support pressure P_i. Then the tunnel strain P_{imax} was computed using the P_i value that was determined. In its research in the selected tunnel section, the support was installed so using the Hoek and Marinos concept is better for the evaluation of the tunnel squeezing. To allow the internal support pressure in the tunnel the semi-analytical approach is best. In its research majority of the tunnel sections selected fall inside the < 1% tunnel strain. This means there are few support problems in the tunnel rather than the tunnel squeezing. Some sections fall inside the 1 to 2.5 % which means minor support problems. Then very few sections of the selected section tunnel fall inside the 2.5 to 5% which means the severe types of squeezing. Then the graphical plot of the tunnel strain at zero support pressure condition is shown below (Figure 8).

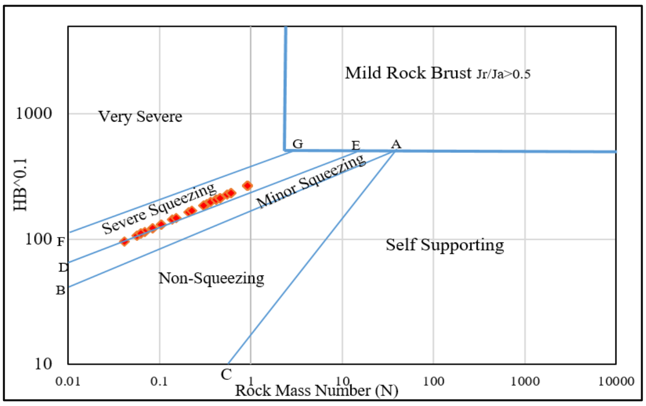

Figure 7, Prediction of the ground using rock mass number N.

In the study project at the selected tunnel section, the support was installed so, using this Hoek and Marinos concept the value of the internal support pressure is calculated to find the tunnel strain after the support installation in the tunnel. So, to calculate the internal support pressure (P_{imax}) in the tunnel by considering the different supports used in the tunnel. Then from the calculation, the value of P_{imax} is 2.5 for the whole selected tunnel section. Then, the value of the tunnel strain ranges from 0.002 to 3.40 %. Then the comparison between the tunnel strain at conditions of with support and without support is shown below (Figure 8).

This shows that the support helped to control the tunnel failure at a certain point and then further after support installed there still the tunnel strain value is higher in some sections which indicates there is also some defect in the support used and in ground conditions. At chainage 0+407, 0+446, 1+334, and 1+356 there seems to squeeze problem in the field and the calculations. Then the final tunnel strain value is calculated by using the effective value of support pressure. From the Hoek and Marinos (2000) analysis of tunnel squeezing at the different sections of the tunnel different problems of squeezing were found such as few support problems, Minor squeezing problems, and severe squeezing problems (Table 1). The result obtained from this analysis seems more appropriate than the other method of tunnel squeezing prediction with ground conditions.

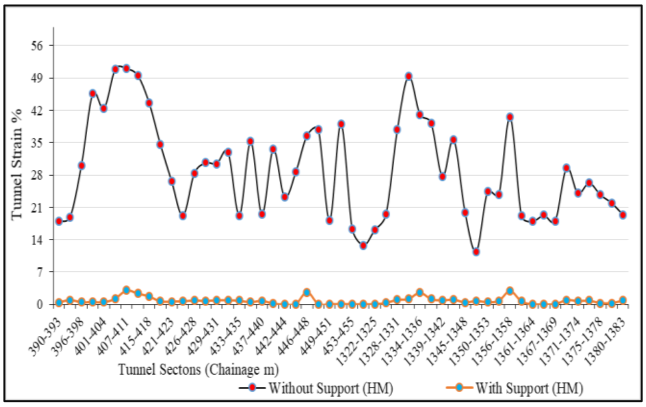

Figure 8, Comparison of the tunnel strain without the support and with support.

Numerical modelling approach

In its research work, generally Phase 2 software was used for tunnel deformation modeling. Based on the tunnel squeezing condition or based on tunnel strain value the different tunnel sections on which high squeezing occurs were selected for the modeling of tunnel deformation. The chainage 0+407 m, 0+446 m, and 1+334 m were selected for the deformation analysis on which maximum squeezing occurred.

Chainage 0+407: The excavated rock mass consists of thinly foliated, slightly to highly weathered, dark grey to black phyllite (pelitic) with little quartz veins. The existing rock mass is highly deformed and crushed, and the joints are low to medium spacing, with a medium persistence of >1m. Slightly weathered, smooth. Then the excavated rock mass of the left wall below the sp level is highly sheared and deformed in conditions. But the right wall seems slightly better than the left wall of the tunnel. Then the details of the rock mass parameter used in this modeling are shown below (Table 2).

The parameter was used in the numerical modelling of tunnel deformation, then the result observed is shown below (Figure 9, Figure 10, Figure 11 and Figure 12).

Using the finite element method several ground conditions were modeled, and the results are shown as deformation behavior under the different low to medium stress conditions. In this study, overburden mass seems to correspond to the highest and lowest stress level range.

Table 1, Tunnel strain and types of problems at selected section of Tunnel.

Chainage (m)	Tunnel Strain (ε%)	Remarks
390 to 404	0.45 – 0.95	Few support problems
404 to 407	1.27	Minor squeezing problems
407 to 411	3.04	Severe squeezing problems
411 to 415	1.74	Minor squeezing problems
415 to 446	0.02 to 0.93	Few support problems
446 to 448	2.66	Severe squeezing problems
448 to 458	0.01 to 0.07	Few support problems
1322 to 1331	0.06 to 0.94	Few support problems
1331 to 1334	1.18	Minor squeezing problems
1334 to 1336	2.56	Severe squeezing problems
1336 to 1339	1.15	Minor squeezing problems
1339 to 1356	0.49 to 0.97	Few support problems
1356 to 1358	2.51	Severe squeezing problems
1358 to 1383	0.02 to 0.96	Few support problems

Table 2, Rock mass input parameter for chainage 0+407.

Parameter type	Rock mass (sheared)		Rock (mass sound)	
	Peak	Residual	Peak	Residual
Types of rock	Phyllite (Pelitic)		Phyllite (Pelitic)	
UCS (Mpa)	13		20	
Unit weight (KN/m^3)	26		26	
GSI	6	6	16	16
m_i	7	7	7	7
D	0	0.5	0	0.5
m_b	0.235	0.0759	0.3362	0.12224
S	2.60e-0	3.15e-006	7.91e-00	1.19e-00
A	0.612	0.61921	0.56110	0.561101
Poisson ratio (θ)	0.2	0.2	0.2	0.2

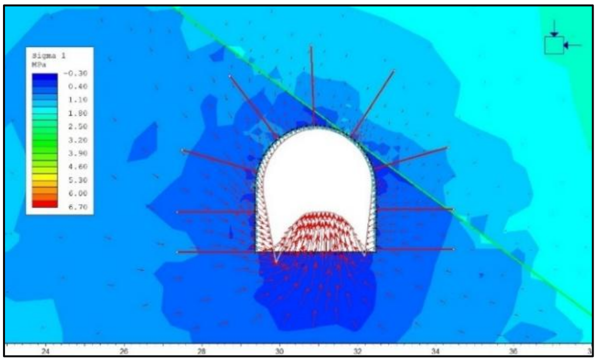

Figure 9, The principle stress (σ_1) applied Ch. 0+407 m

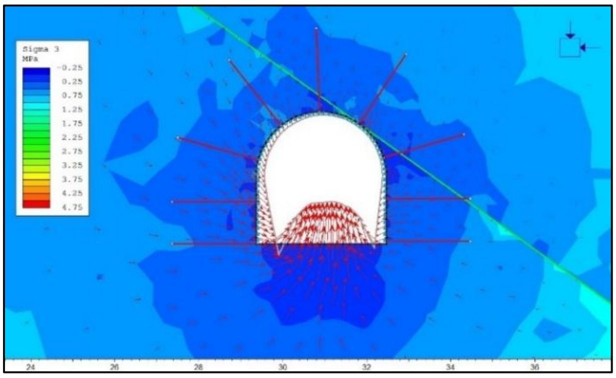

Figure 10, The principal stress (σ_3) applied at Ch. 0+407 m

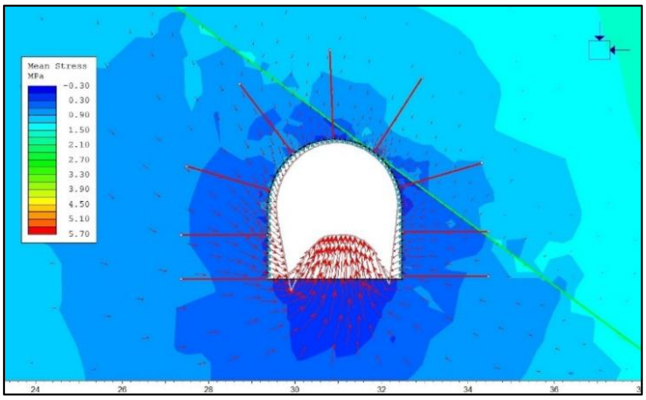

Figure 11, The mean stress applied at Ch. 0+407 m

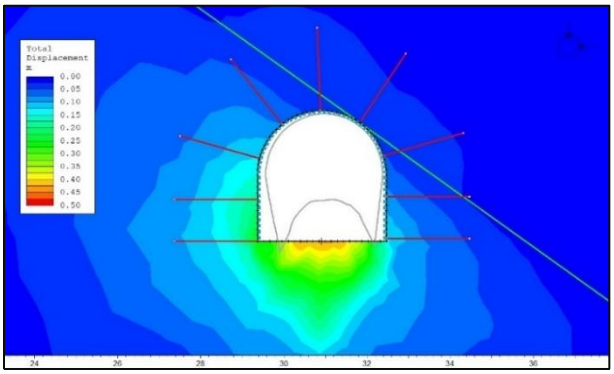

Figure 12, Tunnel deformation boundary at ch. 0+407 m

Finally, in this section, the value of the total maximum displacement obtained is 0.432803 m. Chainage 0+446: The rock mass consists of thinly foliated, slightly to high weathering dark grey to black phyllite (pelitic) with branching quartz veins. The rock mass is highly deformed and crushed phyllite. J1 is low to medium spacing, medium persistence of >1m, slightly weathered, and smooth to the rough planar surface. Other crushed joints are low to medium persistence, and slightly weathered conditions. The excavated rock mass of the right wall below the sp level is lightly shared and deformed in conditions. Most of the properties of the rock mass are like the rock mass condition of chainage 0+407 m. The details of the rock mass parameter used in the modeling are shown in the table below (Table 3).

Table 3, Rock mass input parameter for chainage 0+446 m.

Parameter type	Rock mass (sheared)		Rock (mass sound)	
	Peak	Residual	Peak	Residual
Types of rock	Phyllite (Pelitic)		Phyllite (Pelitic)	
UCS (Mpa)	14		21	
Unit weight (kN/m3)	26		26	
GSI	7	7	18	7
mi	7	7	7	7
D	0	0.5	0	0
mb	0.0796	0.09637	0.37431	0.079637
s	3.60e-0	3.64e-006	0.00011	3.6045e-00
a	0.61151	0.611508	0.54999	0.611508
θ	0.2	0.2	0.2	0.2

The above-tabulated parameter was used in the numerical modelling of tunnel deformation then the result observed is shown in Figures 13, 14, 15, 16. Using the finite element method several ground conditions were modeled, and the results are shown as deformation behavior under the different low to medium stress conditions. In this study, overburden mass seems to correspond to the highest and lowest stress level range. The different above-mentioned rock mass parameters of them are collected from the literature review like ground condition, some of them were taken from the project site office and some were from the field measurement and test. In this section, the value of the total maximum displacement obtained is 0.200786 m.

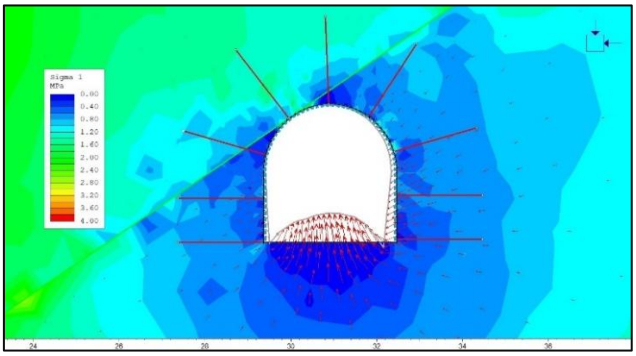

Figure 13, the principle stress (σ_1) applied Ch. 0+446 m

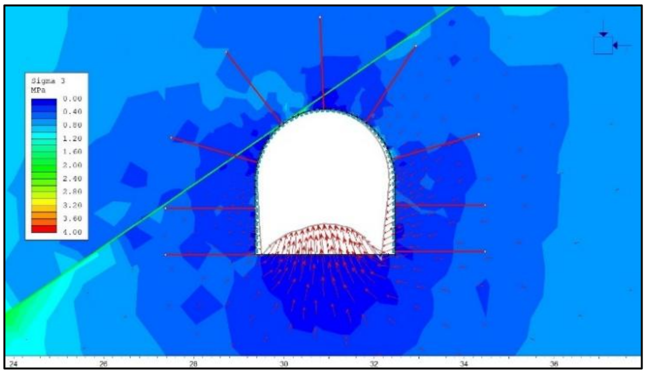

Figure 14, the principle stress (σ_3) applied Ch. 0+446 m

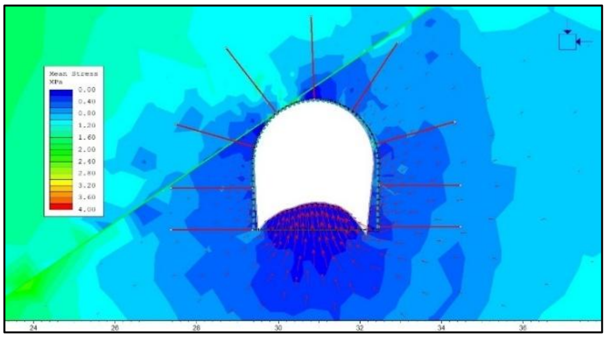

Figure 15, the mean stress applied at Ch. 0+448 m

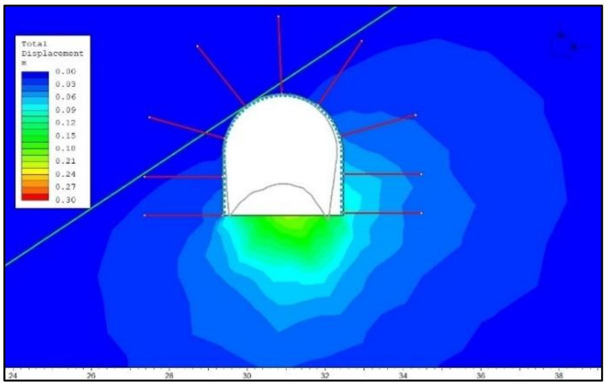

Figure 16, The deformation contour at Ch. 0+446 m

Chainage 1+334: The rock mass excavated consists of thinly foliated, mildly to heavily worn dark grey to black phyllite (pelitic) with extensively branching quartz veins, which makes up the excavated rock mass. The rock mass is severely crushed and distorted and J1 has low to medium spacing and persistence of more than 1 m, lightly worn, open joint, smooth planar surface, and J2 and J3 with low persistence (<1 m). The Rock mass is damp to little dripping in conditions. In its study, this section does not seem much of a drastic variation in the properties of the materials between the left and the right wall of the tunnel section. So, in the modeling of the deformation of the tunnel the same properties were used in both walls of the tunnel. The summary of the rock mass input parameter for the modeling is given below (Table 4).

Table 4, Rock mass input parameter for chainage 1+334 m.

Parameter type	Rock mass (sheared)	
	Peak	Residual
Types of rock	Phyllite (Pelitic)	
UCS (Mpa)	14	
Unit weight (kN/m3)	26	
GSI	11	11
mi	7	7
D	0.5	0.5
mb	0.101045	0.325358
s	7.0206e-006	2.93922e-00
a	0.579839	0.523561
Poisson ratio (θ)	0.2	0.2

The above-tabulated parameter was used in the numerical modelling of tunnel deformation then the result observed is shown below (Figures 17, 18, 19, 20). Using the finite element method several ground conditions were modeled, and the results are shown as deformation behavior under the different low to medium stress conditions. In this study, overburden mass seems to correspond to the highest and lowest stress level range. The different above-mentioned rock mass parameters of them are collected from the literature review like ground condition, some of them were taken from the project site office and some were from the field measurement and test.

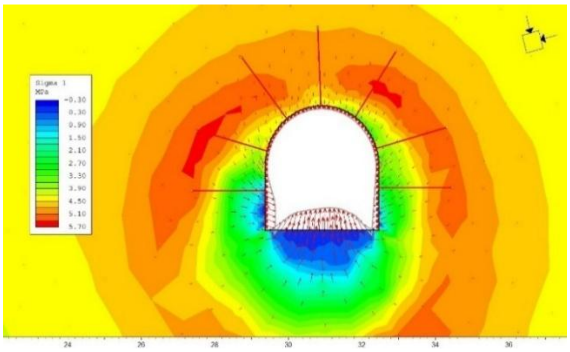

Figure 17, The principal stress (σ_1) applied at Ch.1+334 m

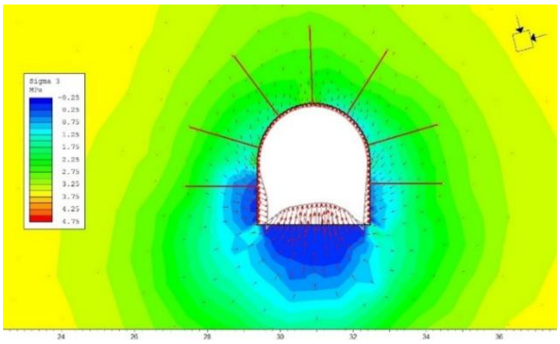

Figure 18, The principal stress (σ_3) applied at Ch. 1+334 m

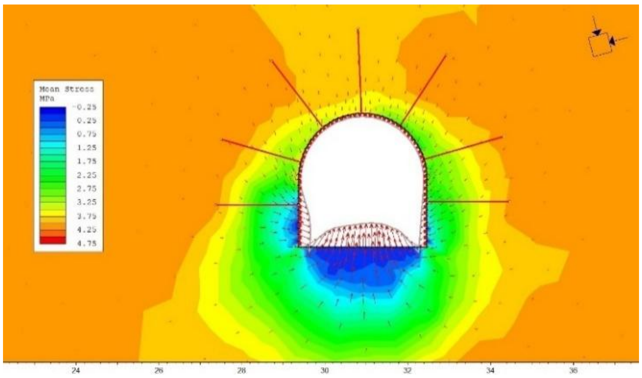

Figure 19, The mean stress applied at Ch. 1+336 m

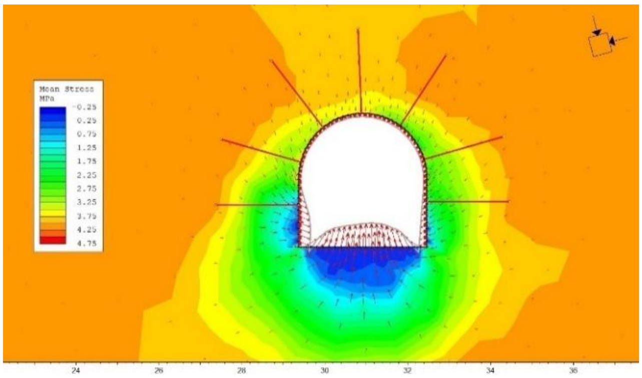

Figure 20, The deformation contour at Ch. 1+334 m

Finally, in this section, the value of the total maximum displacement obtained is 0.101413 m.

Table 5, Rock mass input parameter for chainage 1+334 m.

S.N.	Chainage (m)	Total maximum displacement (m)
1.	0+407	0.432803
2.	0+446	0.200786
3.	1+334	0.101413

Discussion

To study the deformability at different tunnel section rock mass classification was conducted from three different methods i.e. Rock Quality Index (Q), Geological Strength Index (GSI), and Rock Mass Rating (RMR) were carried out in which the Q value ranges from 0.0016 to 0.25, GSI ranges from 11 to 28, and RMR value ranges from 17 to 19. In my research using the different well-accepted equations given by Grimstad and Braton (1993), Palmström and Singh (2001), Barton (2002), Hoek and Brown (1997), Beiki et al (2010), Carvalho (2004), Hoek and Diderichs using Ei, Sreafim, and Pereira (1983), Diderichs and Kaiser (1999), Mitri et al (1994) and Gokceoglu et al (2003) were used to estimate the value of deformation modulus for the different rock types and rock class along the tunnel section. The different values obtained from the calculation were plotted to know the similarity or disparity obtained from the rock types and classes of rock. Due to the various values of the deformation modulus obtained from the various empirical formulas there exists a big challenge to pick up the value which is more appropriate to design the tunnel support and the various civil engineering structures. In the past, such kinds of studies were carried out by Panthee (2016), Kayabasi et al. (2003), and Hoek and Diderichs (2006) but the significant result was not formed.

The values of deformation modulus in some empirical relations show higher sensitivity and some of them display lesser sensitivity with the class of the rock mass. In its study, the deformation modulus value range of some equations gives a lesser deformation modulus value and some of them show higher values of the deformation modulus with the rock mass and class. In its research using the Q value the deformation modulus obtained from Barton, 2002 shows less sensitivity to the Q value than Barton (1983) and Palmström and Singh (2001). Then the deformation modulus using GSI by using the empirical relationship Hoek and Diderichs using Ei, Beiki, Carvalho, Hoek and Brown the Deformation modulus value using the Ei shows less sensitivity than the deformation modulus from Beiki et al, Carvalho, Hoek and Brown (1997) with the GSI value. Similarly, using RMR values from the different equations Gokceoglu et al. (2000), Mitri et al. (1994), Sreafim and Pereira (1983), and Diderichs and Kaiser (1999) of Gokceoglu et al. (2000) show less sensitivity than the other empirical equations with RMR value. From its research, I discovered that the deformation modulus value increases along with rising Q, GSI, and RMR values. When the value of the deformation modulus changes in a highly sensitive equation the accompanying change in the value of Q, GSI, and RMR will be significant. The equation given by Barton (2002) based on Q, Hoek, and Diederichs using Ei based on GSI and Gokceoglu et al. (2003) based on RMR are the best for the deformability estimation because all these equations show less sensitivity with the rock mass class.

The tunnel squeezing analysis uses different approaches, i.e. empirical approaches in which Singh et al. gave 90 % area of the tunnel under squeezing and Goel (1994) gave 41 % of the tunnel area of a tunnel under the severe squeezing and 59 % under the minor squeezing zone. In semi-analytical approaches Hoek and Morinas (2000) were used to find the tunnel squeezing. This method is found to be more acceptable than the other method. Using the numerical modeling approach tunnel squeezing was carried out in which Finite Element Method (FEM) was used. Using this method, total displacement was estimated and then the amount of the tunnel deformation using numerical modeling. The maximum total displacement was found in the chainage 0+407 i.e. 0.432803 m, then at chainage 0+446 and 1+334 the total displacement was found 0.200786 m and 0.10143 m respectively. In the selected tunnel section, most of them suffered from support problems.

Conclusion

The intricate challenges associated with tunnel deformation and squeezing in Gharkhola Hydroelectric Project, emphasizing the paramount importance of accurately estimating the deformation modulus (Em) of rock masses. By employing several empirical approaches based on the values of Q, GSI, and RMR reported by different studies where the equations proposed by Barton (2002), Hoek and Diederichs (using Ei), and Gokceoglu et al. (2003) exhibit superior reliability due to their diminished sensitivity to rock mass variability, thereby facilitating more precise predictions of tunnel behavior. The investigation reveals that severe squeezing phenomena, manifesting as tunnel wall closures up to 0.432803 meters, predominantly occur in sections with overburden heights approximating 134 meters, corroborating the necessity for robust support systems. Furthermore, the synthesis of empirical analyses, Hoek and Marinos' semi-analytical approach, and Phase2 numerical modeling underscores the indispensability of integrating diverse techniques to mitigate uncertainties and enhance predictive accuracy.

This study not only advances the comprehension of rock mass deformability in geologically complex terrains but also proffers pragmatic insights for optimizing tunnel design and support strategies in analogous hydroelectric ventures. Ultimately, the research advocates for the judicious selection of input parameters and the amalgamation of multiple analytical paradigms to ameliorate the fidelity of squeezing assessments and ensure the structural integrity of subterranean excavations.

References

Barla G. (2016). Applications of numerical methods in tunnelling and underground excavations: Recent trends (Keynote Paper). https://doi.org/10.1201/9781315388502-7.

Barton N. (1983). Application of Q system, index tests to estimate shear strength and deformability of rock masses. In: Proceedings of the International Symposium on Engineering Geology and Underground Construction, Lisbon, 51–70.

Barton N. (1995). The influence of joint properties in modelling jointed rock masses. Keynote Lecture, 8th ISRM Congress, Tokyo.

Barton N. (2002). Some new Q-value correlations to assist in site characterization and tunnel design. International Journal of Rock Mechanics and Mining Sciences, v. 39, 185-216. https://doi.org/10.1016/S1365-1609(02)00011-4

Barton N., Lien R., Lunde J. (1974). Engineering classification of rock masses for the design of tunnel support. Rock Mechanics 6(4):189–236. https://doi.org/10.1007/BF01239496

Beiki M., Bashari A., Majdi A. (2010). Genetic programming approach for estimating the deformation modulus of rock mass using sensitivity analysis by neural network. International Journal of Rock Mechanics and Mining Sciences, 47 (7), 1091-1103.

Bieniawski Z. T. (1973). Engineering classification of jointed rock masses. Transactions of the South African Institution of Civil Engineers, v. 15, pp. 335-342.

Carvalho J. (2004). Estimation of rock mass modulus, In Hoek E. and Diederichs M. S. (2006): Empirical estimation of rock mass modulus International Journal of Rock Mechanics and Mining Sciences, 43, 203-215.

Diederichs M. S., and Kaiser P. K. (1999). Stability of large excavations in laminated hard rock masses: The voussoir analogue revisited. International Journal of Rock Mechanics and Mining Sciences, 36 (1), 97–117. https://doi.org/10.1016/S0148-9062(98)00179-4

Goel R. K. (1994). Correlations for predicting support pressures and closures in tunnels, (Ph. D. thesis), Nagpur University, India, Unpublished, 43 p.

Goel R. K., Jethwa J. L., and Paithankar A. G. (1995). An empirical approach for predicting ground condition for tunnelling and its practical benefits. In Proceedings of the 8th International Congress on Rock Mechanics, 693–698.

Gokceoglu C., Sonmez H. and Kayabasi A. (2003). Predicting the deformation moduli of rock masses. International Journal of Rock Mechanics and Mining Sciences - INT J ROCK MECH MINING SCI. 40. 701-710. https://doi.org/10.1016/S1365-1609(03)00062-5.

Grimstad E. and Barton N. (1993). Updating the Q-system for NMT. In: Proceedings of the international symposium on sprayed concrete, Fagernes. Norway Concrete Association, Oslo, 20-58.

Hoek E. and Brown E. T. (1980a). Underground excavations in rock. Institution of Mining and Metallurgy.

Hoek E. and Brown, E. T. (1980b). Empirical strength criterion for rock masses. Journal of the Geotechnical Engineering Division, 106 (GT9), 1013–1035.

Hoek E. and Brown E. T. (1997). Practical estimates of rock mass strength. International Journal of Rock Mechanics and Mining Sciences, 34 (8), 1165–1186. https://doi.org/10.1016/S1365-1609(97)80069-X

Hoek E. and Diederichs M. S. (2006). Empirical estimation of rock mass modulus. International Journal of Rock Mechanics and Mining Sciences, 43 (2), 203–215. https://doi.org/10.1016/j.ijrmms.2005.06.005

Hoek E. and Marinos P. (2000). Predicting tunnel-squeezing problems in weak heterogeneous rock masses. Tunnels and Tunneling International, 32 (11), 45-51.

Jaiswal A., Shrivastva B. K. and Singh P. K. (2023). Numerical modelling for support design and stability analysis of a tunnel in weak rock mass. Journal of

Mining and Environment, 14 (1), 123-138. Retrieved from https://www.researchgate.net/publication/337679951, Accessed on 22 June 2023.

Kayabasi A., Gokceoglu C. and Ercanoglu M. (2003). Estimating the deformation modulus of rock mass: a comparative study. International Journal of Rock Mechanics and Mining Sciences, 40, 55-63. https://doi.org/10.1016/S1365-1609(02)00112-0

Khadka S. S., Pathak D. and Panta S. R. (2019). Numerical analysis of tunnel squeezing and support design: A case study from Nepal. Journal of Rock Mechanics and Geotechnical Engineering, 11 (6), 1266–1282. https://doi.org/10.1016/j.jrmge.2019.07.005

Mitri H. S., Edrissi R. and Henning J. (1994). Finite element modeling of rock mass deformability. Paper presented at the 1st North American Rock Mechanics Symposium, Austin, TX.

Mushahary D. R., Singh T. N. and Das R. (2020). Stability analysis of a tunnel in the Himalayan region: A finite element approach. Geotechnical and Geological Engineering, 38, 6675–6687. https://doi.org/10.1007/s10706-020-01463-7

Palmström A. and Singh R. (2001). The deformation modulus of rock masses- comparisons between in situ tests and indirect estimates. Tunneling and Underground Space Technology, 16 (3), 115–131. http://dx.doi.org/10.1016/S0886-7798(01)00038-4

Panthi K. (2006). Analysis of engineering geological uncertainties related to tunneling in Himalayan rock mass conditions. Doctoral dissertation, Norwegian University of Science and Technology. Unpublished, 189p. Retrieved from https://ntnuopen.ntnu.no, Accessed on 19 June 2023.

Panthee S. (2016). A comparative study of empirical equations for estimating deformation modulus of rock mass, Master's thesis. Tribhuvan University. Unpublished, 192p.

Rocscience Inc. (2011). RocLab 1.0 - Rock mass strength analysis using the Hoek-Brown failure criterion. [Computer software].

Selmer-Olsen R. and Broch E. (1977). General design procedure for underground openings in Norway. Paper presented at the 1st International Symposium on Storage in Excavated Rock Caverns, Stockholm. https://doi.org/10.1016/B978-1-4832-8406-4.50046-4

Serafim J. L. and Pereira J. P. (1983). Considerations of the geomechanics classification of Bieniawski. In Proceedings of the International Symposium on Engineering Geology and Underground Construction (pp. II.33–II.42). SPG.

Singh B., Jethwa J. L., Dube A. K. and Singh B. (1992). Correlation between observed support pressure and rock mass quality. Tunneling and Underground Space Technology, 7, 59-74. https://doi.org/10.1016/0886-7798(92)90114-W

Zhang L. and Einstein H. H. (2004). Using RQD to estimate the deformation modulus of rock masses. International Journal of Rock Mechanics and Mining Sciences, 41 (2), 337–341. https://doi.org/10.1016/S1365-1609(03)0

Asian Journal of Engineering Geology, 2024, Vol. 1 No. 1 and 2, 39-48

Research Article **DOI: https://doi.org/10.64862/ajeg.112.05** **Open Access**

Influence of Precipitation Variability on Pore water Pressure and Surface Layer Failures in Naturally Undulating Slopes at Nau Kilo, Narayanghat–Mugling Road, Central Nepal

Samyog Khanal[1]* and Ranjan Kumar Dahal[2]

[1]Kajaria Ramesh Tiles Ltd., Team Venture Building, 3rd floor, Sinamangal, Kathmandu, Nepal
[2]Central Department of Geology, Tribhuvan University, Kathmandu, Nepal

*(*Corresponding E-mail: Samyogkhanal2017@gmail.com)*

Received: July 15, 2024, Accepted on November 05, 2024

Abstract: This study investigates the role of pore water pressure variations in slope failures within naturally undulated hill slopes characterized by topographic hollows. A representative slope with a distinct hollow and six rainfall-induced failures recorded between 2001 and 2023 was selected for detailed analysis. Seepage and slope stability modeling were conducted in GeoStudio using the July 31, 2003, precipitation event, with simulations incorporating 24-hour maximum rainfall data corresponding to 5, 10, 25, 50, and 100-year return periods. These events were normalized using 6-minute interval rainfall data, and potential seepage face boundary conditions were applied. The results demonstrated a threshold relationship between hollow area and maximum pore water pressure, indicating that larger hollows generate higher pore water pressures under extreme rainfall. Specifically, a hollow of 100 m^2 was found to develop a maximum pore water pressure of 6.94 kPa. The findings highlight that topographic hollows act as hydrological convergence zones, increasing subsurface saturation and instability during intense rainfall events. The developed threshold relationship offers a predictive framework for assessing slope failure susceptibility in similar geomorphic settings, contributing to more effective hazard assessment and early warning systems.

Keywords: ***Hillslope Hydrology, Threshold for shallow failure, Pore water pressure.***

Introduction

Seepage and slope stability modeling is one of the crucial factors in the analysis of the rainfall-induced slope failure present in the naturally undulated slope. The landscape present in the concave depression that collects water and consists of steep slopes, which can trigger slope failure during heavy rainfall events is called a naturally undulated slope. It is important to consider the soil characteristics, moisture content, geometry of the slope, and forces developed by rainfall events for the slope stability analysis (Setyawan et al. 2021). The intense rainfall reduces the shear strength of the soil by gradually increasing pore water pressure, which leads to the instability of the slope. Thus, the seepage and slope stability model are applied in naturally undulated slopes to recognize possible processes leading to slope failure and to provide proper guidance leading to the mitigation measures (Acharya et al. 2016). Seepage modeling is the process of examining the flow of moisture in and out of the soil and dealing with the evolution of pore water pressure within the soil. Analytical methods, numerical methods, and physical methods are some widely used methods to model seepage in the slope. Finite element analysis and finite difference methods are examples of numerical methods that are complex and need more pragmatic geometrics and boundary conditions. Constructed scaled model of the slope is simulated through the flow of water in the physical models (Khan and Wang 2021). In insertion to seepage modeling, slope stability analysis plays an important role in griping the prospective for slope failure in naturally undulated slopes. The limit equilibrium analysis, finite element analysis, and numerical methods are some types of modeling techniques widely used for slope stability. The factor of safety against failure is calculated by processing the different forces acting on the slope is commonly used in the limit equilibrium analysis in geotechnical engineering (Khan and Wang 2021). The slope is classified into the small parts and analyzing it with the forces acting on each element to obtain the factor of safety against failure is done for the finite elements methods. The infiltration rate and the pore water pressure dealing out within the slope is generally influenced by rainfall intensity, duration and distribution of rainfall, so it important to model the rainfall infiltration and development of pore water pressure in the slope face (Sun et al. 2022). In general, unsaturated flow models are widely used to model the simulation of the infiltration of the rainfall into soil for the development of the pore water pressure within the slope face (Acharya et al. 2016). Shallow landslide and debris flows can be generated by the enormous and short rainfall in the soil with high permeability as explained by Campbell (1975), while common rainfall dealing with an extended period leads to deep as well as shallow landslides in the region's soil having low permeability was explained by Cardinali et al. (2006) in his study. The intensity and the duration of rainfall along with the distribution of permeability of soils play an important role in describing the type of landslide described by Dahal and Hasegawa (2008) and Pasuto and Silvano (1998). The characteristics and pattern of rainfall along with their regional area plays an important role in the landslide threshold value from one place to another with the combination of factors like lithology of the area, climate of the area, geological past histories, soil characteristics and geometry of the slope was explicate by Crosta (1998), van Asch et al. (1999) and its relation with time was explained by Crozier (1999). When there was an excellent number of databases available in connection with the rainfall events and add the landslide the threshold for landslide. occurring event were predicted by the help of a statistical model by Dahal et al. (2008).

The rainfall leads to the rainfall infiltration to develop the pore water pressure was analyzed with the help of a hydrological model as explained by Frattini et al. (2009) in his work. The development of the positive pore water pressure leads to the deep-seated failure by decreasing metric suction leading to the slope failure has been noticed by the Guzzetti et al. (2004). Topographical flow routing based on the hydrological model in saturated and unsaturated conditions was used to simulate the failure mechanism. TOPMODEL by Beven and Kirkby (1979), HILLFLOW by Bronstert (1994), SHALSTAB by Dietrich et al. (1998), and SINMAP by Pack et al. (1999) were some examples of hydrological slope stability analysis model widely used.

The naturally undulated slopes were also called topographic hollow. The convex topography with thick colluvium deposited and tends to be deposited with much infiltrated water as a result of extreme rainfall events was called naturally undulated slopes. The have capacity to evacuate slowly compared to the ridges as explained by Dunne (1978). Deposit from existing vegetation, throw away of material around the scar, gradient of slope with its type, action of wind, creeped materials, and presence of organic material plays an important role of depositions of material in the naturally undulated soles (Dietrich and Dunne 1978). The liquefaction was the one of the most effects observed in the naturally undulated slopes (Sassa 1998). Based on the mode of development and depositions they were classified as A type and B type by the Tsukamoto and Minematsu (1987). Geotechnical parameters of soils, gradient and aspect of slope, strength of vegetation root, thickness of he deposited soil plays an important role in the failure of the naturally undulated slopes (Sidle 1987). After a certain period of time of the deposition, the slope failure can occur leading to the deposition of new slope materials. That was the reason why the undulated slopes were believed to be in vogue and soon failure may occur (Dietrich 1987). The small-scale landslides were generally the most prominent features in the naturally undulated slopes (Yatabe et al. 2016). Numerous numbers of computer-based software have been created for the examination and determination of the factor of safety (FOS) of the slope. The detailed field observation data with the geometry of the was easily simulated and modeled with the help of different software. "SHIVA" was the software developed by Wagner et al. (1990) that can be used to create rock and soil hazard maps in the research field of Nepal. "CLARA" was used by Marquez (2004) used for the three-dimensional slope stability analysis. Rocscience developed da comprehensive 2D slope stability software "SLIDE" for the study of the groundwater seepage and stability of the dams was used by Kvalstad et al. (2005). FLAC (Fast Lagrangian Analysis of Continua) used in the field of geotechnical, civil and mining operations to model the groundwater seepage and its vulnerability on the slopes Pradhan (2014). "GeoStudio 2018" packages SEEP/W and SLOPE/W for seepage and slope stability analysis was used by Acharya (2016). "PLAXIS" was the software for the geotechnical study of the slopes and its stability analysis developed by Jacob et al. (2018).

Study Area

Location and Geology of the area

The study area is located in the Bagmati Province, Chitwan District, Ichchhakamana Rural Municipality near the Koyalghari area Figure 1. The study area can be accessed through road by major highway of Nepal. The study area can be approached from Kathmandu through the Tribhuvan Rajpath and the Narayanghad Muglin highway. The area of interest is also accessed by flight or through airway taking flights up to Bharatpur Airport and up to the research area. Geologically, the research area lies in the Autochthonous Unit of the Lesser Himalaya, mainly in the Labdi Khola Member of the Nourpul Formation (Paudyal and Paudel 2011, Paudyal et al. 2012, Paudyal 2017).

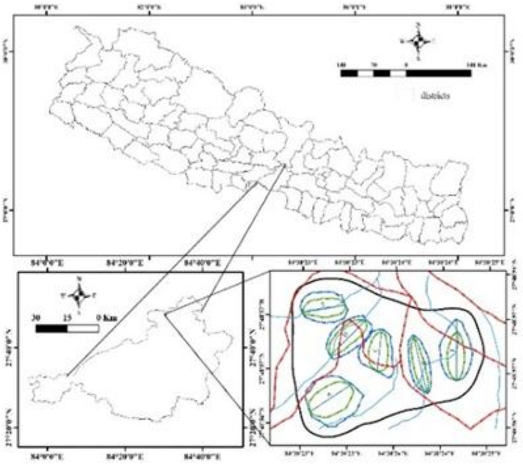

Figure 1, Location map of the study area.

The outcrop comprises interbedded phyllite and quartzite. The phyllite is reddish-brown to green on weathered surfaces and dark grey to light grey on fresh surfaces. It is thinly foliated with an average foliation spacing of approximately 8 cm and exhibits slight to moderate weathering. The quartzite beds are fine- to medium-grained, dark grey, and display slight to moderate weathering. Bedding thickness varies from thinly to thickly bedded, ranging from 12 to 22 cm. The overall lithological contact is conformable, indicating a well-developed interbedding relationship between the phyllite and quartzite units (Stöcklin 1980). The colluvium and alluvial deposited material are also observed in the study area Figure 2.

Rainfall in the study area

Rainfall data from 2001 to 2023 A.D. were analyzed to assess precipitation patterns in the study area. The highest recorded 24-hour rainfall was 446.30 mm on July 31, 2003. The study area, situated within a subtropical climate zone, experiences a pronounced monsoon season extending from June to September, during which the majority of annual precipitation occurs. The climate is characterized by unevenly distributed rainfall, as evidenced by meteorological records. The mean annual rainfall over the study period varies considerably, with the maximum total annual precipitation reaching 3,164.70 mm in 2003. That same year also recorded the highest monsoonal rainfall, amounting to 2,598.40 mm. Temperature in the region ranges from a minimum annual average of 23.6°c to a maximum of 35°c. These climatic conditions contribute significantly to slope hydrology and potential instability, especially during peak monsoonal events.

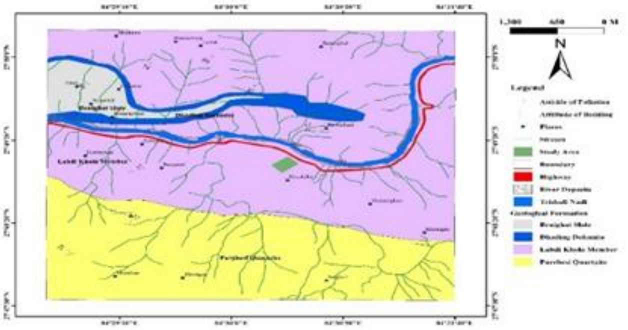

Figure 2, Geological map of the study area.

Materials and Methods

Fieldwork

The field investigation was done to gather the length/width of slope failure zones, soil thickness, and soil permeability. A dynamic cone penetration test was done to determine the thickness of the soil in the research area. For the permeability of the soil in-situ permeability test was done in the study area. Disturbed soil sampling was collected due to the impossibility of undisturbed sampling in the field due to lack of instruments and difficulty in the slope area. An overall field survey was conducted to determine the area of the failure, and soil thickness of the soil.

Laboratory Work

A series of laboratory work was performed to obtain definitive information on the soil properties. The unified Soil Classification System was used to classify the soil after the laboratory tests for porosity, moisture content, unit weight, and so on. The coarse soil particle greater than 2mm was analyzed by using the wet sieve analysis method.

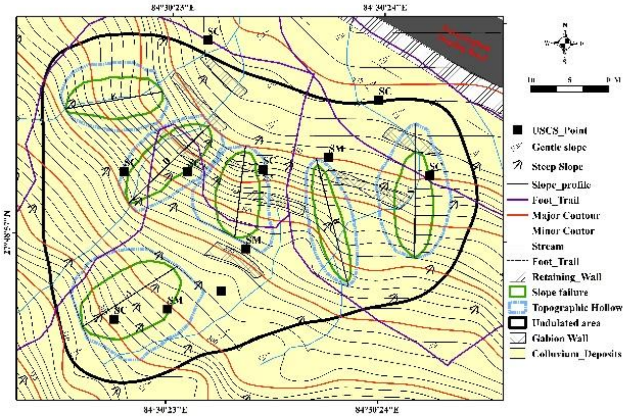

Figure 3, Engineering geological map of the study area.

Table 1, Laboratory Tests with the Standard used in the research work.

Laboratory Tests	Standards
Moisture Content Test	ASTM D2216
Specific Gravity Test	ASTM D854
Atterberg Limit Test	ASTM D4318
Particle Size Distribution	ASTM C136
Direct Shear Test	ASTM 3080
USCS	ASTM D2487

Properties of Slope Materials

The results show that the majority of soil collected from the study area is silty sand and gravel. Based on the grain size analysis of the 14 locations samples, most of them are silty sand (SM) clayey sand (SC). The most common is silty sand.

Figure 4, Process of infiltration test done at the study area.

The ASTM D2487 standard was used to classify the soils in the laboratory. The moisture content of the soil samples varies from 4.65% to 18.27%. The minimum specific gravity of the soil sample is calculated as 2.60 and the maximum specific gravity calculated as 2.79. The minimum and maximum values of infiltration rate obtained from the field work was 6.73E-05 m/sec to 3.71E-04 m/sec. The soil passes from ASTM standard sieve size 2mm was used for the direct shear test. The friction angle of the soils ranges from 26.62° to 39.97° whereas cohesion ranges from 0.08 to 0.26 Kpa.

Figure 5, Showing the process of the sieve analysis.

Slope Characteristics

Based on the flow direction map of the study area slopes were chosen for the modeling and evaluation of the stability of the area. The flow direction map shows the most unstable area on the flow line of the subsurface water in the naturally undulated slope. The most critical part of the slopes was chosen which represents the entire geometry of the study area.

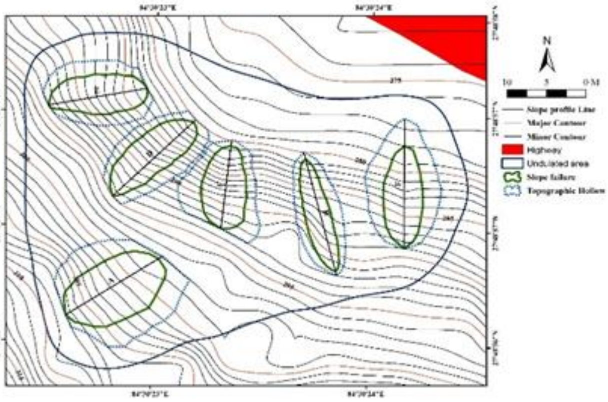

Figure 6, Naturally undulated slope with six failures.

The slope was a natural slope with average slope angles ranging from 31 to 62 degrees. The required geotechnical parameters for modeling were obtained from both field tests and laboratory tests. The slope profile was extracted with the help of Arc Map 10.8, Google Earth Pro, and DEM of the area. In the research area, six slope failures were studied. Named as A, B, C, D, E, and F as indicated in Figure 4. All slope failures were facing toward the northeast direction, recognized in the topographic map using the flow direction map Figure 5. For the seepage and slope stability analysis, all six failure slopes of the naturally undulated slope were chosen for further work.

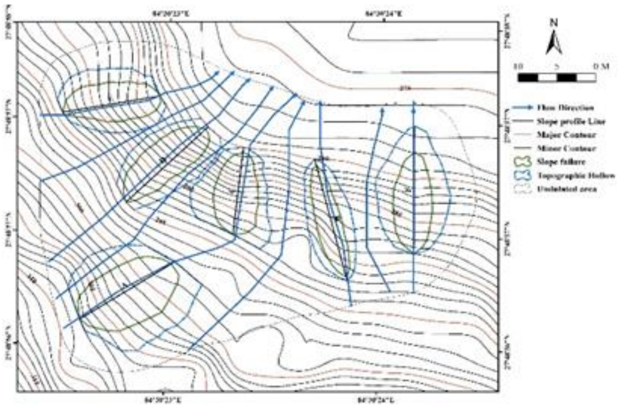

Figure 7, Flow direction map of the research area.

Results

Naturally undulated slopes were a three-dimensional feature of the geomorphological unit. Depth of soil. Length, width, curvatures of profiles i.e. concave (hollow), convex (nose), and straight and plan shapes (convergent, parallel and divergent) represents the hydro-mechanical phenomena occurring in the slope were three-dimensional in nature Dietrich (1987). Slope inclination of the naturally undulated slope was represented by the three-dimensional geometry. To model the hydrologic response of slope in relation with rainfall different models like Hydrological-Stability Model (InH-SM) by VanderKwaak (1999) and GEOFS by Rigon et al. (2006) were used in the past times.

High quality of data with solutions of large equations were required to solve these stability problems (Paniconi et al. 2003). Specification and evaluation of parameters were very difficult in these (Hilberts 2006). Therefore, the development of two-dimensional program was done for the studying the mechanism of failure of slope during the action of extreme rainfall (Carrivick 2007) by reducing the assumptions Lanni (2012). To observe the hydro-mechanical phenomenon for the rainfall induced slope failure in naturally undulated slope two-dimensional approaches were used. The following assumptions were made to apply the two-dimensional approach and get simulations:

- Slope materials fail in a single layer.
- The mode of failure is circular.
- The thickness of soil depth is equal to the maximum depth of failure.
- There are no hydrological relations between colluvium and the bed rock. So that the soil mass was assumed to be impervious.
- The failed slope material is homogeneous and isotropic.
- For both saturated and unsaturated conditions, the hydro-mechanical properties of soils are considered too same for failed mass.

- Rainwater infiltration is assumed to be in transient state conditions.
- The permeability of the soil is equal to the maximum rate of infiltration of soil.

Coupled SEEP/W-SLOPE/W models were frequently used by different researchers to estimate and observe the discharge of the hillslope seepage and capability of the failure during rainfall Dahal et al.(2009). The finite-elements based program SEEP/W in GeoStudio (2018) simulates the distribution of pore water pressure in natural slope whereas SLOPE/W allows limit equilibrium environment for slope. Due to the lack of hydrological model of pore water pressure in SLOPE/W, the modelled information from SEEP/W was directly imported into the SLOPE/W.

Seepage Modelling

For seepage and slope stability modelling, the direction of maximum subsurface flow using DEM of the study area was used to create longitudinal profile of the slopes and soil thickness based on topography of the slope. All profiles were meshed into a fine square element. Soil water characteristic curve (SWCC) function and soil permeability curve (SPC) function were utilized as the input parameters for the modelling. The GeoStudio (2018) environment consists of SWCC function Figure 6 was used for soil with similar gain size distribution pattern whereas Fredlund and Xing (1994) was used to predict the SPC function Figure 7. These two functions were integrated with saturated moisture content and soil permeability field values.

A null flux boundary was assigned for the left vertical edge and the edge below the water table to protect seepage from upper slope section and bedrock. A null flux boundary of the right vertical edge above the water table was specified as potential seepage face. The rain gauge station of Devghat station was utilized as the transient flux to the nodes on the exposed slopping surface with potential seepage face as the upper boundary conditions Figure 8. The relationship of the hillslope hydrology with naturally undulated slopes of the area along the slope profile was simulated by recording the maximum pore water pressure in an area.

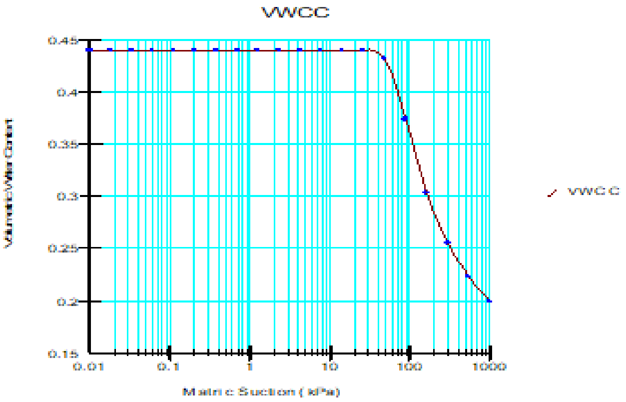

Figure 8, SWCC function used in seepage modelling.

Slope Stability Modelling

The output of the SEEP/W which was two-dimensional seepage simulated is directly linked to SLOPE/W for the stability assessment of the slope. The shear strength due to the role of suction (Φ) was assumed to be two third of Φ'. The presence of organic matter plays a crucial role in decreasing the effective cohesion, effective angle of shearing resistance, and unit weight of the soil Dahal et al. (2011). The calculation of the factor of safety was done by the sensitivity analysis which determines the interrelationship of different parameters as effective cohesion, effective angle of shearing resistance, unit weight, and Φb used in analysis. The minimum and maximum values of effective cohesion, effective angle of shearing resistance, unit weight, and Φ were depends upon the material properties and assigned in the SLOPE/W. To find the slip center and potential failure zone the entry and exit function was assigned. A limit equilibrium analysis was specified by the numbers of iteration. The sliding was divided into vertical slices to reduce the basic equation of the limit equilibrium method. The most critical value was specified by slip surfaces in the simulations.

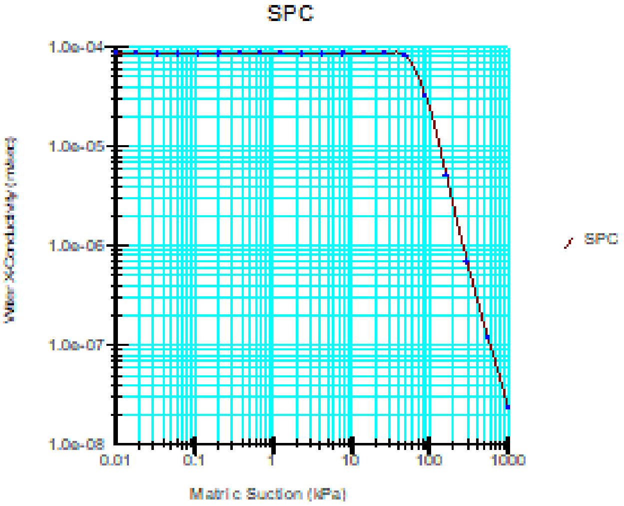

Figure 9, SPC function utilized in seepage modelling.

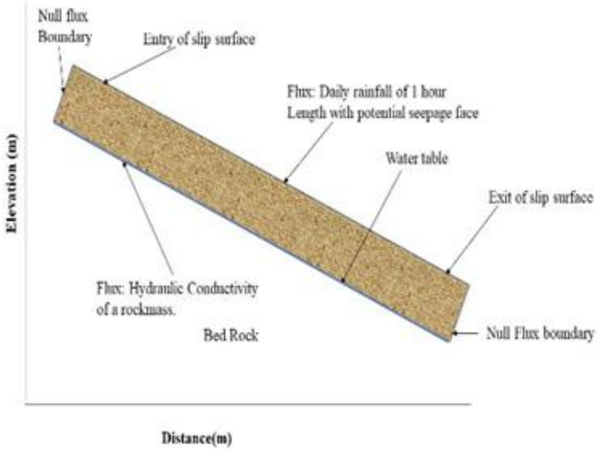

Figure 10, The finite element model used in the research work.

Seepage and Slope Stability analysis

The coupled seepage and slope stability modeling for all six failed slopes were prepared with the help of the flow direction map using the digital elevation model (DEM) of the study area. For the soil thickness data, a topographic break point in the slopes was chosen. All profile sequences were discretized into the mesh of triangle elements of 0.25m. The number of nodes was 223, 216, 164, 208, 144, and 143, whereas the number of mesh elements was 295, 297, 236, 291, 214, and 216 for slope profiles A, B, C, D, E, and F, respectively. The main input parameters used were the soil water characteristic curve (SWCC) function and the soil permeability curve (SPC) function. The slope was simulated using the maximum accumulated rainfall record in 24 hr. at Narayani at Devghat station between 2001 to 2003 A.D. The maximum 24-hour rainfall was discovered in July 31of 2003.

For the slope stability analysis, the seepage simulated in SEEP/W is directly linked to SLOPE/W. The parameters used for modeling are shown in Table 2. To remunerate some uncertainties, sensitivity analysis was performed in stability analysis. Sensitivity analysis helps to examine the interrelation sheep between various parameters used in the analysis and then calculates the factor of safety based on changes in cohesion, angle of shearing resistance, and unit weight. The Morgenstern-Price method with half-sine user-specified interslice force was used to calculate the factor of safety. To find the slip center and the potential failure surface the entry and exit points were used. A limit equilibrium analysis with 2000 iterations was used in each time step.

Table 2, Results of laboratory and field investigations.

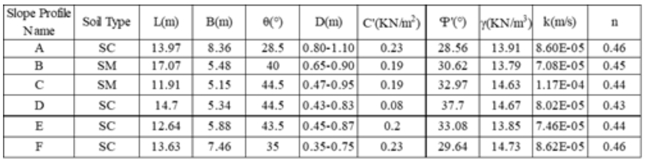

Slope Profile Name	Soil Type	L(m)	B(m)	θ(°)	D(m)	C'(KN/m²)	Φ'(°)	γ(KN/m³)	k(m/s)	n
A	SC	13.97	8.36	28.5	0.80-1.10	0.23	28.56	13.91	8.60E-05	0.46
B	SM	17.07	5.48	40	0.65-0.90	0.19	30.62	13.79	7.08E-05	0.45
C	SM	11.91	5.15	44.5	0.47-0.95	0.19	32.97	14.63	1.17E-04	0.44
D	SC	14.7	5.34	44.5	0.43-0.83	0.08	37.7	14.67	8.02E-05	0.43
E	SC	12.64	5.88	43.5	0.45-0.87	0.2	33.08	13.85	7.46E-05	0.44
F	SC	13.63	7.46	35	0.35-0.75	0.23	29.64	14.73	8.62E-05	0.46

Note: In this table, L= slope failure length; B = slope failure breadth; θ= average slope angle; D=Soil thickness; C' = effective cohesion; γ= unit weight of soil; Φ'= effective angle of shearing resistance, K= soil permeability; and n= saturated volumetric water content. C' and Φ' were determined from direct shear test. γ and n were obtained from laboratory experiments. K was measured by field experiment. These values are mean, and therefore a factor of safety via sensitivity computation was performed during slope stability analysis.

For further simulations, different return periods of the 24-hour maximum rainfall of 31 July 2003 were considered. The hydraulic function employed in the previous simulation was used using the 5 years return period of rainfall. The Gumbell technique was used to compute the return period. The variation of pore water pressure with the topographic hollow area is shown in Figure 9 for a 5-year return period. Using the area of the topographic hollow and the maximum pore water pressure data recorded, a threshold relation between the maximum pore water pressure and the topographic hollow area was established in Figure 10. The threshold equation by using the maximum pore water pressure with the topographic hollow area for the 5-year return period of rainfall expressed as

$$u = 0.0564 \times a0.9956$$

where u is the maximum pore water pressure in Kpa and a is the area of topographic hollow in sq. m.

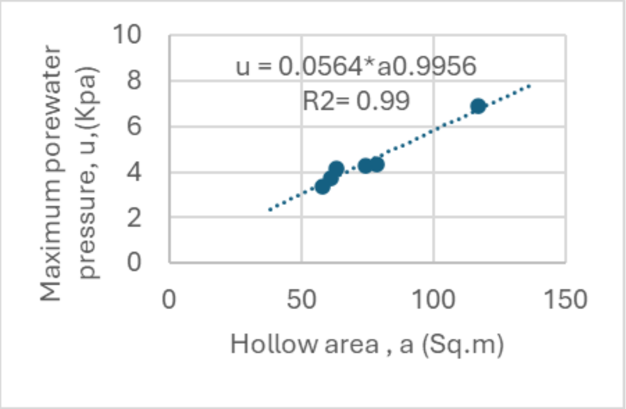

Figure 11, Variation of maximum pore water pressure with topographic hollow area for 5-year return period.

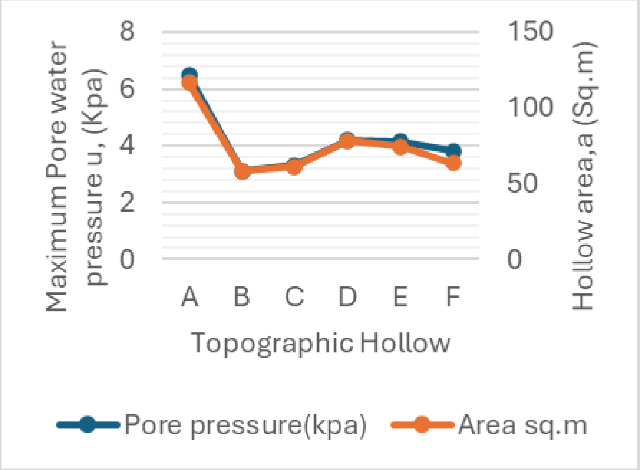

Figure 12, Pore water pressure and topographic hollow area threshold cure for slope failures for 5-year return period.

The factors of safety calculated by using the 5-year return period rainfall data were 0.494, 0.889, 0.380, 0.694, 0.457, and 0.359 respectively for the slopes A, B, C, D, E, and F. The factor of safety values shows that slopes were in very critical condition. The optimized critical slip surfaces and respective factors of safety for all slopes.

The empirical relation between the maximum discharge of hillslope seepage and the topographic hollow area presented in this study for 24 hrs maximum rainfall data and their 5, 10, 25, 50, and 100 years return period.

Table 3, Maximum Pore water pressure- topographic hollow area threshold equations for slope failure for different period of time.

Time	Threshold equation
24 hrs max	$u = 0.09*a^{0.9413}$
5-year return	$u = 0.0564*a^{0.9956}$
10-year return	$u = 0.0768*a^{0.9398}$
25-year return	$u= 0.092*a^{0.9063}$
50-year return	$u = 0.0985*a^{0.9029}$
100-year return	$u = 0.1279*a^{0.8708}$

Discussion

In past studies in the context of Nepal, the problem caused by the discharge of hillslopes and slope instability in naturally undulated slopes was not studied in detail. This study mainly focused on topographic hollows present in the naturally undulated slope and explicitly presented the hydrological and mechanical phenomenon in hollows responsible for the development of slope failure during a heavy rainfall event. The role of topographic hollows on hill slope hydrology and slope stability can be understood when they are recognized. In this research, six topographic hollows A, B, C, D, E, and F were identified in the digital elevation model based on flow direction characteristics. All the hollows in the study area were elliptical. The maximum pore water pressure developed in the topographic hollows were 7.84, 3.95, 4.43, 5.49, 5.34, and 4.5 kPa for A, B, C, D, E, and F respectively by using 24-hour maximum rainfall data. The bigger the size of hollows it produces the higher pore water pressure leads to the higher amount of subsurface follow and vice versa.

An equation of threshold relationship representing maximum pore water pressure and the hollow area was established for the 24 hrs. maximum rainfall with their return period of 5, 10, 25, 50, and 100 years as represented in Table 3 and their pore water pressure variation was shown in Figure 11. Slope failures A, B, C, D, E, and F were identified in the hollows. All these slope failures were caused by the rainfall event. So, the maximum rainfall of 2001 to 2023 years was analyzed and 24 hrs maximum rainfall was used for the simulation. Thus, the seepage and slope stability simulations were performed for the six slopes using GeoStudio 2018 to understand the hydrological and stability conditions of the topographic hollows present in the naturally undulated slopes. In the seepage modeling, transient positive and negative pore pressure was noted in all nodes in the direction of potential slip faces during rainfall events. The discharge of hillslope seepage and instability in the topographic hollows are three-dimensional but these were researched by using two-dimensional observation in this research. The finite element mesh model of slope failure profiles was used in numerical modeling using parameters like soil thickness, slope gradient, and slope length. These are the basic topographic parameters of slope mass triggering as they are used to determine the initial subsurface zone storage before rainfall. The result and finding of this two-dimensional modeling in this research should not deviate from the actual hydro-mechanical phenomenon in the topographic hollows. The empirical relation between the maximum discharge of hillslope seepage and the topographic hollow area presented in this study for 24 hrs maximum rainfall data and their 5, 10, 25, 50, and 100 years return period. These relationships are thought to help improve the understanding of the development of the discharge of hillslope seepage in hollows. Knowing about the accuracy of the empirical parameters relationship to predict the discharge of hillslope seepage, further research is needed. Hence, similar types of work should be repeated in others catchment of related geophysical settings.

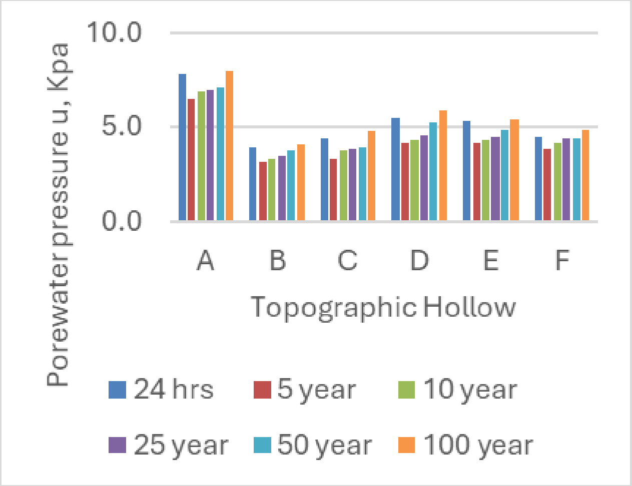

Figure 13, Histogram shows pore water pressure develop at hollow at different period of time comparison.

Conclusion

A series of fully coupled hydro-mechanical simulations were conducted to evaluate the development of positive and negative pore water pressures and their effect on the factor of safety (FoS) of a naturally undulated slope. The time-dependent analysis revealed that rapid removal of stress leads to the development of higher negative excess pore water pressure (suction), which in turn results in temporarily elevated FoS values. The water table was found to be a critical factor in pore pressure dynamics: below the water table, pore pressure is positive; above it, soils remain saturated due to capillary rise but exhibit negative pore pressures (matric suction), influencing slope stability.

Geologically, the study area is located within the Labdi Member of the Nourpul Formation, predominantly composed of phyllite. Engineering geological mapping identified features such as minor landslides, gully erosion, and shallow slope failures. Data from the

Narayani (Devghat) rainfall station confirmed that the area receives intense and prolonged monsoonal rainfall, with extreme 24-hour events, particularly in 2003, contributing to elevated failure risks.

Key findings indicate that slope failure is closely linked to the interplay between rainfall intensity and duration, pore water pressure distribution, and slope geometry. Long-duration rainfall events were observed to cause a significant increase in pore water pressure, reducing matric suction and weakening slope materials. In contrast, short-duration events had comparatively minor effects.

Finite element seepage analyses using both saturated and unsaturated flow conditions provided critical insights into temporal variations in pore water pressure, volumetric water content, and total hydraulic head. These simulations confirmed that larger naturally undulated slopes exhibit greater hillslope seepage, with the highest pore pressures developing in lower elevation hollows.

Overall, the study concludes that hydrological conditions, rainfall characteristics, and slope geometry are dominant factors controlling rainfall-induced slope failures. Effective seepage management and early warning systems are recommended to mitigate future hazards in similar geomorphic settings.

References

Acharya K. P., Bhandary N. P., Dahal R. K. and Yatabe R. (2016). Seepage and slope stability modelling of rainfall-induced slope failures in topographic hollows. Geomatics, Natural Hazards and Risk, 7(2), 721-746. https://doi.org/10.1080/19475705.2014.954150

Acharya K. P., Yatabe R., Bhandary N. P. and Dahal R. K. (2016). Deterministic slope failure hazard assessment in a model catchment and its replication in neighbourhood terrain. Geomatics, Natural Hazards and Risk, 7(1), 156-185. http://dx.doi.org/10.1080/19475705.2014.880856

Beven K. J. and Kirkby M. J. (1979). A physically based, variable contributing area model of basin hydrology/Un modèle à base physique de zone d'appel variable de l'hydrologie du bassin versant. Hydrological sciences journal, 24(1), 43-69. https://doi.org/10.1080/02626667909491834

Bronstert A. (1994). Modellierung der Abflussbildung und der Bodenwasserdynamik von Hangen Dissertation, Karlsruhe, Karlsruher Institut für Technologie (KIT).

Campbell R. H. (1975). Soil slips, debris flows, and rainstorms in the Santa Monica Mountains and vicinity, southern California (Vol. 851). US Government Printing Office. https://doi.org/10.3133/pp851

Cardinali M., Galli, M., Guzzetti, F., Ardizzone, F., Reichenbach, P. and Bartoccini, P. (2006). Rainfall induced landslides in December 2004 in south-western Umbria, central Italy: types, extent, damage and risk assessment. Natural Hazards and Earth System Sciences, 6(2), 237-260. https://doi.org/10.5194/nhess-6-237-2006.

Carrivick J. L. (2007). Hydrodynamics and geomorphic work of jökulhlaups (glacial outburst floods) from Kverkfjöll volcano, Iceland. Hydrological Processes: An International Journal, 21(6), 725-740. http://dx.doi.org/10.1002/hyp.6248

Crosta G. (1998). Regionalization of rainfall thresholds: an aid to landslide hazard evaluation. Environmental Geology, 35(2-3), 131-145. https://doi.org/10.1007/s002540050300

Crozier M. J. (1999). Prediction of rainfall-triggered landslides: A test of the antecedent water status model. Earth Surface Processes and Landforms, 24(9), 825-833. https://doi.org/10.1002/(SICI)1096-9837(199908)24:9<825::AID-ESP14>3.0.CO;2-M

Dahal R. K. and Hasegawa S. (2008). Representative rainfall thresholds for landslides in the Nepal Himalaya. Geomorphology, 100(3-4), 429-443. https://doi.org/10.1016/j.geomorph.2008.01.014

Dahal R. K., Hasegawa S., Nonomura A., Yamanaka M., Masuda T. and Nishino K. (2008). GIS-based weights-of-evidence modelling of rainfall-induced landslides in small catchments for landslide susceptibility mapping. Environmental Geology, 54, 311-324. http://dx.doi.org/10.1007/s00254-007-0818-3

Dahal R. K., Hasegawa S., Yamanaka M. and Bhandary, N. P. (2011). Rainfall-induced landslides in the residual soil of andesitic terrain, western Japan. Journal of Nepal Geological Society, 42, 137-152. https://doi.org/10.3126/jngs.v42i0.31461

Dahal R. K., Hasegawa S., Yamanaka M., Dhakal S., Bhandary N. P. and Yatabe R. (2009). Comparative analysis of contributing parameters for rainfall-triggered landslides in the Lesser Himalaya of Nepal. Environmental Geology, 58, 567-586. http://dx.doi.org/10.1007/s00254-008-1531-6

Dietrich W. (1987). Overview:" Zero-order basins" and problems of drainage density, sediment transport and hillslope morphology. International Association of Hydrological Sciences Publication, 165, 27-37.

Dietrich, W. and Dunne T. (1978). Sediment budget for a small catchment in a mountainous terrain. http://doi.org /10.1130/0091-7613(2001)029

Dietrich W. E., de Asua R. R., Coyle J., Orr, B. and Trso, M. (1998). A validation study of the shallow slope stability model, SHALSTAB, in forested lands of Northern California. Stillwater Ecosystem, Watershed and Riverine Sciences. Berkeley, CA.

Dunne T. (1978). Field studies of hillslope flow processes. In Hillslope Hydrology; Kirkby, M.J., Ed.; John Wiley & Sons: New York, NK, 227-293.

USA, 1978.

Frattini P., Crosta G. and Sosio R. (2009). Approaches for defining thresholds and return periods for rainfall-triggered shallow landslides. Hydrological Processes: An International Journal, 23(10), 1444-1460. https://doi.org/10.1002/hyp.7269

Fredlund D. G. and Xing, A. (1994). Equations for the soil-water characteristic curve. Canadian geotechnical journal, 31(4), 521-532. https://doi.org/10.1139/t94-061

Guzzetti F., Cardinali M., Reichenbach P., Cipolla F., Sebastiani C., Galli M. and Salvati, P. (2004). Landslides triggered by the 23 November 2000 rainfall event in the Imperia Province, Western Liguria, Italy. Engineering Geology, 73(3-4), 229-245. https://doi.org/10.1016/j.enggeo.2004.01.006

Hilberts A. G. J. (2006). Low-dimensional modeling of hillslope sub-surface flow processes: developing and testing the hillslope-storage Boussinesq model. Wageningen University and Research. https://doi.org/10.1029/2006WR004964

Jacob A., Thomas A. A., Nath A. G. and MP, A. (2018). Slope stability analysis using Plaxis 2D. International Research Journal of Engineering and Technology (IRJET), 5(4), 3666-3668. Retrieved from https://www.irjet.net/archives/V5/i4/IRJET-V5I4820.pdf. Accessed on 23 Dec 2023.

Khan M. I. and Wang, S. (2021). Slope stability analysis to correlate shear strength with slope angle and shear stress by considering saturated and unsaturated seismic conditions. Applied Sciences, 11(10), 4568. http://dx.doi.org/10.3390/app11104568

Kvalstad T. J., Nadim F., Kaynia A. M., Mokkelbost K. H. and Bryn P. (2005). Soil conditions and slope stability in the Ormen Lange area. Marine and Petroleum Geology, 22(1-2), 299-310. http://dx.doi.org/10.1016/j.marpetgeo.2004.10.021

Lanni C. (2012). Hydrological controls on the triggering of shallow landslides: from local to landscape scale Doctoral thesis in Environmental Engineering, XXIV cycle Faculty of Engineering, University of Trento Academic year 2011/2012. Unpublished, 155p. Retrieved from https://iris.unitn.it/retrieve/b08d6fd7-94f5-44b5-b4da-036dbef3b013/LanniC_PhD_thesis.pdf. Accessed on 20 Dec 2023.

Marquez R. M. (2004). Three-dimensional slope stability analysis using finite elements. 2000-2009-Mines Theses and Dissertations, Unpublished, 101p. Retrieved from https://repository.mines.edu/server/api/core/bitstreams/17af1632-431d-47ef-b1f7-33d4b4c07875/content. Accessed on 16 Dec 2023.

Pack R. T., Tarboton, D. G., and Goodwin, C. (1999). SINMAP 2.0-A stability index approach to terrain stability hazard mapping, user's manual. 73p. Retrieved from https://digitalcommons.usu.edu/cee_facpub/16/. Accessed on 12 Nov 2023.

Paniconi C., Troch P. A., van Loon E. E. and Hilberts A. G. (2003). Hillslope-storage Boussinesq model for subsurface flow and variable source areas along complex hillslopes: 2. Intercomparison with a three-dimensional Richards equation model. Water resources research, 39(11). http://dx.doi.org/10.1029/2002WR001728

Pasuto A. and Silvano S. (1998). Rainfall as a trigger of shallow mass movements. A case study in the Dolomites, Italy. Environmental Geology, 35(2-3), 184-189.

Paudyal K. (2017). Geological and Petrological evolution of the Lesser Himalaya between Mugling and Damauli, central Nepal

Paudyal K., Adhikari L., Maharjan N. and Paudel L. (2012). Geological setting and lithostratigraphy of Bandipur-Gondrang area of Lesser Himalaya, central Nepal. Bulletin of the Department of Geology, 15, 49-62. https://doi.org/10.3126/bdg.v15i0.7417

Paudyal K. and Paudel, L. (2011). Geological setting and lithostratigraphy of the Lesser Himalaya in the Mugling-Banspani area, central Nepal. Journal of Nepal Geological Society, 42, 51-63. https://doi.org/10.3126/jngs.v42i0.31449

Pradhan S. (2014). Stability analysis of open PIT slope using FLAC, (M.Sc. Thesis), Department of Mining Engineering, National Institute of Technology, Rourkela-769008, India. Unpublished, 69p. Retrieved from https://core.ac.uk/download/pdf/53190326.pdf. Accessed on Dec 14 2023.

Rigon R., Bertoldi G. and Over T. M. (2006). GEOtop: A distributed hydrological model with coupled water and energy budgets. Journal of Hydrometeorology, 7(3), 371-388. https://doi.org/10.1175/JHM497.1

Sassa, K. (1998). Mechanisms of Landslide Triggered Debris Flows. In: Sassa K. (eds) Environmental Forest Science. Forestry Sciences, vol 54. Springer, Dordrecht. https://doi.org/10.1007/978-94-011-5324-9_53.

Setyawan A., Alina A., Suprapto D., Gernowo R., Suseno J. E. and Hadiyanto H. (2021). Analysis slope stability based on physical properties in Cepoko Village, Indonesia. Cogent Engineering, 8(1), 1940637. https://doi.org/10.1080/23311916.2021.1940637

Sidle R. (1987). A dynamic model of slope stability in zero order basin. IAHS publ., 165, 101-110.

Stöcklin J. (1980). Geology of Nepal and its regional frame: Thirty-third William Smith Lecture. Journal of the Geological Society, 137(1), 1-34. https://doi.org/10.1144/gsjgs.137.1.0001

Sun Y., Yang K., Hu R., Wang G. and Lv J. (2022). Model Test and Numerical Simulation of Slope Instability Process Induced by Rainfall. Water, 14(24), 3997. https://doi.org/10.3390/w14243997

Tsukamoto Y. and Minematsu, H. (1987). Hydrogeomorphological characteristics of a zero-order basin. IAHS-AISH publication (165), 61-70.

van Asch T. W., Buma J. and Van Beek L. (1999). A view on some hydrological triggering systems in landslides. Geomorphology, 30(1-2), 25-32. https://doi.org/10.1016/S0169-555X(99)00042-2

VanderKwaak J. E. (1999). Numerical simulation of flow and chemical transport in integrated surface-subsurface hydrologic systems. 243p. Retrieved from https://uwspace.uwaterloo.ca/bitstreams/6c08afbe-8097-4b6d-95a4-6ba62fb74642/download. Accessed on 17 Nov 2023.

Wagner A., Leite E. and Oliver R. (1990). A landslide hazard mapping software (version 1.0), 2 volumes. ITECO CH and University of Lausanne, Switzerland, 4.

Asian Journal of Engineering Geology

Volume 1 No. 1 and 2

Table of Content

Official Journal of Nepal Society of Engineering Geology (NSEG)
Dhobighat, Lalitpur, Nepal
For Online Submission: https://ajeg.nseg.org.np